EFFECT OF COMBINED SHEAR, BENDING AND LOW AXIAL LOAD ON BEHAVIOR OF CONCRETE BEAMS REINFORCED WITH GLASS FIBER-REINFORCED POLYMER BARS

by

Senthil Kumar Velkumar

Submitted in partial fulfillment of the requirements
for the degree of Master of Applied Science

at

Dalhousie University
Halifax, Nova Scotia
April 2021

DEDICATION

I dedicate this thesis wholeheartedly to my mother and wife, who had continuously encouraged and provided their spiritual and financial support. Without their inspiration, love, and support, this master's program would not have been made possible.

TABLE OF CONTENTS

LIST OF TABLES

LIST OF FIGURES

ABSTRACT

This research's main objective was to investigate the effect of combined bending and shear behavior of the concrete beams longitudinally and laterally reinforced with glass fiber reinforced polymer (GFRP) bars subjected to low axial load less than 10% axial capacity of the beams. For the past few decades, many research projects have been conducted to investigate fiber-reinforced polymer (FRP) reinforcement's contribution in compression. However, due to insufficient experimental data, many design standards and guidelines ignore FRP bars' contribution in compression. This research shows that if the FRP beam were subjected to axial compression due to any accidental wind or seismic load, ignoring the compression might not be conservative. To characterize the flexural capacity of the beams under low axial loading, an analytical and experimental study was performed for nine full-scale reinforced concrete beam specimens of size 330 x 430 x 3100 mm with a concrete grade of 44.2 MPa, which was casted using sand coated GFRP bars with different reinforcement ratios of 1.7, 2.5 and 3.3%. The specimens were tested under four-point bending, and low axial compressive loading was applied at both ends of the beam with four electrical resistance strain gauges attached to the top and bottom of the longitudinal reinforcement to measure the compressive and tensile strain. The displacements of the beams were measured using a linear potentiometer. The tension and compression characteristics of GFRP reinforcement were obtained using appropriate test methods available in the literature. The analytical model was developed using PTC MATHCAD Prime to analyze the beams' behavior, verified by the experimental investigation. The analytical study results of the beam interaction diagram from all cases show that moment carrying capacity of the beams typically decreases by adding axial load in the range of 2.0 to 4.0% of the axial capacity of the sections. Further to the analytical model, a parametric study was performed to investigate the effect of reinforcement ratio, concrete strength, elastic modulus, cross-sectional shape, and axial load on the beams. This research's outcome through analytical findings supplemented by experimental test data recommended that the accidental axial load can no longer be ignored in FRP beams' design in some cases.

LIST OF ABBREVIATIONS USED

Abbreviations

ACI	American Concrete Institute
AFRP	Aramid Fiber Reinforced Polymer
ASTM	American Society of Testing and Materials
BFRP	Basalt Fiber Reinforced Polymer
CC	Concrete Crushing
CFRP	Carbon Fiber Reinforced Polymer
COV	Coefficient of Variation
CSA	Canadian Standards Association
FF	Flexural Failure
FRP	Fiber Reinforced Polymer
GFRP	Glass Fiber Reinforced Polymer
GPC	Geo Polymer Concrete
HSC	High Strength Concrete
LP	Linear Potentiometer
LRFD	Load and Resistance Factor Design
NSC	Normal Strength Concrete
OPC	Ordinary Portland Cement
P-M	Axial vs Bending Resistance
SD	Standard Deviation
SF	Shear Failure

Symbols

A	GFRP Reinforcement Cross-Sectional Area
A_f	Longitudinal Reinforcement Total Cross-Sectional Area
A_{fi}	Gross Area of GFRP Bars
A_{fv}	Amount of FRP Shear Reinforcement withing Spacing s
A_g	Beam Cross-sectional Area

b	Width of Beam Cross-section
b_w	Width of Web
c_b	Neutral Axis Depth of Balanced Section
c	Neutral Axis of Beam Section
C_c	Total Concrete Compressive Force of Beam Section
d	Beam Effective Depth
d_b	Diameter of GFRP Reinforcement
d_i	Depth of Each Reinforcement Layer
D_i	Inner Diameter
D_o	Outer Diameter
d_s	Diameter of Stirrup
d_v	Effective Shear Depth
e	Eccentricity of Axial Load
E_c	Modulus of Elasticity of Concrete
E_f	Modulus of Elasticity of GFRP
E_{fv}	Modulus of Elasticity of GFRP Shear Reinforcement
f'_c	Unconfined Concrete Maximum Compressive Stress at 28 days
f_{fb}	Strength of Bent Portion of FRP bar
f_{cj}	Concrete Stress Corresponding to Axial Strain of Concrete Fiber
f_{cr}	Cracking Strength of Concrete
f_{fi}	Axial Stress of GFRP
F_{fi}	Axial Force of GFRP Bars
f_{fu}	Ultimate Tensile Stress of GFRP
f_{fv}	Tensile Strength of GFRP
h	Height of Beam Cross-section
k	Curve Fitting Factor Governing for Descending Slope
k_n	Ratio of Depth of Neutral Axis to Reinforcement Depth
L_a	Anchor Length
L_g	Gauge Length
L_s	Vertical Spacing of GFRP Reinforcement
L_T	Total Length of Tension Test Specimen

M_c	Total Bending Moment due to Axial Force in Concrete Fiber
M_f	Bending Moment due to Axial Force of GFRP Bars
M_u	Total Bending Moment of Beam Section
n	Curve Fitting Factor Governing for Ascending Slope
n_f	Ratio of Modulus of Elasticity of FRP Bars to Modulus of Elasticity of Concrete
P_u	Total Compressive Force of Beam Section
r_b	Internal Radius of Bent Bar
R_r	Reinforcement Ratio
s	stirrup spacing
V_c	Nominal Shear Strength of Concrete
V_f	Shear Resistance by FRP Stirrups
ε'_c	Strain when f_c reaches f'_c
ε_{cj}	Axial Strain of Concrete Fiber
ε_{cu}	Ultimate Concrete Strain
ε_{fi}	Axial Strain of GFRP
ε_{fu}	Ultimate Axial Strain of GFRP
ε_x	Average Longitudinal Strain at Mid-span of the Section
Δ_y	Thickness of Concrete Segment
P	Reinforcement Ratio
ρ_f	FRP Reinforcement Ratio
ρ_{fb}	FRP Balanced Reinforcement Ratio
ρ_{fv}	FRP Web Reinforcement Ratio
λ	Factor for Concrete Density
φ_c	Resistance Factor for Concrete
φ_f	Resistance Factor for FRP
α_s	Inclination Angle of the Main Diagonal Compressive Strut
β	Factor for the Shear Resistance of Cracked Concrete

ACKNOWLEDGEMENTS

Foremost, I would like to express my special thanks and sincere gratitude to my research supervisor, Dr. Pedram Sadeghian, Associate Professor and Canada Research Chair in Sustainable infrastructure in the Department of Civil and Resource Engineering of Dalhousie University, who has provided me an excellent opportunity to do this research and supported me with invaluable guidance and motivation throughout this Master Thesis Research for successful completion. His immense knowledge in the field of Fiber Reinforced Composites, methodology of teaching the concepts, and his comments throughout this period made a significant impact in making this research journey a wonderful learning experience. Besides, I am extending my sincere appreciation to the supervisory committee and internal examiners, Dr. Kyle Tousignant, Dr. Navid Bahrani, and Dr. Steve Zou, for giving their valuable time for assessing and commenting on this thesis report which helped to achieve the standard quality to publish. For the laboratory specimen preparation, material procurement, and testing, it wouldn't be possible without the dedicated support of lab technicians Jordan Maerz, Jesse Keane, and Dean Grijm for mentoring and providing assistance in the lab at all times required. I wish to acknowledge my fellow students; Dillon Betts, Subharajit Roy, and Justin Thomas, who helped me a lot during concrete pouring and fabrication. I am highly grateful to Owens Corning, Toledo, OH, USA, for manufacturing and supplying the Glass Fiber Reinforced Polymer (GFRP) reinforcement material for the experimental testing of beam specimens in this research.

CHAPTER 1 INTRODUCTION

1.1 Background

Over the past few decades, concrete structures built with steel reinforcement in the humid and aggressive marine environment are more susceptible to corrosion; resulting in reduced structural strength, serviceability, maintenance cost increase, affects the performance, and curtails the life span. Based on the ASCE 2021 comprehensive assessment of America's infrastructure report card, from the 617,000 overall bridges in the United States, 42% are more than 50 years old, out of which 7.2 % are structurally deficient and considered to be in poor condition. The report showed that the annual spending on bridge rehabilitation in America increased from $14.4 to $22.7 billion (ASCE 2021). Canada's annual expenditures due to steel corrosion were $46.4 billion (Abdelkarim et al., 2019). A wide range of methods was implemented to protect the steel reinforcement from corrosion in the past by galvanization, epoxy coating, and cathodic protection. Still, these methods were costlier than using FRP reinforcement, and none of the techniques were successful in eliminating the corrosion. However, a better way and innovative approach to eliminate the problem related to corrosion are replacing the ingredients causing corrosion (steel, oxygen, and water) which can be achieved by replacing steel with fiber (Alsayed 1997). After extensive research, Fiber-reinforced polymer (FRP) bars emerged as a replacement to conventional steel reinforcement and are suitable to overcome the severe problems associated with corrosion.

There are four types of FRP bars available in the market, namely, Carbon Fiber-Reinforced Polymers (CFRP), Aramid Fiber-Reinforced Polymers (AFRP), Glass-Fiber Reinforced Polymers (GFRP), and Basalt Fiber-Reinforced Polymers (BFRP). GFRP, as shown in Fig 1-1, is the most acceptable and widely used construction industry from all the listed types of FRP bars. The interest in GFRP bars' usage in civil engineering applications increased compared with steel reinforcement because of its lighter weight, excellent corrosion resistance, higher strength to water ratio, non-electric and non-magnetic conductivity. GFRP bars have higher tensile strength than steel reinforcement; in contrast,

the modulus of elasticity of GFRP bars is much lower than its counterpart results in large deflection and crack widths. The strength of GFRP bars in compression is relatively low compared to their tensile strength; hence, FRP bars' contribution in compression should be completely ignored in ACI 440.1R-15 (ACI 2015). Based on CAN/CSA S806-12 (CSA 2012), FRP bars can be used in the compression member if FRP bars' contribution in compressive strength is neglected. The FRP bars in compression are the major issue specified by the codes that need to be addressed through further research.

Fig 1-1 Glass fiber-reinforced polymer bars

In terms of flexural behavior of GFRP bars in beams, they exhibit linear elastic behavior, which does not yield until failure (Zhu et al. 2018) due to their lower elastic modulus in the range of 40 to 60 GPa, which is a maximum of 30% in comparison to the steel reinforcement. Based on American design codes and guidelines ACI 440.1R-15 (ACI 2015), beams reinforced with FRP used as longitudinal reinforcement should be designed for two modes of failure, namely, first being the tension-controlled failure similar to steel reinforcement as specified by ACI 318-19 (ACI 2019) which will be abrupt as the FRP reinforcement fails without any yield. The later failure mode is the compression-controlled failure caused by the crushing of concrete, which provides the greater FRP reinforcement ratio (ρ_f) in the tension-controlled region above the FRP balanced reinforcement ratio (ρ_{fb}). Arivalagan (2012) experimentally tested seven square concrete beams of 150 mm x 150 mm x 900 mm cross-sectional size to assess the beam's flexural behavior and found that deflection and strains are more extensive than the beam reinforced with steel

reinforcement.

1.2 Problem Statement

In the construction industry, glass fiber-reinforced polymer bars are a widely used composite materials to replace steel reinforcement. Most of the research conducted previously on flexural performance of beam reinforced with GFRP bar was significantly accepted. As the design codes do not recommend the GFRP bars as compression reinforcement, GFRP bars are acceptable in tension. They are being used in the beam only as tension reinforcement, and these beams were not designed to accommodate any loads due to compression. In engineering practice, the steel-reinforced concrete beams are being designed only for flexure, and any low accidental axial loads due to wind or seismic loads under 10 % of the axial capacity of the beam are being ignored. As the design codes and guidelines are more stringent on GFRP bars in compression, ignoring of low axial load in the GFRP beam subjected to flexure may cause the beam to design failure.

1.3 Objectives

This research's main objectives are to investigate the flexural behavior of concrete beams reinforced with GFRP bar as longitudinal and transverse reinforcement when subjected to low axial loading, relatively less than 10% axial capacity of the beam. The flexural capacity of the GFRP beams will be taken as the load when the ultimate concrete strain reaches 3000 μmm/mm in the extreme compression zone as per ACI 440.1R-15 (ACI 2015), and this will be compared between the experimental and analytical study. The research objectives are summarized as follows:

(i) To study the experimental behavior of GFRP beams under combined shear, bending, and low axial loading.

(ii) To investigate the effects of tensile reinforcement ratio and axial load level on the failure of the beams.

(iii) To assess the flexural capacity, moment-curvature, and deflection of the beams using an analytical model.

(iv) To investigate the effect of compressive reinforcement, concrete strengths,

FRP modulus, cross-sectional shape, and axial load using a parametric study.

1.4 Research Scope

The objectives outlined in the previous section were achieved by fabricating the full-scale GFRP specimens under varying reinforcement ratios and tested under four-point bending without and with low axial load. The material properties of GFRP bars were determined by casting and testing the small-scale specimens for compression and tension testing using a universal testing machine. Further, an analytical model was created and verified using the experimental test results.

1.5 Thesis Outline

This thesis's overall layout starts with the introduction chapter, which discusses the fiber-reinforced polymer background and its significant advantages as longitudinal reinforcement in beams subjected to flexure. It will be followed by a literature review, a detailed explanation of the experimental program, the procedure followed in the analytical model, verification of the analytical model with the literature and experimental test data, and the conclusion and future research recommendations. Chapter-2 will review past researchers' literature to investigate the axial and flexural behavior of FRP bars in three cases, which include axial compression, pure bending, simultaneously subjected to axial compression and bending. Current research on the flexural capacity of GFRP bars studied in this thesis will be reviewed against previous researchers' BFRP and CFRP bars. Following the introduction and literature review, Chapter-3 will cover the experimental program that explains specimen fabrication, concrete pouring and curing, test matrix, test set-up, and instrumentation used in measuring the strain and deflection during testing.

Furthermore, after a detailed explanation of the experimental program, the testing results will be provided to discuss the various stress, strain, bending moment, and specimens' deflection behavior. Chapter-4 presents the procedure, design codes, guidelines, and equations that are used in developing the analytical model for GFRP beams to determine

the ultimate axial capacity, bending resistance, and deflection. Following the model's explanation, verification against other researchers' models, experimental verification, and parametric study are included. Finally, the thesis ends with the conclusion in Chapter-5, which contains the significant finding of this research work and several recommendations for future research derived based on this research experience.

CHAPTER 2 LITERATURE REVIEW

This chapter summarizes FRP composites' history and material properties for use as internal reinforcement in beams and columns. The primary studies focus on the conducted research on FRP reinforcement and detailed investigation of FRP reinforced columns behavior in axial compression, the FRP reinforced beam's behavior in bending, and beam-column behavior under combined axial load and bending. The various aspects of FRP reinforced concrete member's serviceability and strength behavior were studied based on the code provisions and guidelines.

Fiber-reinforced polymer (FRP) is a composite material that has been used for many decades in the aerospace, automotive, and recreational product industries due to its lightweight, stiffness, and high tensile strength. In contrast, they have been used in the construction industry only over the last two or three decades to construct new structures such as concrete pavements, highway bridges, and barriers. Furthermore, FRPs are an effective solution for upgrading or retrofitting existing structures. Corrosion of steel reinforcement is a significant issue in steel-reinforced concrete structures that experiences prolonged exposure to humid and aggressive areas causes engineering problems such as affecting the service life span of concrete by deterioration and causes extensive maintenance and rehabilitation cost, and the loss of the performance of structural components. Different techniques were developed, such as galvanized or stainless-steel bars, epoxy coating, and cathodic protection to protect reinforcement. Among all these techniques, only some of them have partially succeeded, while none of the methods have eliminated steel reinforcement's corrosion. However, to eliminate the problem related to corrosion and replace the steel reinforcement with alternative new corrosion-resistant material that needs to be sustainable, resistant against the highly aggressive environment, and cost-effective. All these factors have influenced the researchers and have become extensive research to use FRP as a possible alternative material for steel reinforcement.

Recent advances in polymer technology have led to the development of the latest generation FRP reinforcing bars for the construction industry (in the 1970s) that are

becoming cheaper in the recent years than the FRP manufactured in the beginning stage for the aerospace industry (in the 1950s) due to the larger market and they become the attractive alternatives for steel reinforcement because of their outstanding resistance to corrosion, high performance, high tensile strength, low electrical conductivity, low damping coefficient, fatigue damage resistance, electromagnetic neutrality, and low maintenance cost. Despite having a relatively high tensile strength than steel bars, it cannot be directly replaced with the equivalent amount. This is because FRP bars are anisotropic and have low elastic modulus. A tendency to rupture without yielding means they require different treatment in the design codes to steel reinforcement.

Fiber-reinforced polymers were primarily formed to make better composite material by combining the different polymer matrix components (epoxy or vinylester) reinforced with fibers such as glass, carbon, aramid, and basalt. Fiber acts basically as an elastic, brittle, and strong material that provides strength, controls the elastic modulus and is responsible for serving as the composite's load resisting component. The resins are cohesive in nature to keep the fiber together, transfer stress between the fibers, and protect the fiber's durability from environmental damages such as salt, water, and alkalis. FRP products are manufactured in various shapes and characteristics as bars, ropes, tendons, grids, sheets, and plates. For the FRP composite to achieve the reinforcing function, the fiber-volume fraction for FRP bars and rods should not be less than 55%, and for grids, the fiber-volume fraction should be more than 35% (ISIS 2007). Moreover, FRP products' mechanical properties mainly depend on various parameters within the composites such as fiber properties, volumetric ratio, adhesive resin, and manufacturing process.

There were several research conducted globally by a professional organization and research institution which had resulted in the development and publication of design codes and construction guidelines to design the structural concrete members reinforced with FRP reinforcement (ACI 440.1R-15; CAN/CSA S6-14; CAN/CSA S806-12; ISIS Design Manual No. 3 & 4). The American design code ACI 440.1R-15 for concrete reinforced with FRP bars recommended ignoring FRP bars' contribution in compression due to the lack of adequate experimental research data. The Canadian highway bridge design code

CAN/CSA S6-14 for FRP bars in compression was the same as American code ACI 440.1R-15 (ACI 2015), but the latest version of CAN/CSA S6-19 (CSA 2019) included that the design strain limit of 0.002 mm/mm can be allowed for FRP bars in compression. Another Canadian design code CSA S806 for building structures with FRP, is amending the code limitation to include the design strain limit of 0.002 mm/mm.

2.1 FRP-Reinforced Column Behavior in Axial Compression

De Luca et al. (2010) designed the study to investigate the square column reinforced with glass fiber-reinforced polymer bars and steel reinforcement to understand the behavior under axial load. Eight full-scale GFRP columns with a cross-sectional size of the 24-inch square and 10 feet length were fabricated with longitudinal reinforcement of 25 mm diameter bar and transverse reinforcement of 12.7 mm diameter bar with different spacings were used to manufacture the specimens as shown in Fig. 2-1.

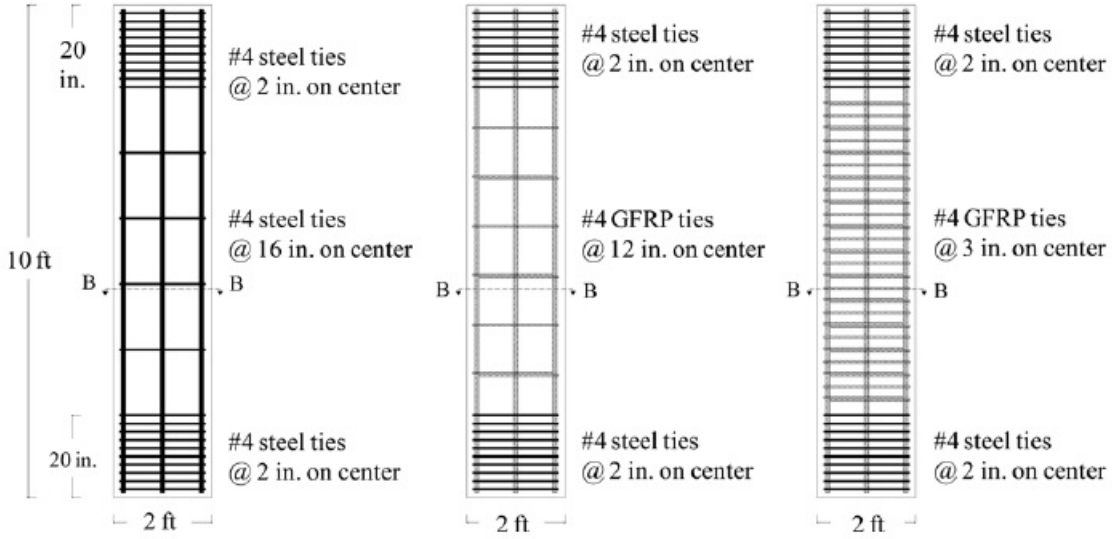

Fig 2-1 Square column cross-section and reinforcement layout (De Luca et al. 2010)

The average concrete compressive strength of specimens was 34.5 MPa, GFRP ultimate tensile strength of 608 MPa, and modulus of elasticity of 44.2 GPa. For the column with steel reinforcement, the failure pattern was brittle happened at the top half, initiated with concrete cracking. The splitting of concrete occurred, followed by concrete crushing and

buckling of longitudinal reinforcement. The specimen's failure mode with larger tie spacing initiated with the vertical cracks followed by the contribution of longitudinal reinforcement for crack widening, after which resulted in the concrete crushing and buckling of longitudinal reinforcement. Alternatively, for specimens with the smaller spacing of shear reinforcement, the outcome was axial deformation increases due to the confinement effect without concrete crushing.

A comparison of column test specimen internally reinforced with steel reinforcement and GFRP bars had shown similar behavior at the reinforcement ratio of 1.0% without any noticeable difference in the peak capacity. Furthermore, the contribution of steel reinforcement to the column capacity was 12.0 % against GFRP bars, which were less than 5.0 % under the peak load; hence, it was recommended to ignore GFRP bars' contribution in compression. However, the GFRP bars had a more significant influence on failure mode; significantly delaying longitudinal reinforcement buckling further delays the initiation of cracks, widening, and concrete crushing. The C-shaped stirrups provided as shear reinforcement partially contributed to concrete confinement after the concrete cover's initial splitting. Based on the results and research outcome in testing, De Luca et al. (2010) concluded that specimens under axial loading had refrained from proposing the changes to design criteria of ACI 440-1R to include GFRP bars as transverse and longitudinal reinforcement in compression member.

Mohamed et al. (2014) tested the circular concrete column under concentric axial load reinforced with longitudinal fiber-reinforced polymer bars, sand coated, and laterally reinforced with hoop and spiral FRP bars to evaluate the performance of FRP bars. Fourteen full-scale circular columns were fabricated in three groups such as the first group of six columns reinforced with glass fiber-reinforced polymer bars, the second group of six columns reinforced with carbon fiber-reinforced polymer (CFRP) bars, and the final group of two columns in which one with steel reinforcement and other as the plain concrete column. All test specimens were 300 mm in diameter and 1500 mm long with 6.4 mm, 9.5 mm, 12.7 mm, 15.9 mm GFRP bars, 6.4 mm, 9.5 mm, and 12.7 mm CFRP bars, and M15 steel bars. The spiral and hoop reinforcement for the test specimens were spaced at 50 mm on both ends and 80mm at mid-span location. The average compressive strength of

concrete used was 42.9 MPa, the tensile strength of GFRP and CFRP bars were in the range of 889 to 1899 MPa, and steel reinforcement with grade 60 material.

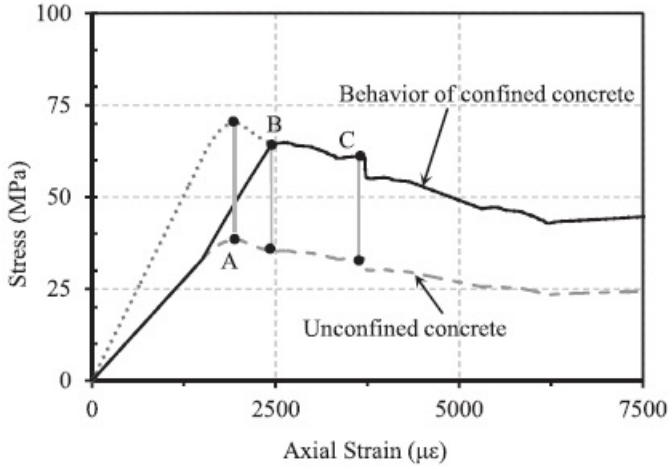

Fig 2-2 Typical stress-strain behavior of confined and unconfined FRP RC columns (Mohamed et al. 2014)

The circular concrete column's behavior was similar to linear load-strain behavior up to the peak load irrespective of the type of reinforcement as the initial stiffness was directly dependent on the strength of concrete. The columns' stress-strain behavior with confined and unconfined concrete varies, as shown in Fig. 2-2. Two different failure modes were noticed in the GFRP and CFRP test specimens; GFRP columns failure was ductile initiated with the concrete cover spalling followed by a longitudinal reinforcement buckling. The failure pattern in the CFRP column case was sudden and brittle similar to the plain concrete column. The plain circular concrete column does not exhibit any significant behavior after reaching the peak load. In contrast, in the column with CFRP, GFRP, and steel reinforcement behavior were similar until peak load; further, it took higher peak load in the ratio of 1.20, 1.24, and 1.27 compared to the plain concrete column. The compressive strain developed by GFRP and CFRP columns was 0.4 % and 0.7 %, confirming that FRP bars effectively resist compression even after the test specimen's concrete crushing. Mohamed et al. (2014) performed the analytical study considering the GFRP and CFRP bars strain up to 0.002 under the concrete strain had well predicted the test specimen's nominal capacity.

Karim et al. (2016) conducted the experimental and analytical study on circular concrete columns reinforced with sand coated glass fiber-reinforced polymer bars and helices to understand axial-load behavior deformation. Two plain circular concrete columns without reinforcement but with helical shear reinforcement and three circular columns with a diameter of 205 mm and 800 mm long with #4 longitudinal reinforcement and #3 transverse reinforcement were casted and tested under monotonic axial compression. The average concrete compressive strength was 37 MPa, and the GFRP bars used were 1600 MPa tensile strength and elastic modulus of 66 GPa. The failure mode of the tested specimens initiated with the vertical cracks at 90% of the peak load; the further increase of axial load resulted in the propagation of cracks followed by spalling of concrete cover, reducing axial carrying strength capacity. This induced stress in the helical shear reinforcement, which contained the concrete core, to increase the stiffness and sustain the axial load.

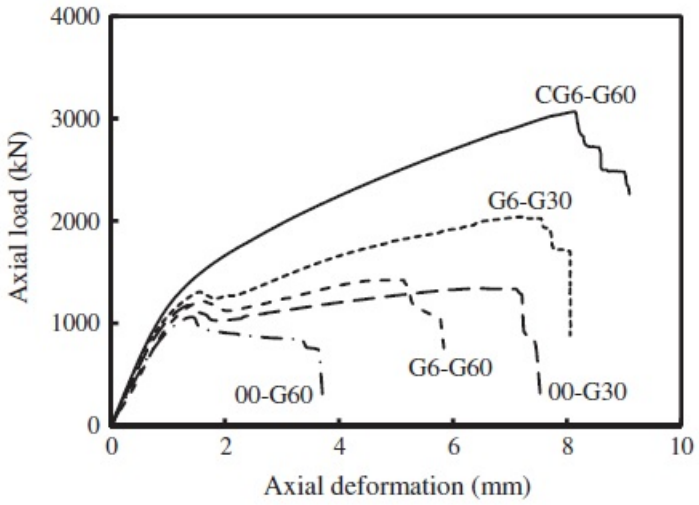

Fig 2-3 Test specimen axial-load deformation behavior (Karim et al. 2016)

Finally, further increase of axial load caused the rupture of helical reinforcement followed by the longitudinal GFRP bar fracture and concrete crushing resulting in total failure. In the case of axial-load deformation behavior, as shown in Fig. 2-3, the ascending part of the curve shows similar behavior for all test specimens until the first peak load, after which the behavior changes depending on the concrete confinement due to helical shear reinforcement. The tested specimen's first peak load demonstrated the ultimate load-

carrying capacity of unconfined concrete and was greater than the second peak load of almost all specimens; however, the second peak load demonstrated the ultimate load-carrying capacity of confined concrete. The test specimen with longitudinal reinforcement had shown better ductile behavior in comparison to the plain concrete columns. The stress-strain behavior of the GFRP bars had shown linear elastic behavior until failure based on the experimental test data. The GFRP column with longitudinal reinforcement increased the ductility, confined concrete strength, ultimate load-carrying capacity. Karim et al. (2016) proposed the equation for the curve shape factor based on the parametric study to streamline the ascending part of the stress-strain curve both for confined and unconfined concrete. The axial-load deformation curve based on the different parameters such as longitudinal reinforcement, confined and unconfined cover were plotted between the analytical model, and experimental test data had shown reasonable agreement.

Maranan et al. (2016) investigated the geopolymer circular concrete column reinforced with glass fiber-reinforced polymer bars to study the behavior when loaded with concentric axial compression. Six testing specimens with a diameter of 250 mm, length of 1000 mm, and 2000 mm with longitudinal reinforcement of #5 GFRP bars and transverse reinforcement of #3 bars. In the six full-scale circular columns, three columns were casted with circular stirrups with the spacing of 50 mm, 100 mm, and 200 mm, two columns were casted with helical stirrups with the spacing of 50 mm and 100 mm, one column without shear reinforcement. The geopolymer concrete used was produced with a mix design of 10 mm and 20 mm coarse aggregate, fine and medium sand, geopolymer binder, plasticizer, and water which gained average compressive strength of 38 MPa in 28 days. The tensile and compressive strength of the GFRP bars was arrived at based on material testing and found the bar could resist the tensile strength of 1184 MPa, the elastic modulus of 62.6 GPa, and the compressive strength of GFRP bars were 612.5 MPa. The columns were tested based on the test set-up as shown in Fig. 2-4, and the failure mode of specimens was either by crushing of concrete or by the failure of GFRP bars by crushing or buckling due to the slenderness ratio.

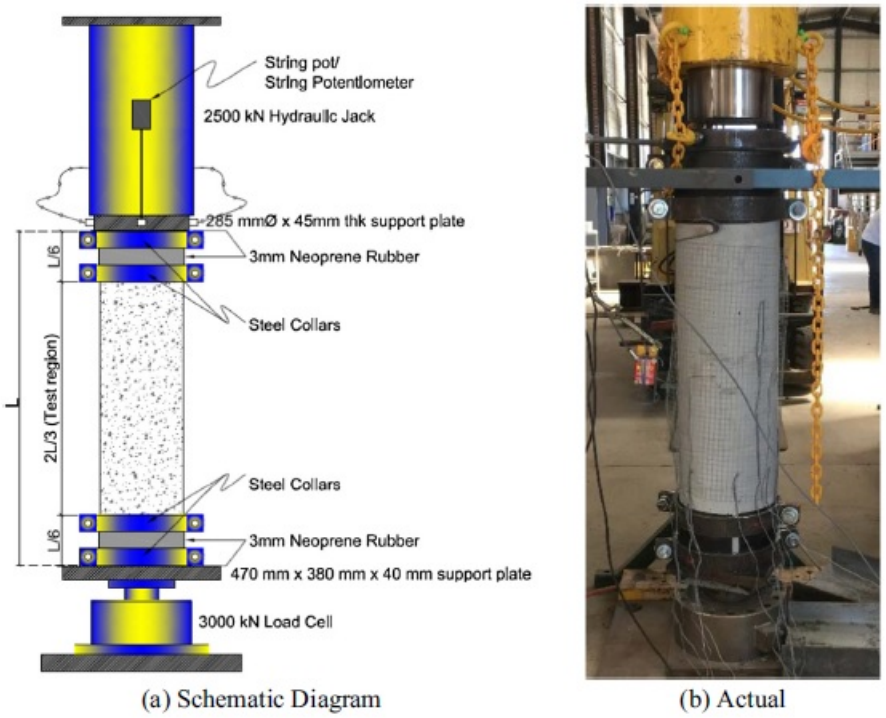

Fig 2-4 Circular column test-setup (a) Schematic (b) Actual (Maranan et al. 2016)

Initially, vertical cracks were developed in the tested specimen followed by deflection on the longitudinal reinforcement depending on the confinement of concrete by lateral reinforcement, leading to the geopolymer concrete cover split, which then reached the peak load, failed by concrete crushing and GFRP buckling at the same time. The outcome of this study showed that short columns failed due to concrete crushing; in contrast, the slender column failed due to buckling of GFRP bars which implies that short columns could yield higher ultimate compression capacities irrespective of the transverse reinforcement type and reinforcement ratio. The test specimen with the transverse reinforcement of hoop stirrups showed less ductile behavior and lower concrete cover spalling than the test specimen reinforced with spiral stirrups. The stress-strain equation proposed had demonstrated that the analytical model exhibited good agreement with the stress-strain relationship curve obtained through experimental test data. Maranan et al. (2016) proposed the equation to precisely predict the tested specimens' nominal capacity considering reduction factor as 0.9 for geopolymer concrete strength and the GFRP bar contribution in compressive strain equivalent to 2000 μmm / mm. In the slender column, the failure

happened at the lower load, and its strength compared to the short column was 66 % and 82 %. Still, the slender column's deformation compared to the short column was higher due to the lateral movement and the buckling failure.

Fillmore and Sadeghian (2018) investigated the concrete cylinders longitudinally reinforced with glass fiber-reinforced polymer bars to study the compressive behavior under axial loading. As part of this experimental investigation, a total of twenty-one concrete cylinders with the diameter of 150 mm and 300 mm long casted as plain, reinforced longitudinally with #4 GFRP, and 10M steel reinforcement were casted. The test specimens were fabricated with average compressive concrete strength of 36.2 MPa and different reinforcement arrangements of 4, 6, and 8 number bars. The steel-reinforced concrete cylinder's failure mode was concrete crushing followed by steel bars buckling after concrete spalling, as shown in Fig. 2-5 (a).

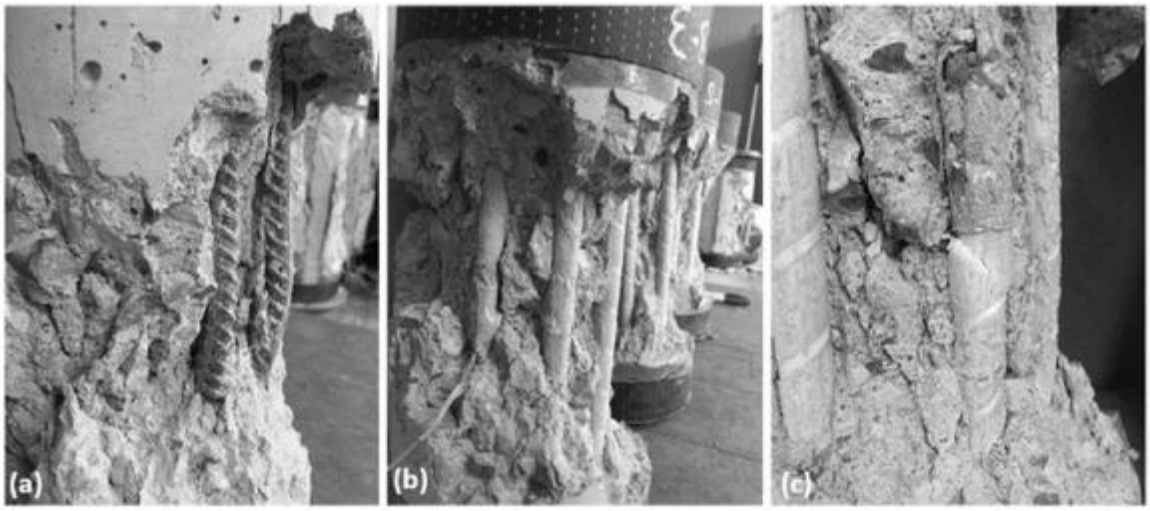

Fig 2-5 Concrete cylinder failure modes (a) Steel rebar inelastic buckling (b) GFRP rebar elastic bucking (c) GFRP rebar crushing (Fillmore and Sadeghian 2018)

Alternatively, for GFRP reinforced concrete cylinders, there was no buckling of the bar until it reaches the peak load. In contrast, once the peak load was applied, a few of the GFRP bars buckled, and some of them had crushes due to the spalling of concrete and release of confinement effect, as shown in Fig. 2.5 (b) & (c). The axial strain of test specimens was higher at peak load in steel and GFRP reinforced specimens, which showed an average strain of 0.0026 mm/mm than the strain of 0.002 mm/mm by the plain specimen.

It should also be noted that concrete cylinder with steel reinforcement, once the peak load reaches the strain in the bar reaches yield strain, after which the stress in the steel bar does not increase. On the other hand, for the concrete cylinder with GFRP bars, the stress in the bar increases with the concrete strain increase until concrete spalling happens and the GFRP bar ruptures. The specimens with GFRP bars enhanced the peak load compared to plain concrete specimens, but at the same time, GFRP bars were not effective as steel bars. This study's outcome from the test specimen was GFRP bars sustained enormous strain at peak load. Comparing the analytical model with the experimental results predicted the axial capacity of concrete cylinders through small-scale test specimens. The test specimen with GFRP bars confirm its contribution as the strength was directly proportional to the reinforcement ratio and modulus of elasticity. Furthermore, the GFRP bar had shown a similar modulus of elasticity in tension and compression; additionally, the compressive strength of GFRP bars was in the range of 66% compared to the tensile strength of GFRP bars.

2.2 FRP-Reinforced Beam Behavior in Bending

El-Nemr et al. (2013) conducted the experimental and theoretical investigation to study the flexural performance and serviceability of normal (NSC) and high strength concrete (HSC) reinforced with sand coated glass fiber-reinforced polymer. Twelve rectangular concrete beams have a cross-sectional size of 200 mm x 400 mm, and 4250 mm length was fabricated as shown in Fig. 2-6. They tested for four-point bending with varying longitudinal reinforcement diameter (#13, #15, and #25), reinforcement ratio, concrete compressive strength of 32.5 MPa for NSC and 66.2 MPa for HSC, modulus of elasticity ranging from 48.7 GPa to 69.0 GPa. The test specimens were designed as over-reinforced concrete beams with a minimum reinforcement ratio of 1.0% to attain the failure mode of concrete crushing at the compressive strain of 0.003 mm/mm, which showed the bilinear behavior until failure. The deflection behavior demonstrated that the reinforcement ratio directly correlates with the stiffness of the beam. Test specimens with lower reinforcement ratios experienced higher deflection due to the lower stiffness as against the higher reinforcement ratio test specimens shown lower deflection.

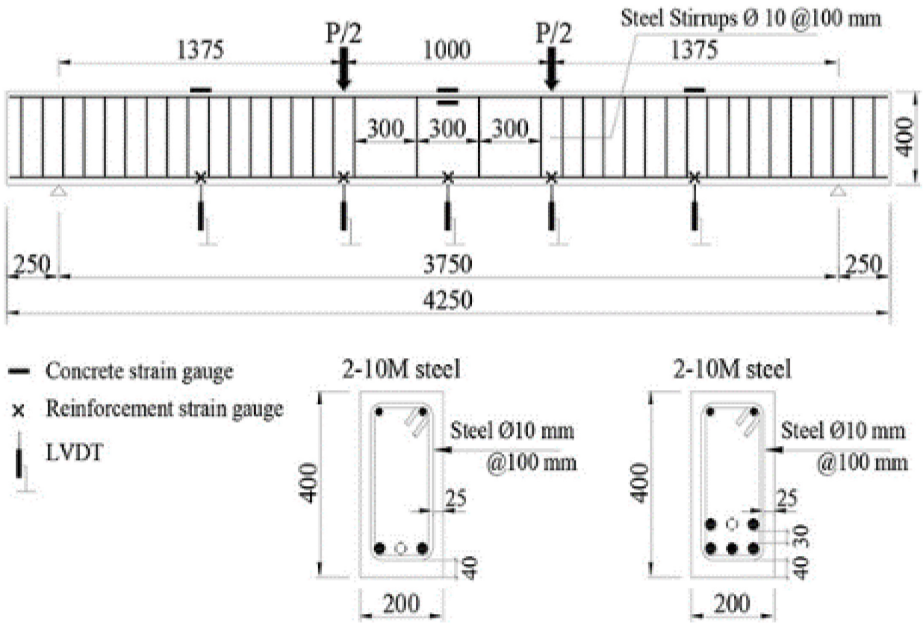

Fig 2-6 Beam reinforcement details and instrumentation set-up (El-Nemr et al. 2013)

El-Nemr et al. (2013) used the method in predicting the deflection theoretically based on CAN/CSA S806-02, considering the beam as fully cracked. The stiffness was reduced for both NSC and HSC beams after cracking, whereas NSC beams had shown lower post cracking stiffness than HSC beams while the failure behavior was similar. Furthermore, the strain levels were lower in NSC beams than HSC beams without affecting the load carry capacity. The increase in strain increase was sharper at a lower reinforcement ratio when the cracking was above 3000 μmm/mm. The ratio of experimental deflection to predicted deflection based on the equations from ACI 440.1R and ACI 440-H were 1.17 and 1.13, respectively, which were underestimated compared to experimental results. On the other hand, the ratio of experimental deflection to predicted deflection with CAN/CSA S806 and ISIS[14] was 0.76 and 0.80, respectively, which were overestimated compared to experimental results.

Elgabbas et al. (2016) demonstrated the experimental study on rectangular concrete beam reinforced with sand coated basalt fiber-reinforced polymer (BFRP) bars to characterize and investigate the flexural behavior at the serviceability and ultimate limit state. As part

of this study for experimental testing, six full-scale beams with the cross-sectional size of 200 mm x 400 mm, and 3100 mm length were built up using the different diameter of BFRP bars 10 mm, 12 mm, and 16 mm as longitudinal tension reinforcement, 10M steel bars were used as top and transverse reinforcement which were poured with concrete compressive strength of 42.4 MPa and tested under four-point bending with a clear span of 2700 mm and the loading point placed at a distance of 500 mm. To avoid shear failure, shear reinforcements were placed at a distance of 100 mm center to center at shear span locations and at mid-span location to avoid the confinement effect, no shear reinforcements were used. Furthermore, the beam specimens were designed, built, and tested based on the test set-up shown in Fig. 2-7 to fail by concrete crushing at a midspan maximum moment location.

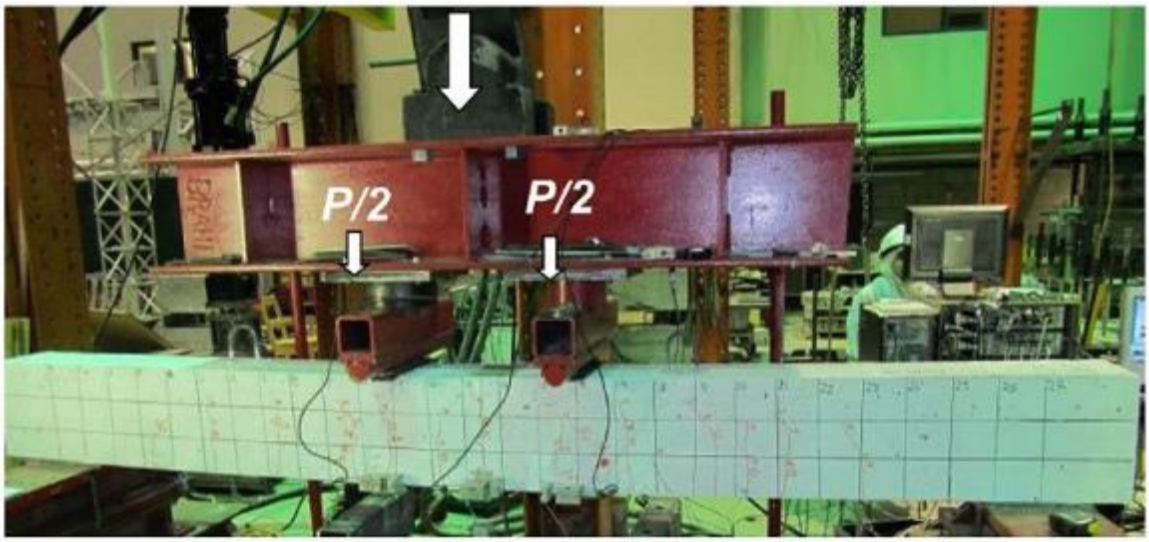

Fig 2-7 Beam during four-point bending test (Elgabbas et al. 2016)

The behavior of all test specimens tested by Elgabbas et al. (2016) was similar until the first cracking. The predicted cracking moment based on ACI and CSA was 27.0 % and 24.0 % higher than the experimental values. The moment-strain relationship illustrated that tensile and compressive strain at mid-span location was bilinear. Still, a sharp increase of strain was noted at a lower reinforcement ratio, which drastically increased the cracking location's stiffness. The BFRP bars train strain was much linear after post cracking of the beams until failure due to the beam's reduced stiffness at cracking location. The effect of reinforcement ratio had no impact on the cracking load and pre-cracking response due to

the gross moment of inertia. In contrast, after the beam's cracking, a higher reinforcement ratio played a vital role in stiffness increase and reduction of tensile strain in the BFRP bars at similar loading levels. Furthermore, the lower reinforcement ratio BFRP beams had shown a drastic increase in strain and deflection, causing the broader and deeper cracks to create the impact in stiffness and neutral axis location. The BFRP beam's deflection based on the experimental result to the predicted value using ACI was 1.08, which was unconservative. Alternatively, the ratio of deflection based on experimental to predicted using CSA was 0.92, on a conservative side.

Ovitigala et al. (2016) investigated the rectangular concrete beam reinforced Basalt fiber-reinforced polymer (BFRP) bars for serviceability and ultimate load behavior. There were eight concrete beams with a cross-sectional size of 200 mm x 300 mm, and 3350 mm long were casted with various BFRP bar diameters size of 10 mm, 13 mm, 16 mm, and 25 mm with the reinforcement ratios ranging from 1.43 to 10.70 times the balanced reinforcement ratio. The test specimens were casted with concrete compressive strength of 35.9 MPa and two steel bars' reinforcement arrangement at the compression face, BFRP bars at tension face. There was shear reinforcement of #3 steel bars spaced at 75 mm center to center from the support to loading point location and 140 mm spacing between the load points. All fabricated beams were tested under four-point bending with a clear span of 3050 mm and two-point loading spaced at 750 mm at mid-span while the support was hinged at one end and roller at the other end. All test specimens' failure pattern was similar due to the crushing of concrete in the compression face at the mid-span location. From the cracking pattern as shown in Fig. 2-8, the first vertical crack started at the middle of the beam, an additional crack developed beyond the cracking load, and propagation of crack continued until the ultimate moment capacity during which the concrete in the compression face crushed to cause the failure. In the case of moment-deflection behavior, all test specimens had shown the deflection, which was lesser before cracking; however, the deflection after the post-cracking stage can be distinguished because the increase in BFRP reinforcement ratio had a direct relationship towards the rise in stiffness and ultimate moment capacity reduced the deflection.

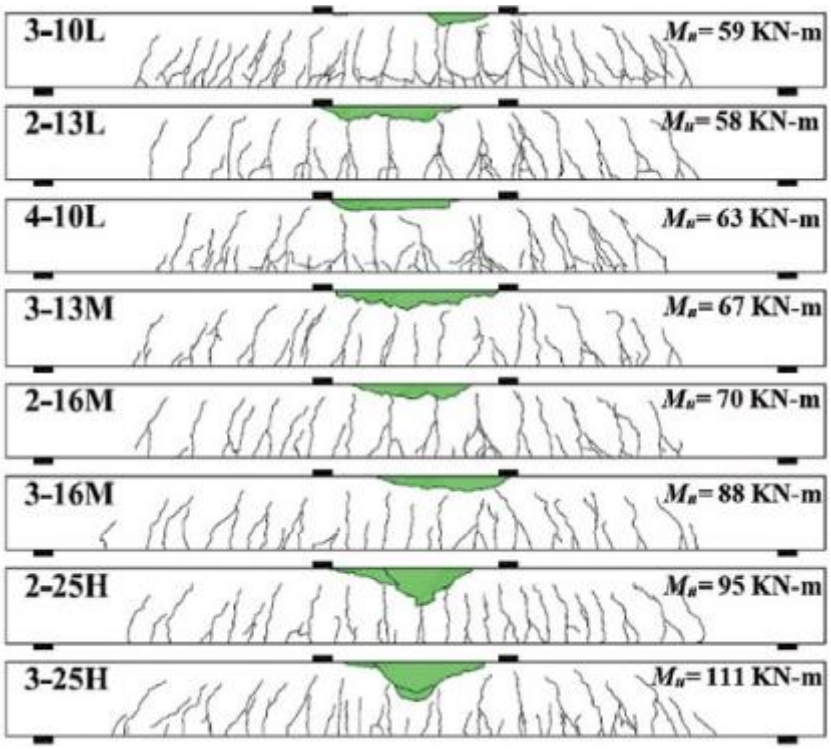

Fig 2-8 Crack pattern of all tested specimen (Ovitigala et al. 2016)

None of the test specimens had shown the noticeable strain value before the first crack of the beam, whereas the strain deformation was observed after the first crack formation; furthermore, the ultimate and post-cracking strain had shown good agreement with strain compatibility equation prediction based on ACI. In the experimental result, the ultimate moment capacity and deflection changing the rate considerably decreased with the increase of reinforcement ratio to balanced reinforcement ratio; additionally, ultimate moment capacity predicted based on ACI compared to experimental was unconservative.

El-Nemr et al. (2018) studied the flexural behavior and serviceability of rectangular concrete beams reinforced with sand-coated glass fiber-reinforced polymer bars. The experimental investigation involves testing of seventeen full-scale rectangular beams with a cross-sectional size of 200 mm x 400 mm having a length of 4250 mm were fabricated with 10M steel bars as reinforcement in the compression zone and GFRP bars of a different diameter such as 13 mm, 15 mm, 20 mm, 22 mm and 25 mm in the tension zone. The shear reinforcement was 10 mm diameter steel stirrups placed at 100 mm center to center in the

shear span location and 300 mm center to center at mid-span location to reduce the confinement effect due to stirrups at moment zone location. The specimen's failure pattern was observed, in which the first crack appeared, and the load was noted to calculate the cracking moment that seems to be directly proportional to tensile and compression strength of concrete, which implies higher the concrete compressive strength higher were the cracking moment.

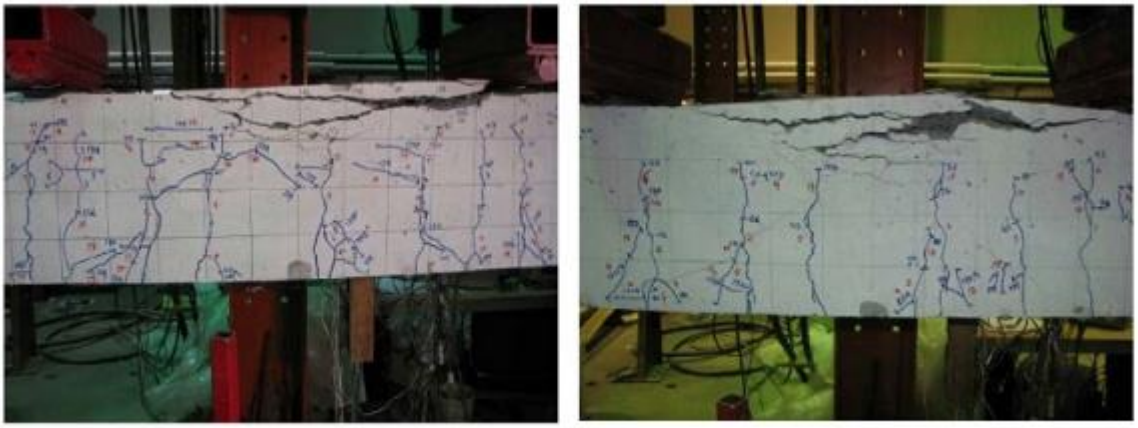

Fig 2-9 Compression failure of the tested specimen (El-Nemr et al. 2018)

All the tested beam specimens of El-Nemr et al. (2018) shown the failure due to concrete crushing as shown in Fig. 2-9, as the beams were casted as over-reinforced; furthermore, the beam had shown the bilinear behavior for the strain in GFRP and deflection until the failure of the specimens. Before the first crack, all test specimens' behavior was similar irrespective of the reinforcement ratio and confirmed the governing factor was the beam's gross cross-sectional area. Another critical governing factor that enhances the beam's flexural behavior was axial-reinforcement stiffness, which directly controls the load-carrying capacity, reduces crack width, and lowers the deflection. The smaller diameter bars had smaller strain and narrow cracks than the larger diameter bars, which increased the strain and cracking behavior. The sand coated GFRP bars' bond performance was better than the helically grooved GFRP bars was confirmed through their cracking behavior. The average ratio of experimental deflection to the predicted deflection using ACI was 1.26, which seems unconservative; alternatively, the average ratio found from the predicted

deflection using CSA was 0.90 compared with the previous, which was a conservative value.

Abdelkarim et al. (2019) evaluated the rectangular concrete beam reinforced with deformed glass fiber-reinforced polymer bars to study the flexural strength and serviceability using the normal and high strength concrete. For the experimental investigation, eight full-scale concrete beams with a cross-sectional size of 200 mm x 300 mm and a length of 3100 mm were casted with equal four of normal strength concrete (NSC) of 35 MPa and high strength concrete (HSC) of 65 MPa. The test set up was configured with a clear span of 2700 mm subjected to four-point bending supported by pinned and rolled support at either end while two-point flexural loading applied with the spacing of 500 mm at the center of the beam until the failure load. The beam was reinforced with four different size of GFRP bars such as 12 mm, 16 mm, 20 mm, and 25 mm as bottom reinforcement and two steel bars for all specimens as top reinforcement with the stirrups spaced at 100 mm center to center along the length of the beam while the mid-span was free from shear reinforcement.

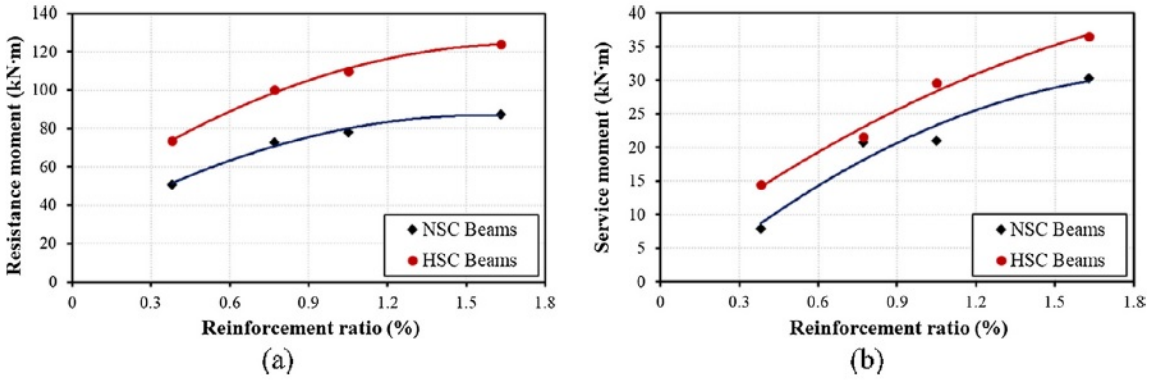

Fig 2-10 NSC and HSC beams reinforcement ratio versus (a) Resistance moment (b) Service moment (Abdelkarim et al. 2019)

The failure mode of the seven test specimens was compression failure due to the crushing of concrete, while one of the test specimens showed tension failure due to GFRP rupture. The experimental results from the testing were in the range of 0.80 to 0.99 compared to the predicted beam's nominal capacity based on the strain compatibility equation based on

CSA S-806 and ACI 440-15. The test specimen confirms the decrease of non-linear behavior, which was inversely proportional to the increasing reinforcement ratio. All the tested specimens showed the bilinear relationship in moment deflection behavior and showed non-linearity behavior just before the concrete crushing. The initial stiffness was very high for NSC and HSC beams, followed by secant stiffness, which increased with the increase of the GFRP reinforcement ratio. Simultaneously, the behavior in terms of crack width was reversed, and the increase of reinforcement ratio decreased the crack width. The resistance moment had shown an increase with higher concrete strength, as shown in Fig. 2-10, whereas in the case of service moment, the increase was dependent on the decrease in bars' spacing. Hence, the recommendation was to use the smaller diameter bars at closer spacing instead of larger diameter bars being spaced apart. The curvature ductility method used for the test specimens had shown that high strength concrete (HSC) beams were highly ductile compared to the normal strength concrete (NSC) beams.

2.3 FRP-Reinforced Beam-Column Behavior in Combined Axial and Bending

Khorramian and Sadeghian (2017) investigated short concrete columns' compressive behavior reinforced with glass fiber-reinforced polymer by performing experimental and analytical studies. The experimental study was conducted with a fabricated short concrete column of square section 150 mm x 150 mm x 500 mm long and tested under concentric and eccentric load behavior. Two different sets of specimens were fabricated for this study, including nine GFRP reinforced columns of sand coated rebars six #5 and five plain concrete columns were tested under the eccentricity to width ratio of 0, 0.1, 0.2, and 0.3. The column was tested using the universal testing machine with the steel cap plates used at the end to ensure the end boundary condition has pinned, and the loads were applied at either end of the column with the same eccentricity. The primary mode of failure of all the GFRP specimens was concrete crushing in compression, and no GFRP bars buckling or crushing in compression was detected. It was also observed that the GFRP bars were not reached the 50% of strain limit when the specimen failed, and the actual compressive strain recorded were in the range of 16% and 22% of the ultimate strain capacity of GFRP bars, as shown in Fig. 2-11.

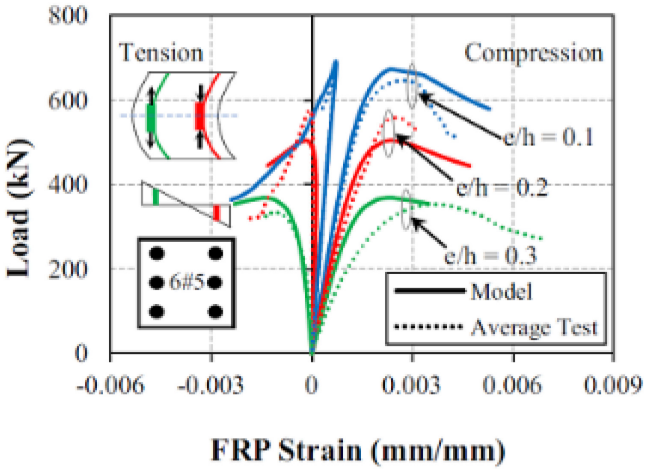

Fig 2-11 Load versus compressive and tensile strain of GFRP rebars (Khorramian and Sadeghian 2017)

The analytical model developed by Khorramian and Sadeghian (2017) in this study was based on the stress-strain relationship equation proposed by Popovics (1973), which showed that the experimental results are in good agreement with the axial load and bending moment interaction diagram. It was concluded that the design of short concrete columns should consider the contribution of GFRP bars in compression when used as a longitudinal reinforcement, and its effect can no longer be ignored.

Elchalakani et al. (2018) performed finite element and experimental analysis of rectangular columns using 16 test specimens reinforced with GFRP bars under concentric and eccentric axial load. The concrete column with a cross-sectional size of 260 mm x 160 mm and over a length of 1200 mm with 14 mm GFRP bars were casted using Geopolymer concrete (GPC) and ordinary Portland cement (OPC) concrete having a compressive strength of 26 MPa and 32.8 MPa. The different test set-up was used for the concentrically and eccentrically loaded columns, as shown in Fig. 2-12, while the later was controlled by the loading pin made with steel plates. The failure mode observed for all the specimens were concrete crushing, bending, and shear due to the reinforcement ratio and variation in the concrete material used.

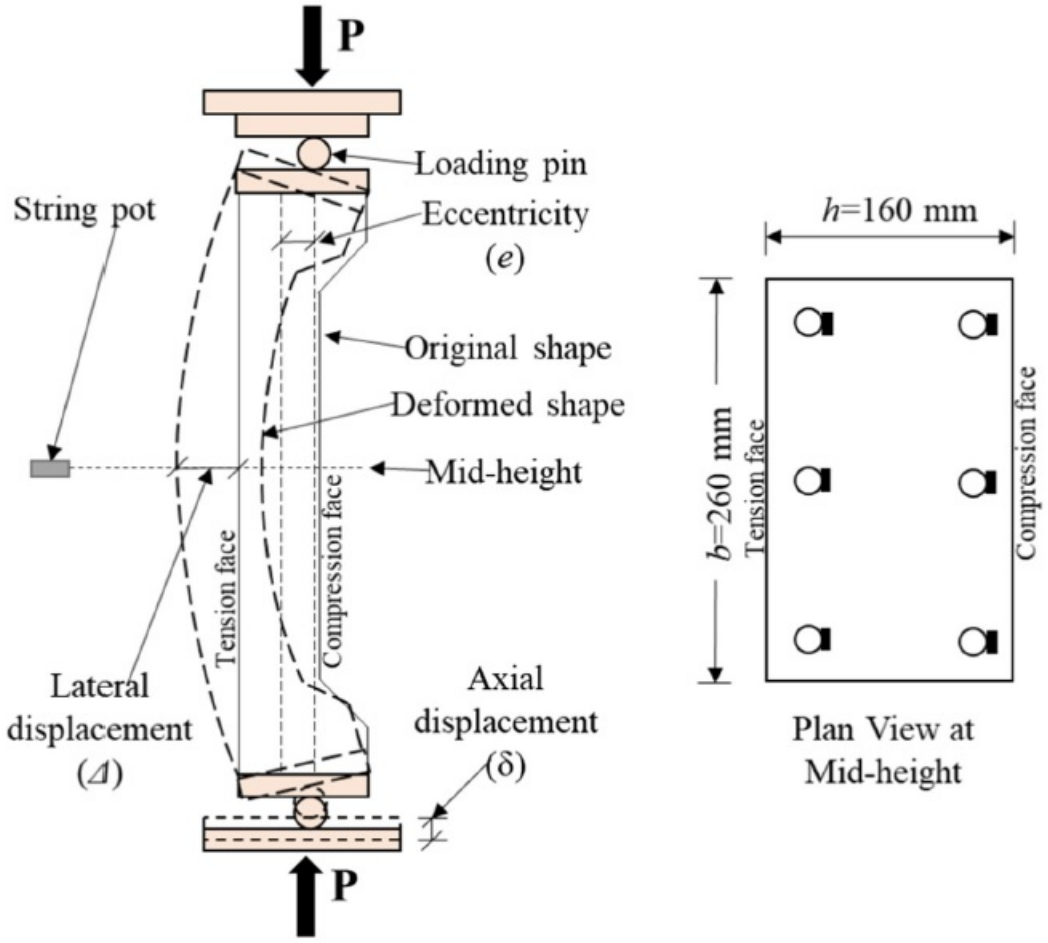

Fig 2-12 Test set-up of GFRP column with load eccentricity (Elchalakani et al. 2018)

The load-deflection curve based on the finite element model has predicted the failure closely to the experimental investigation as some of the specimens with closely spaced stirrups experienced the ductile failure. In contrast, the other experienced explosive failure at peak load. The specimen with larger stirrups spacing had shown the buckling failure against the smaller stirrups spacing in the specimen, which had clearly demonstrated the GFRP bar rupture due to longitudinal reinforcement confinement. It should also be noted that few of the tests had encountered premature failure based on which the recommendation was made on the stirrup's minimum lapping distance to be constructed with half the perimeter distance. In comparing the experimental investigation with the finite element model, there were accurate predictions in the elastic and plastic behavior of both concrete

types.

Guerin et al. (2018) conducted the analytical and experimental investigation to study the effect of reinforcement ratio on the concrete column's axial and flexural strength reinforced with glass fiber-reinforced polymer as longitudinal reinforcement. In the comprehensive experimental study, twelve columns with a square cross-sectional section of 405 mm x 405 mm reinforced with GFRP bars in the longitudinal and transverse direction and ties in transverse direction were fabricated and tested under eccentric loading conditions. As recommended in most standards and codes, the minimum reinforcement ratio of 1.0% was considered to avoid tension failure due to GFRP bar rupture (Zadeh and Nanni 2013; Hadhood et al. 2016a). The longitudinal reinforcement ratio used were of three different types in the range of 1.0%, 1.4%, and 2.5%, which were test under an axial load of four different levels of eccentricity. All fabricated columns were tested using an MTS testing machine, and before which, the specimens were protected with rigid steel cap plates at both ends to avoid any premature failure at the column ends. All the specimen's longitudinal reinforcement ratio was determined to attain the preferred mode of failure, which was concrete crushing as shown in Fig. 2-13, before the GFRP bar rupture specified in CAN/CSA 806-12 and ACI 440.1R-15.

Fig 2-13 Failure pattern of GFRP column with low eccentricity (Guerin et al. 2018)

Firstly, column failure was compression controlled, resulting in concrete crushing when the eccentricity to width ratio was below 20%; secondly, compression-tension transition

column failure in which the crack started with tension side followed by concrete crushing when the eccentricity to width ratio was between 20% and 40% and finally, tension-controlled failure due to huge tensile strain above 5000 μmm/mm in the GFRP bar when the eccentricity to width ratio was between 40% and 80%. The analytical model was developed to calculate the ultimate axial load and bending moment of the rectangular section to plot the P-M interaction diagram using the conventional method using the equilibrium of forces, compatibility of strains, and strength reduction factors. For the eccentrically loaded GFRP columns, Guerin et al. (2018) found that the tested column did not show any compression failure. The bars developed the compressive strain of 12000 μmm/mm, which resisted the compression until concrete crushing. The column subjected to large eccentric load failure was not due to GFRP bars' rupture provided the minimum longitudinal reinforcement ratio was more than 1%. The increase in the strength of the specimen tested was more pronounced in large eccentricity than the low eccentricity due to the increase of longitudinal reinforcement ratio from 1% to 2.5%. Furthermore, when considering the contribution of GFRP reinforcement compression in the force equilibrium and strain compatibility predicts the accurate analysis results compared to the experimental data, instead of ignoring the compression contribution of GFRP predicted the conservative results.

Salah-Eldin et al. (2019) investigated the theoretical and experimental behavior of concrete columns casted with high strength concrete (HSC) and reinforced with newly developed sand coated basalt fiber reinforced polymers (BFRP) to evaluate the internal reinforcement feasibility and as an alternative to conventional FRP. This research contributed to the better understanding of the BFRP reinforced column's axial-flexural strength and included the design provisions in AASHTO LRFD Bridge Design Guide Specification for GFRP Reinforced Concrete and the Canadian Highway Bridge Design Code using test data from this experimental investigation. The author has reported the experimental results by several researchers using the BFRP bars to recognize the behavior similar to glass or aramid-FRP. There were eight specimens of 400 mm x 400 mm with a square cross-section and with a length of 2000 mm was constructed and tested under different values of eccentricity. Two separate groups of columns were casted, one with six #6 longitudinal BFRP bars and #4

transverse BFRP bars at a spacing of 150 mm, the other group with six numbers 20M steel bars as longitudinal reinforcement and 10M steel bars at 300 mm spacing as transverse reinforcement. Each specimen group was tested for different eccentricity to depth ratios of 0.2, 0.3, 0.4, and 0.6h. The test data and evidence have shown that the column groups reinforced with BFRP and steel showed similar behavior at different levels of eccentricity in terms of cracking pattern, increasing tensile strain, and reduced axial strength. The failure pattern of the BFRP and steel-reinforced columns was compression controlled at lower eccentricity. However, at higher eccentricities, the BFRP column had recorded higher strain, cracking, and huge deflection was classified as a tension-controlled failure.

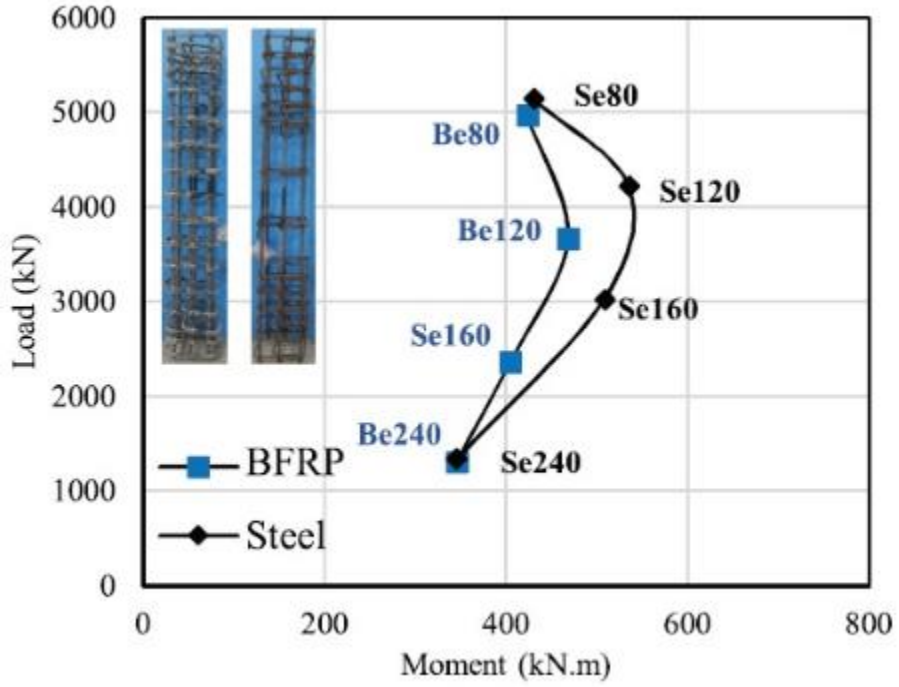

Fig 2-14 Axial-Moment interaction diagram for steel and BFRP reinforced concrete column (Salah-Eldin et al. 2019)

Comparing the test result with the analytical model has shown that the P-M interaction diagram's knee-shaped pattern was precisely similar to the interaction diagram of the steel-reinforced concrete column, as shown in Fig. 2-14. High-strength concrete with BFRP bars has developed higher axial and flexural strength; furthermore, the eccentricity increase has triggered the higher tensile strain, making them the most effective and ideal combination. Both BFRP and steel column had shown stable and ductile behavior until reaching the peak

load, whereas BFRP column enabled to experience the higher compressive strain of 4000 μmm/mm and thereby resisting the compression until the crushing of concrete.

Salah-Eldin et al. (2020) evaluated the strength and stiffness of the high-strength concrete column under eccentric loading with a change in the effect of reinforcement ratio percentage through analytical and experimental study. In this study, 12 square columns with 400 mm x 400 mm x 2000 mm length were casted using high strength concrete with a compressive strength of 70 MPa. The GFRP bars of size #5, #6, and #8 were used as longitudinal reinforcement and #3 size bar as transverse reinforcement to cast four different groups of columns. All test specimens were fabricated with the reinforcement ratios in the range of 0.5%, 1.0%, and 2.5%, with varying load eccentricity of 30%, 40%, and 70%. The outcome of the test results has shown the two types of failure mode: the compression controlled with crushing of concrete and the other being tension controlled, resulting in the development of tensile cracks with GFRP bars experiencing larger deflection and higher strain over 5000 μmm/mm. All column test specimens had failed in concrete crushing, and none of the test specimens had shown GFRP rupture at all levels of the reinforcement ratios.

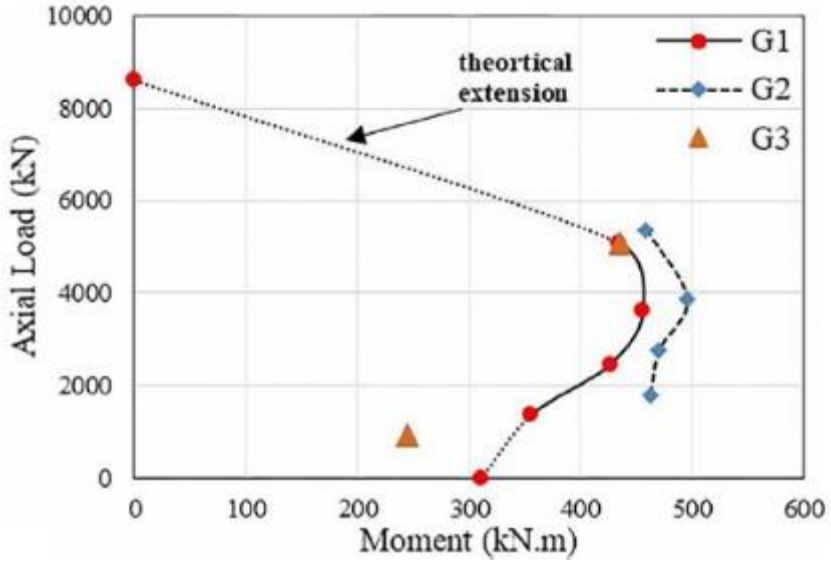

Fig 2-15 Experimental and theoretical comparison of P-M interaction diagram (Salah-Eldin et al. 2020)

The test results from the experimental testing were compared with the developed

theoretical modeling, such as the P-M interaction diagram as shown in Fig. 2-15. The moment-curvature relationship's analytical model shows a good correlation with the experimental result up to the peak load under the low eccentricities. In contrast, the analytical model had shown considerable difference under higher eccentricities. For the effect of reinforcement ratio, Salah-Eldin et al. (2020) concluded that at low eccentricity, the increase of reinforcement had a lesser impact on the strength of the column, whereas at higher eccentricity increase in the reinforcement ratio parameter had played a significant effect by developing higher strain in the GFRP bars. For the higher strength concrete column, the minimum reinforcement ratio recommended was 1.0%, and this cannot be reduced for compression members compared to normal strength concrete columns.

2.4 Behavior of FRP Reinforced Concrete in Shear

There was limited research conducted to study the shear performance of concrete beams reinforced with FRP bars. The shear reinforcement for concrete beams and columns was challenging to manufacture due to the brittle and unidirectional characteristics of FRP material. The higher tensile strength of the FRP bars was the critical feature that makes them attractive to be used as longitudinal reinforcement in concrete members and seen as a better replacement to the steel reinforcement. But the FRP bars had relatively low modulus compared to the steel reinforcement; hence this low modulus of the FRP bar had reduced the shear strength compared to the concrete member that was reinforced with an equal amount of steel reinforcement. Based on the experimental study conducted by Maranan et al. (2018) to test the eight full-scale concrete beams reinforced longitudinally and transversely with GFRP bars revealed that shear span to effective depth ratio influence the shear behavior of the beam.

Ahmed et al. (2010) investigated the fiber-reinforced concrete beam to evaluate GFRP and steel stirrups' shear strength based on experimental data and results. A total of four large-scale T-shaped RC-beam reinforced with GFRP bars were fabricated for the length of 7 m and tested. The longitudinal reinforcement in the beam were 15M and 9M steel rebars at the top and bottom; the transverse reinforcement was the GFRP stirrups of 9.5 mm diameter with the spacing of 150 mm, 200 mm, and 300 mm for three beams and steel stirrups of

9.5mm diameter for the fourth beam. The test specimens were tested with four-point bending with the point loads applied at 2000 mm from the support with the shear-span to depth ratio of 3.33. The loading rate was 5 kN/min and was applied through an actuator with a capacity of 1000 kN.

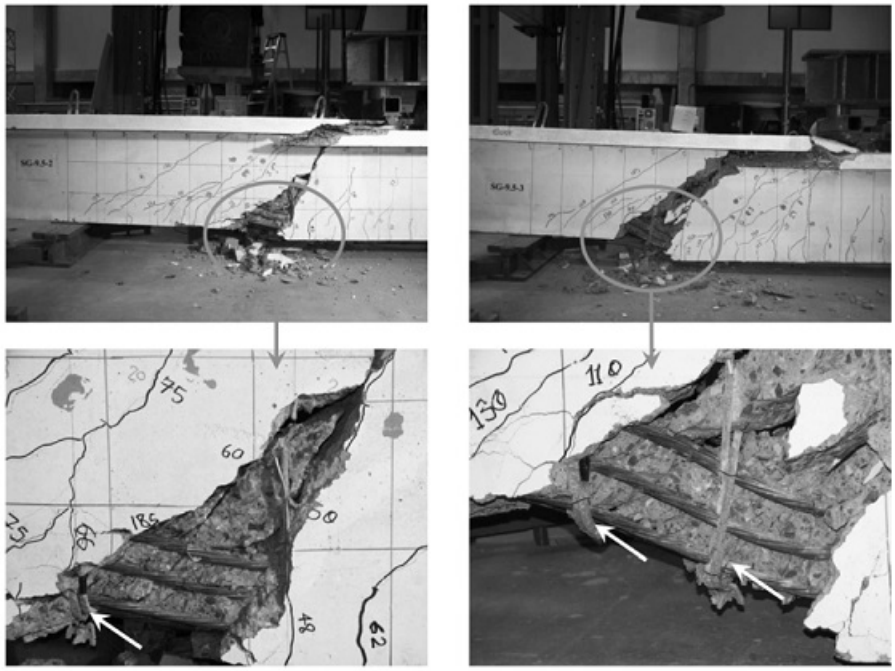

Fig 2-16 Shear failure pattern showing GFRP rupture (Ahmed et al. 2010)

All test specimens had exhibited a similar failure pattern as shown in Fig. 2-16 with the initiation of shear cracks which further widened with the applied load followed by crushing of concrete at the mid-span top flange of the beam. Finally, the tension failure occurred due to the GFRP stirrups rupture. The test specimens showed that similar to steel stirrups, GFRP stirrups enhanced the concrete contribution; however, the beam with smaller stirrups spacing had shown lower transverse strain and higher shear capacity was primarily due to the confinement that was responsible for controlling the shear cracks. All test specimens had shown the shear failure as the primary failure mode, which failed before reaching the beam's flexural capacity. In deflection, all test specimens had shown similar behavior, and there was no significant difference because of any change in the spacing of the stirrups. The flexural strain compared between the specimens was similar, which confirmed there

was no yielding of steel longitudinal reinforcement. The test specimen reinforced with steel stirrups had recorded lower strain compared to the specimen with GFRP stirrups. The strain in the GFRP stirrups was measured and compared with the other test specimens, and it was observed that the strain was maximum in the case of test specimens where larger stirrups spacing was adapted.

Said et al. (2016) evaluated the shear behavior of glass fiber reinforced concrete beams by testing the beams experimentally and comparing them through the analytical model. As part of this research, ten full-scale beams with a cross-section of 120 mm width, 300 mm depth, and 1550 mm long were fabricated with varying parameters of concrete strength, reinforcement ratio, and stirrups spacing. All test specimens were fabricated with the longitudinal reinforcement of 12 mm diameter at the top and bottom of the beam and stirrup diameter of 8 mm at a spacing of 100 mm, 150 mm, and 215 mm. The beams were tested with four-point bending supported at 1250 mm effective span with the shear span of 500 mm, and the two-point loads applied at midspan were spaced at 250 mm. The normal and high concrete compressive strength used were 25 MPa, 45 MPa, and 70 MPa for the beam divided into three groups.

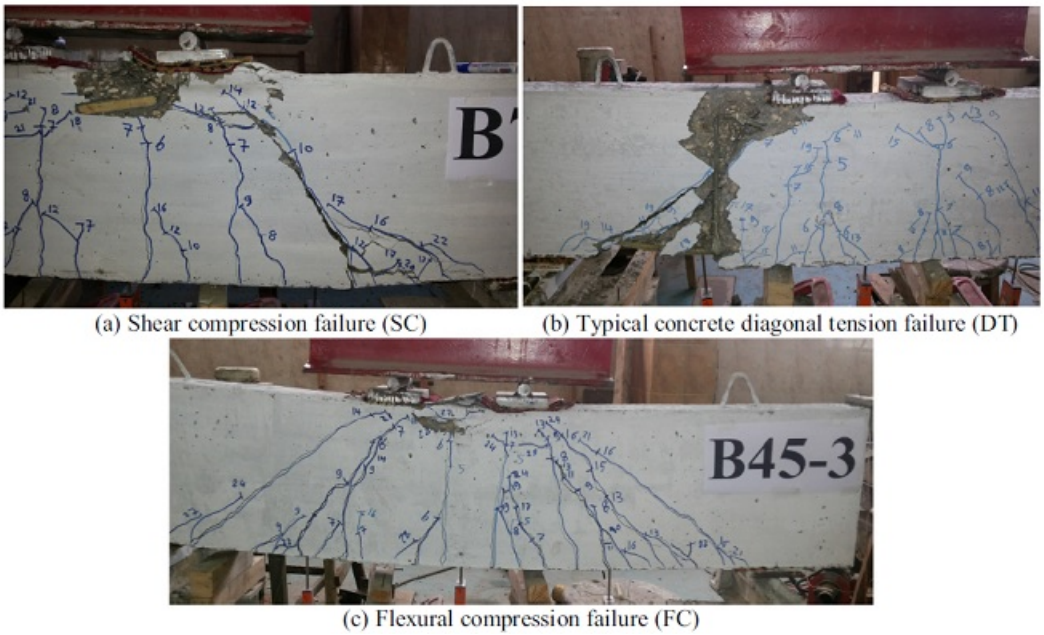

(a) Shear compression failure (SC)

(b) Typical concrete diagonal tension failure (DT)

(c) Flexural compression failure (FC)

Fig 2-17 Failure mode (Said et al. 2016)

There were three modes of failures observed in Fig. 2-17 from testing all specimens until failure, including shear compression failure, diagonal tension failure of concrete, and flexural compression failure. The test specimen with a greater number of stirrups had experienced higher shear capacity by the interlocking aggregate, creating a more significant contribution. The load-deflection behavior of all specimens was similar to the test results, which showed the stiffness and deformation due to the reinforcement ratio of the longitudinal reinforcement rather than the shear reinforcement. The concrete strength increase had a significant effect on the increased, ultimate load-carrying capacity of the beam. When the concrete strength of the specimen was increased from 25 MPa to 45 MPa as normal strength concrete, ultimate load-carrying capacity had increased by 53%, whereas when the normal concrete strength increased from 25 MPa to high strength concrete of 70 MPa, the ultimate load-carrying capacity of the beam was increased by 73%. In other words, the shear capacity of the specimen increased by 49% in the case of normal strength concrete increased from 25 MPa to 45 MPa, whereas shear capacity increased by 104% when the normal concrete strength of 25 MPa increase to high strength concrete strength of 70 MPa. The strain in the shear reinforcement was measured from the vertical stirrups at a critical location, which confirmed GFRP stirrups' effectiveness in increasing test specimens' shear capacity. The tensile strain values recorded comparatively lower strain in the GFRP bars had refrained the GFRP bar tensile rupture, which indirectly made the specimens fail in shear. The specimens with vertical stirrups had shown higher capacity after initiation of the first crack compared to the specimen without stirrups.

Maranan et al. (2017) investigated the short and slender concrete beams reinforced with glass fiber-reinforced polymer bars to evaluate the shear behavior by experimentally and verifying the results with theoretical predictions. Six full-scale short beams and one slender beam were fabricated with a cross-sectional size of 200 mm wide, 300 mm deep, and a span of 1500 mm. One of the short beams was casted without stirrups and the other with steel stirrups spaced at 150 mm; the remaining four were casted with GFRP stirrups spaced at 75 mm, 100 mm, and 150 mm. All the test specimens were designed with the longitudinal reinforcement, which was over-reinforced to induce the shear failure before the flexural failure. The slender beam was built with the same cross-section and different span of 3100 mm with an a/d ratio of 4.7, and the GFRP stirrups were placed at 100 mm spacing as

transverse reinforcement. All specimens were tested with four-point bending, and three types of failure modes, as shown in Fig. 2-18, were observed, including diagonal strut tension failure, diagonal strut compression failure, and flexural failure due to the crushing of concrete in the top compression zone.

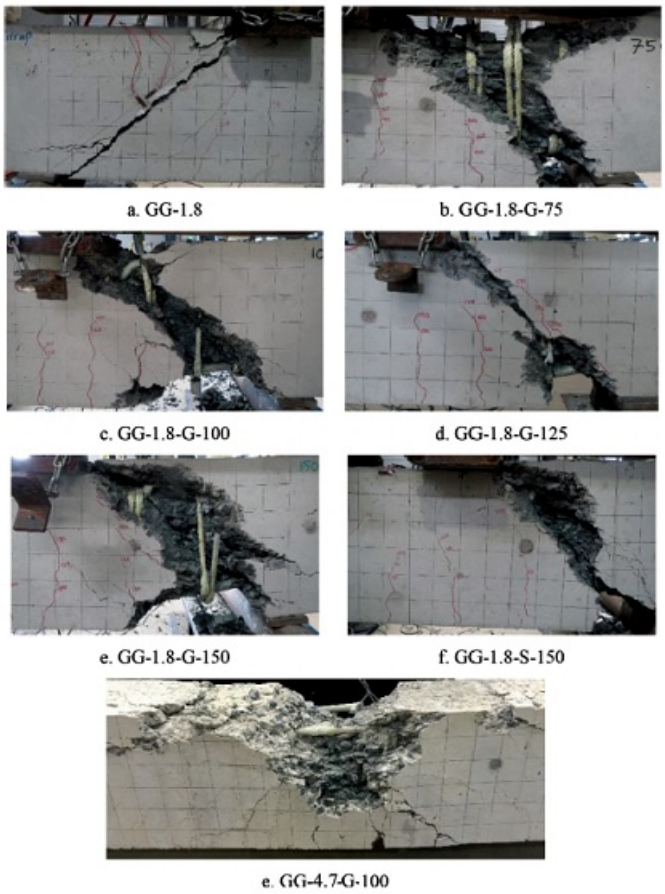

Fig 2-18 Failure mode of tested specimens (Maranan et al. 2017)

The load-deflection response of all the test specimens experienced the bilinear behavior; the initial steep behavior was due to concrete's uncracked behavior. Post-cracking behavior was the second linear behavior of the curve with reduced stiffness due to the cracked concrete. The transverse strain reading recorded from the test shows a lower strain reading at low applied load, which implies that shear stress was completely carried by concrete at lower load. The GFRP stirrups got activated and started experiencing more strain when the first diagonal shear crack initiated. From the comparison of the experimental to the analytical model, it was noted that CSA S806-12 (CSA 2012) was more conservative in

predicting the shear capacity. They were based on the ultimate tie strain assumption of 0.002, which was for steel reinforcement. For the similar load level, the FRP reinforcement strain was higher than the steel reinforcement, and the ultimate strain of 0.002 confirms that CSA S806-12 (CSA 2012) was not a suitable approach for this model.

In comparison, ACI 318-08 was the most accurate in predicting the shear capacity of the concrete beam reinforced with GFRP stirrups as they don't consider the variation in spacing and types of shear reinforcement. The GFRP stirrups usage in the concrete beam with an a/d ratio of 1.8 had increased the shear resistance of the beam by 200%, which further affected the shear cracks' reduction. The other criteria, such as close spacing of GFRP stirrups, had a more significant effect in prolonging shear crack initiation at higher load in the test specimen.

2.5 Research Gaps

From the above literature review, it was found that there were different studies conducted to understand the axial, flexure, and shear behavior of fiber-reinforced polymers rebars. The column reinforced with FRP rebars was tested for axial compression to study the contribution of longitudinal reinforcement in the compressive stresses (De Luca et al. 2010), circular column behavior of longitudinal reinforcement under confinement by transverse reinforcement of spiral stirrups (Mohamed et al. 2014; Karim et al. 2016; Maranan et al. 2016), short concrete cylinders to test the longitudinal reinforcement contribution in compression (Fillmore and Sadeghian 2018). Studies on flexural behavior of concrete beam with GFRP bars were performed to study the deflection and cracking behavior (El-Nemr et al. 2013; El-Nemr et. 2018). Further studied the cracking and deflection behavior of the concrete beam with BFRP bars (Elgabbas et al. 2016), the effect of higher reinforcement ratio increased the ultimate flexural strength by reducing the deflection (Ovitigala et al. 2016). Similarly, the reinforcement ratio increase significantly affected the service moment compared to the resisting moment (Abdelkarim et al. 2019).

Innumerable studies were performed to understand the behavior of the combined action of axial and bending in FRP beams. Eccentric loading behavior of GFRP short concrete column and verifying the experimental study through analytical model based on Popovics

stress-strain curve (Khorramian and Sadeghian 2017). Further, experimental testing of columns with different reinforcement ratio and eccentricity, which an analytical model verified based on Thorenfeldt stress-strain curve (Salah-Eldin et al. 2019; Guerin et al. 2018), verification of experimental testing of GFRP reinforced Geopolymer concrete column through finite element analysis using ABAQUS (Elchalakani et al. 2018).

However, no study was performed to investigate the behavior of concrete beam reinforced with GFRP bars subjected to flexure under low axial loading on reviewing the literature. Hence, this research was conducted to better understand GFRP reinforced concrete beam's combined behavior under bending, shear, and low axial load less than 10% of ultimate axial capacity. An analytical model was developed to compare the P-M interaction diagram, moment-curvature, and deflection behavior with the experimental test data.

CHAPTER 3 EXPERIMENTAL PROGRAM

The following section outlines the experimental program for the testing of GFRP reinforced concrete beam specimens at the Heavy Structure Laboratory of Dalhousie University. The GFRP bars and their material properties are outlined, along with a detailed explanation of rebar arrangement, assembly, fabrication, and testing of the specimens. Each specimen's critical failure mode was demonstrated depending on its reinforcement, material, arrangement, and loading condition. Furthermore, the test results for load-deformation behavior, load-strain behavior, moment-curvature behavior were analyzed, aiming to provide new guidelines for the flexural design capacity of beam reinforced with GFRP bars.

3.1 Test Matrix

To adequately fulfill the objective mentioned in the earlier section 1.3, a total of nine rectangular beams, as shown in Table 3-1, were designed to be tested under different loading conditions. The specimens were named based on the concept of labeling like “B-RX-PY” with the specific notation to identify the beam type. In the beam label, “R” stands for reinforcement ratio, and the number assigned next to it represents the percentage for this specific beam. Furthermore, “P” stands for the axial load applied, and the number assigned next to “P” representing the percentage of the load. For example, the beam with mark number “B-R1.7-P4” represents the beam with a 1.7% reinforcement ratio and 4% axial load to the beam's capacity. The reinforcement ratio for all beams was calculated using the Eq (3-1), only considering the tension reinforcement in the bottom two layers divided by width (b) and effective depth (d). All beam specimens were of the same size with 330 mm width, 430 mm height, and 3050 mm length, as shown in Fig 3-1. The dimensions were chosen based on the condition and capacity of the testing facility at the university laboratory. All specimens selected were designed to investigate the beam's flexural and shear capacity due to 4-point bending under zero (pure bending), 2.0%, and 4% axial capacity of the beams. These specimens were divided into three groups having different reinforcement ratios and rebar arrangement at the bottom. The sand coated #8 GFRP bars were used for longitudinal reinforcement, and GFRP bars #3 were used for

transverse reinforcement.

Table 3-1 Test matrix

Specimen Number	Beam ID	Beam Type	Axial Load (%)	Axial Load (kN)	Longitudinal Bars		GFRP Ratio %
					Size	No. of Bars	
1	B-R1.7-P0	1	0	0	#8	6	1.7
2	B-R1.7-P2	1	2	125	#8	6	1.7
3	B-R1.7-P4	1	4	250	#8	6	1.7
4	B-R2.5-P0	2	0	0	#8	8	2.5
5	B-R2.5-P2	2	2	125	#8	8	2.5
6	B-R2.5-P4	2	4	250	#8	8	2.5
7	B-R3.3-P0	3	0	0	#8	10	3.3
8	B-R3.3-P2	3	2	125	#8	10	3.3
9	B-R3.3-P4	3	4	250	#8	10	3.3

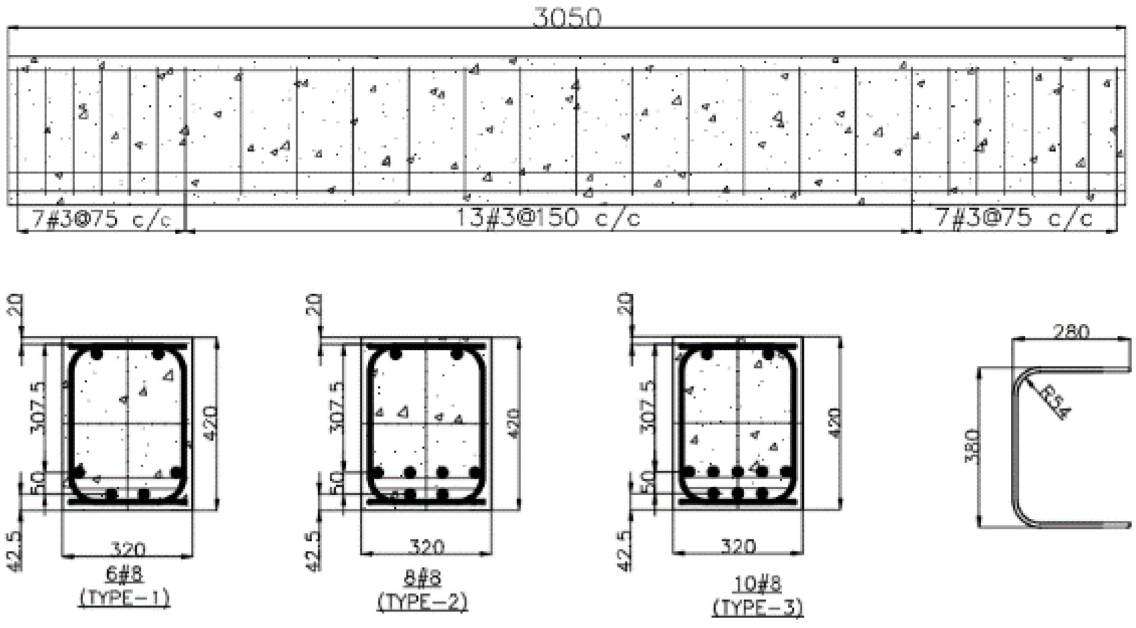

Fig 3-1 Beam dimensions and reinforcement details (dimension in mm)

3.2 Material Properties

The materials used in the fabrication of GFRP beam specimens, and their properties were outlined in this section. For GFRP bars, the material data sheet from the manufacturer and the tensile test performed to confirm the bar properties were provided. The beams were casted with ready mix normal weight concrete made of 12.5 mm aggregate size with a water-to-cement ratio of 0.32, superplasticizers, retarder, and an average 28-days compressive strength of 44.1 MPa. A minimum of nine cylinders with a diameter of 100 mm and length of 200 mm that were cured under similar conditions of the specimen was tested on the day of testing to arrive at the average concrete compressive strength determined following ASTM C39M-12 (ASTM 2012). The GFRP bars used in the specimen were manufactured by the manufacturer Owens Corning (Toledo, OH, USA) from glass fibers content of 80% impregnated in vinyl-ester resin using pultrusion process with the mechanical properties as shown in Table 3-2.

Table 3-2 Mechanical properties of GFRP bars as per the manufacturer Owens Corning (Toledo, OH, USA)

Bar Size	**Nominal Diameter (mm)**	**Nominal Area (mm^2)**	**Ultimate Tensile Strength (MPa)**	**Tensile Modulus (GPa)**	**Ultimate Strain (%)**
#3	10	71.26	827	46	1.79%
#8	25	506.7	620	46	1.34%

Five coupons were prepared to determine the ultimate tensile strength (f_{fu}) and modulus of elasticity (E_{ft}) of the GFRP bars as shown in Fig. 3-2 (a) following ASTM D7205M-16 (ASTM 2016). The specimen used for testing was fabricated with a gauge length (L_g) of 1000 mm, which was 40 times the diameter of the bar. The anchor length (L_a) should be 460 mm made of 48 mm outer diameter and 32 mm inside diameter steel tube recommended by ASTM D7205M-16 (ASTM 2016). The total length (L_T) of the specimen considering twice the anchor length and free length was 1920 mm. The wooden frame was used as the formwork to fabricate the tensile specimen; anchor pipe was fixed at either end in the wooden frame as shown in Fig. 3-2 (b), the GFRP bar was vertically aligned and

ensured it remains at center during the pouring of epoxy grout.

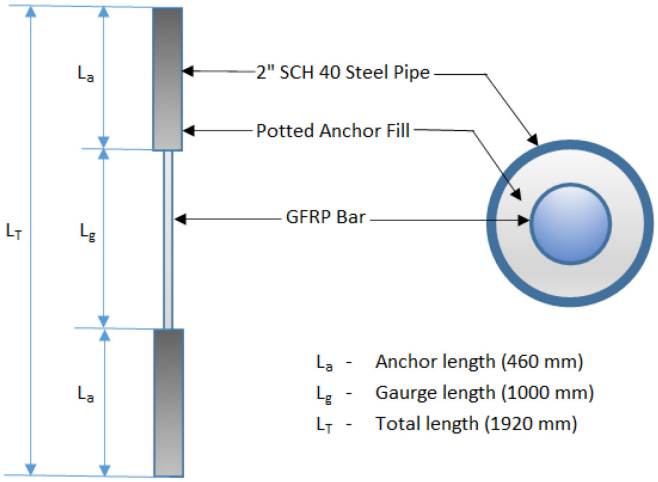

(a)

(b) (c) (d) (e)

Fig 3-2 GFRP tension test set-up: (a) schematic (b) fabrication (c) all fabricated specimens (d) during testing (e) failure

Anchor pipe was drilled with a 3/8" hole on either side along its length to increase the friction between the epoxy grout and inner surface of the pipe, which avoided slippage of the epoxy grout material during tension testing. The gap between the GFRP bar and the

inner side of the steel pipe was filled with epoxy grout at one end, then cured for a minimum of 1 day before being inverted and poured at the other end. After fabrication, all specimens were cured for a minimum of 3 days before being tested in the 2000 kN universal testing machine, as shown in Fig. 3-2 (d). Two strain gauges were attached at the mid of the free length on either side to monitor the strain during testing and the loading rate used was 6.0 mm/min. All strain gauges of the test specimen worked perfectly until the failure except for specimen T4, for which one of the strain gauges failed during the test at 75% stage, and for specimen T5, one of the strain gauges failed during the middle of the test. The GFRP bar's failure in tension was reported in Fig. 3-2 (e), which was observed to be within the free length of the bar between the anchors, and there was no slippage reported in any of the specimens tested.

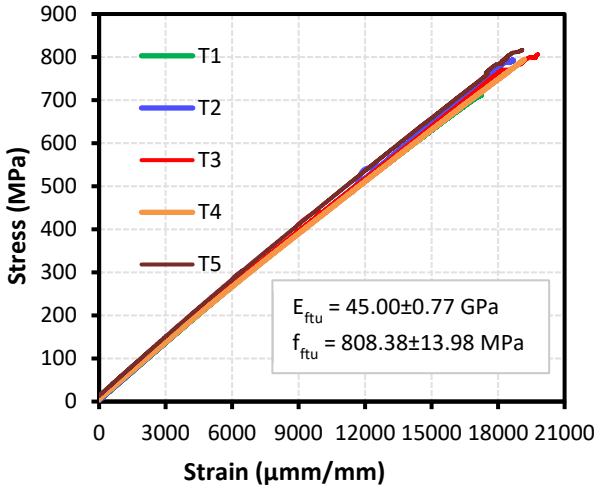

Fig 3-3 Tensile stress-strain of tested GFRP bars

The stress-strain diagram was plotted from the strain data and applied load as shown in Fig. 3-3; the bar's tensile strength was arrived at based on the stress-strain diagram's peak load. The chord modulus of elasticity of GFRP bars in tension was calculated following ASTM 7205M-16 (ASTM 2016) considering the first tensile stress (σ_1) at the strain of 1000 µmm/mm and second tensile stress (σ_2) at 3000 µmm/mm which was reported in Table 3-3. Further, the chord modulus of elasticity was calculated as the ratio of the difference in tensile stress ($\Delta\sigma$) to tensile strain. The ultimate strain of the GFRP bars at peak load was not considered directly as the strain gauge used was not trustable above

10,000 μmm/mm. Hence, the ultimate tensile strain was calculated as the ratio of tensile stress to the modulus of elasticity. The average tensile strength of GFRP bars was 808 MPa, and the average modulus of elasticity in tension was calculated as 45 GPa. From the test results, it was observed that the ultimate tensile stress of the GFRP bar was much higher than the values specified by the supplier.

Table 3-3 Experimental results of GFRP bar tensile testing

Specimen ID	Peak Load (kN)	Tensile Stress (MPa)	Stress σ1 @ Strain 1000 μmm/mm	Stress σ2 @ Strain 3000 μmm/mm	Tensile Stress Difference Δσ (MPa)	Chord Modulus of Elasticity E_{chord} (GPa)
T1	419.32	827.55	47.36	136.56	89.20	44.60
T2	403.69	796.70	48.48	137.56	89.08	44.54
T3	408.72	806.63	54.92	143.53	88.61	44.30
T4	402.39	794.14	51.56	142.38	90.82	45.41
T5	413.90	816.85	59.86	152.19	92.33	4616
Average	**409.60**	**808.38**	**52.44**	**142.44**	**90.01**	**45.00**
SD	7.08	13.98	5.09	6.22	1.54	0.77
COV (%)	1.73	1.73	9.70	4.37	1.71	1.71

*SD = Standard Deviation

*COV = Coefficient of Variation

The compression testing of the GFRP bars was designed and fabricated to test the five specimens of clear length equivalent to two times the diameter of GFRP bars with the bars anchored on either end for the length of four times diameter. The ratio of length to the diameter of the GFRP bar considered for this compression testing was 2. For the GFRP bars' compression testing, there are no specific ASTM standards or test methods that can be followed; hence, a suitable test method was arrived at based on the literature review of the previous researcher's test methods. The pipe size considered was a 4-inch diameter which was comparatively higher than the pipe size specified by ASTM 7205M-16 (ASTM 2016). This size was considered to provide enough compressive strength and material around the GFRP bar to avoid any crushing inside the anchor.

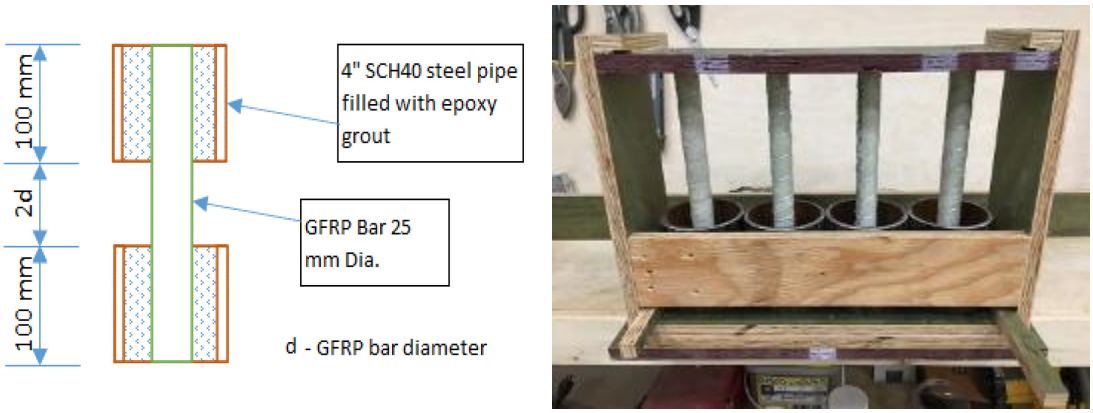

(a) (b)

(c) (d)

(e) (f)

Fig 3-4 GFRP compression test set-up: (a) schematic (b) fabrication (c) all fabricated specimens (d) during testing (e) failure

In the fabrication of test specimens, as shown in Fig. 3-4(b), wooden plywood and plank were used in preparing the framing arrangement by drilling holes in the bottom and top

plywoods to hold the GFRP bars in vertical alignment during the pouring of epoxy between the inner surface of the pipe and GFRP bars. The GFRP bars used were cut by 1.5 inches longer than the actual length required to fabricate the specimen by inserting the bars in the wooden plywood holes and retaining them in the vertical position. The casting of the specimens was carried out in two-stage; the first stage was pouring of epoxy grout for all specimens on one side, which was allowed to cure for one day, after which the other side of the specimen was poured by inverting the wooden arrangement. After curing the epoxy grout, the wooden formwork was dismantled, and the extended end of GFRP and steel pipe and epoxy grout were cut by 15mm to make both the surface flatter and leveled to the plain surface. Two strain gauges were fixed in the clear length on either side along the bar to measure the compressive strain during testing. The strain gauges were connected to the data acquisition system to record the strain for the applied loads. All strain gauges worked perfectly almost until failure for all test specimens. The specimens were tested using the universal testing machine with a capacity of 2000 kN. The adopted loading rate of 0.5 mm/min was applied until the test specimen's failure, as shown in Fig. 3-4(d).

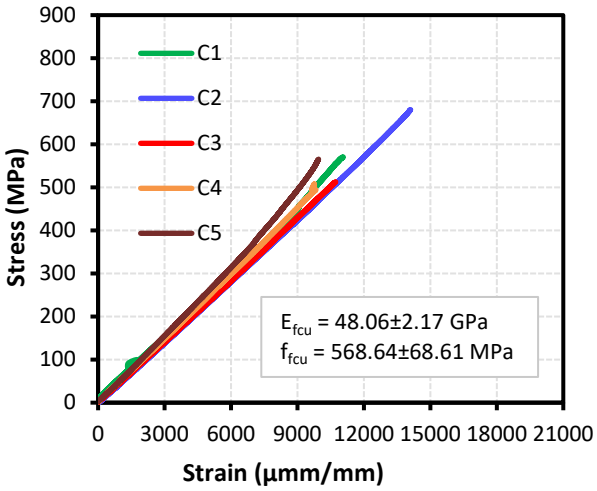

Fig 3-5 Compressive stress-strain of tested GFRP bars

All specimens on compression testing shown the crushing of the GFRP bar exactly at the free end, as shown in Fig. 3-4 (f), and there was no crushing of bar observed either at the end or inside the pipe anchor. The failure at the peak load was sudden, which happened due to the crushing of the bar and breaking of epoxy simultaneously in all specimens. All

test specimens were consistent, as shown in Table 3.4, except the specimen (C2), for which the ultimate tensile stress and the peak load are different from the other specimens.

Table 3-4 Experimental results of GFRP bar compression testing

Specimen ID	Peak Load (kN)	Compressive Stress (MPa)	Stress σ1 @ Strain 1000 μmm/mm	Stress σ2 @ Strain 3000 μmm/mm	Compressive Stress Difference Δσ (MPa)	Chord Modulus of Elasticity E_{chord} (GPa)
C1	289.20	570.75	58.35	152.33	93.98	46.99
C2	345.06	680.99	44.13	137.25	93.12	46.56
C3	259.77	512.67	46.90	140.09	93.19	46.66
C4	260.11	513.34	51.60	148.59	96.99	48.50
C5	286.52	565.46	51.80	155.15	103.35	51.68
Average	**288.13**	**568.64**	**50.56**	**146.68**	**96.13**	**48.06**
SD	34.76	68.61	5.43	7.74	4.34	2.17
COV (%)	12.07	12.07	10.75	5.28	4.51	4.51
Average (W/O C2)	273.09	540.56	52.16	149.04	96.88	48.44
SD (W/O C2)	16.16	31.89	4.71	6.54	4.62	2.31
COV (%) (W/O C2)	5.61	5.61	9.31	4.46	4.80	4.80

*SD = Standard Deviation

*COV = Coefficient of Variation

From the applied load and strain data received, typical stress-strain behavior, as shown in Fig 3-5, was plotted to determine the ultimate compressive stress and modulus of elasticity. The stress-strain behavior was observed to be linear, and the strain reading from either side of the GFRP bar recorded similar reading, which confirmed that the load was applied concentrically on the GFRP bar. Similar to tensile testing, the chord modulus of elasticity in compression for all test specimens as shown in Table 3-4 was calculated as the slope of linear elastic part of the stress-strain curve considering the corresponding first compressive

stresses at the strain of 1000 μmm/mm and second compressive stress at the strain of 3000 μmm/mm following ASTM 7205M-16 (ASTM 2016). The ratio of the difference in the compressive stress (Δσ) to compressive strain was used to determine the chord modulus of elasticity. From the average peak load of 288 kN and average compressive stress of 569 kN from the compressive testing, it should be noted that the GFRP bar can sustain the compressive load, which was 70% of the tensile load, which makes the compressive to tensile ratio as 0.7. This new compressive testing method had resulted in the crushing failure of GFRP bars at the free end consistently without causing any premature failure or crushing at the end or inside the anchor, which facilitated the compressive strength and elastic modulus that can be reliable and comparable with the tensile properties of GFRP bars.

3.3 Specimen Fabrication

All cages for nine beam specimens shown in Fig 3-6 were assembled in the Heavy Structure lab at Dalhousie University. Initially, stirrups for the beams were assembled on a table fixed with wooden planks at 280 mm in the horizontal direction and 380 mm in the vertical direction. C-shaped stirrups were assembled for the required outer to outer dimension alignment of 280 mm horizontally and 380 mm vertically, tied using tie-wraps at top and bottom to make it a rectangular stirrup. The longitudinal horizontal bars were laid horizontally between the two tables, placed at a distance to support the cage assembly. The stirrups were then inserted from one end and then tightened using tie-wraps by placing them at 150 mm spacing at the midspan and end span of the beam with dense stirrups at 75 mm spacing at end span to avoid the failure of the beam due to shear. Finally, the spacer bars were fixed above the FRP bars' bottom layer to assemble the second layer of the longitudinal bars from the beam bottom. The electrical strain gauges that are to be attached to GFRP were marked on the longitudinal bars, which was then followed by removing the sand coating layer of the GFRP, grinding the deformed bar ribs, and cleaning to install the strain gauges using special glues to establish proper bonding between the bar and strain gauge.

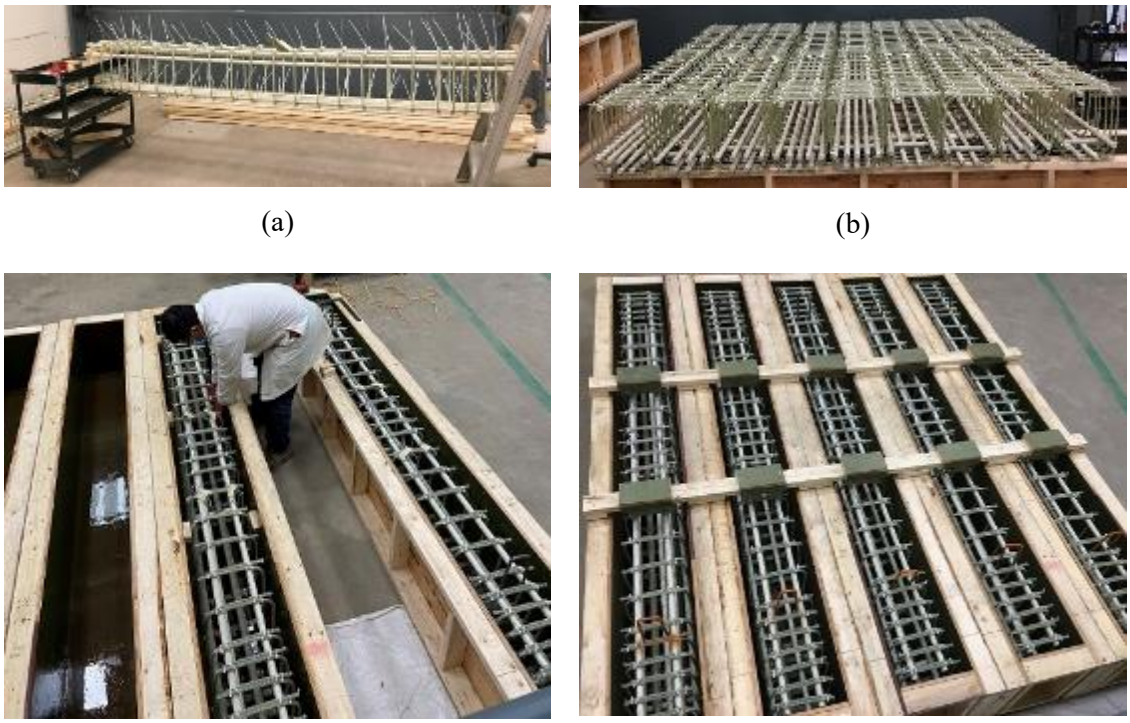

(a) (b)

(c) (d)

Fig 3-6 GFRP beam fabrication: (a) cage assembly (b) cages for all specimens (c) placing cages in formwork (d) assembled cage and formwork before concreting

The formworks made of plywood have been constructed to cast all nine beam specimens at the same time. It was planned to ensure that the condition and geometry remain the same for all beams. The formwork was made to cast the beam horizontally to reach the bottom-most portion of each beam and facilitate vibrating of the beam throughout the length during concrete pouring and casting. The cage assembly was inserted into the wooden formwork prepared for casting the beam and was aligned to achieve a 25 mm concrete cover around all faces of the beam. The concrete was then poured into the formwork, as shown in Fig 3-7, and the electrical vibrator was used simultaneously to maintain the proper distribution of the concrete. During concreting, extreme care was taken to avoid any reinforcement cage movement and damages to strain gauges or connected wires. Nine concrete cylinders were prepared in the same concrete mix. All finishing of the concrete surfaces was shaped to look smooth and was covered with a polythene sheet. Further to the casting of GFRP beams and concrete cylinders, the curing process was initiated in the following day to maintain the wetness of the concrete surface for seven days.

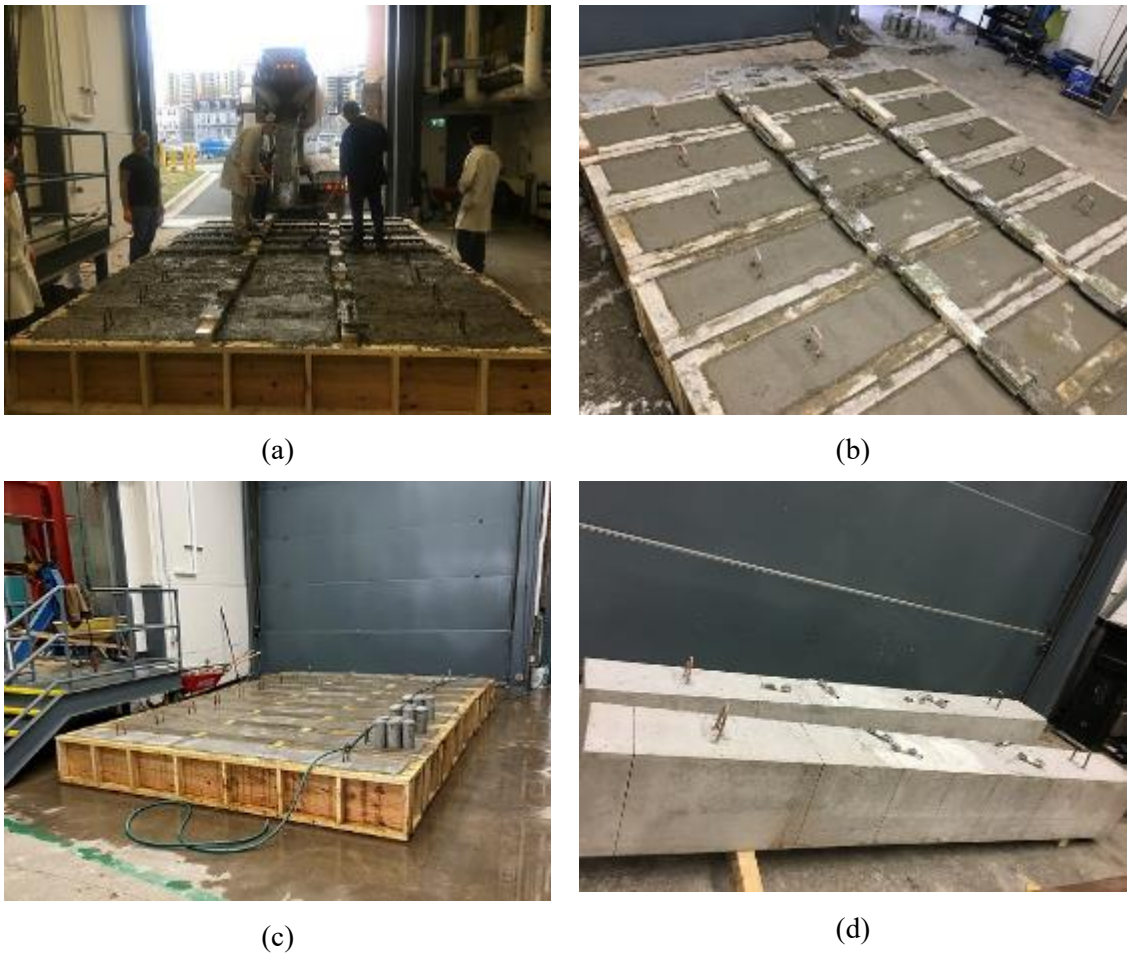

(a) (b)

(c) (d)

Fig 3-7 GFRP beam casting: (a) concrete pouring (b) specimens after concreting (c) curing (d) casted specimens

3.4 Instrumentation and Test Set-up

A total of nine full-scale simply supported beam specimens were tested under four-point bending with a clear span of 2800 mm, allowing the overhang of 125 mm on either end. Both the ends of the specimens were protected with steel cover plates mainly fabricated for proper confinement and to prevent the beams' premature failure at the ends or outside the support locations.

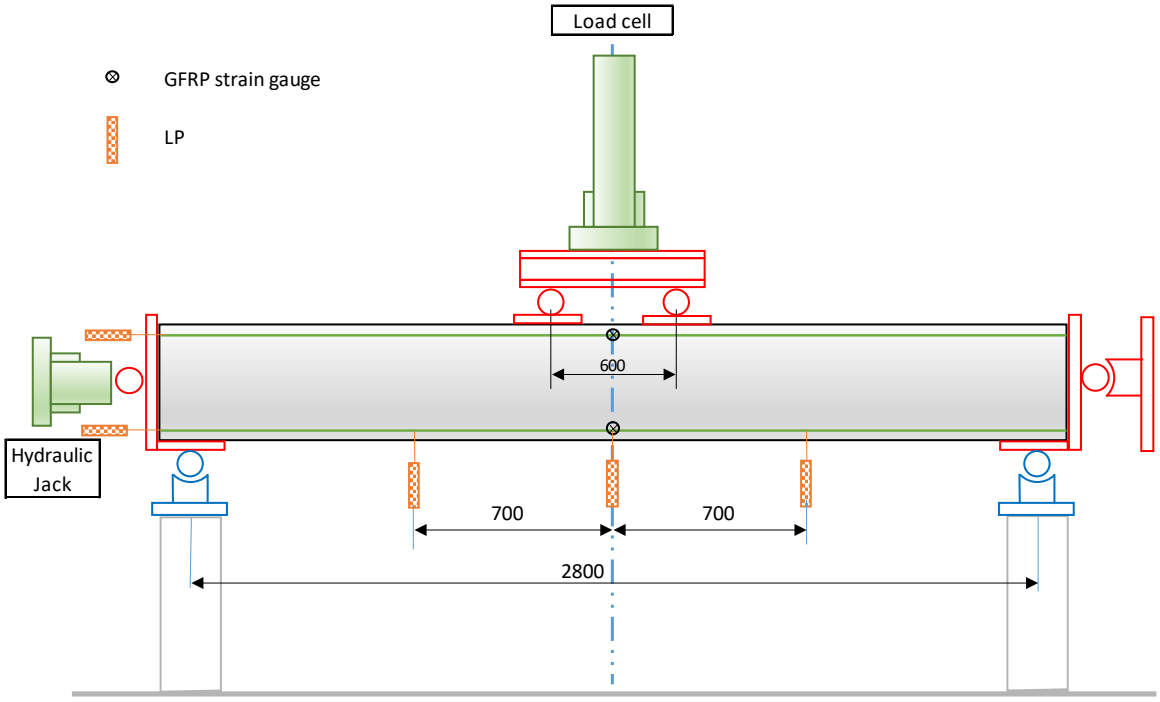

(a)

(b)

Fig 3-8 GFRP beam test set-up and instrumentation details (a) schematic (b) actual (dimension in mm)

On the other hand, the applied load was increased in small increments to measure the load and deformation. The vertical load perpendicular to the simply supported beam was applied using a 1000 kN hydraulic actuator with a 5.0 mm/min displacement rate. The horizontal load was applied longitudinally using another actuator to the center of the beam at one end and was monitored using a load cell. The GFRP beam was instrumented as shown in Fig. 3-8 to analyze the behavior due to displacement, tensile and compressive strain. The vertical displacement at the quarter, midspan, and three-quarter of the beam was measured using the linear variable different transducers (LVDT). The horizontal displacement was measured at one end of the beam using LVDT, which was mounted on either side. To measure the changes in the compressive and tensile strain of the GFRP reinforcement, a total of 4 electrical resistance strain gauges were attached correctly to longitudinal bars. Two strain gauges were installed on the top longitudinal compression bars at the beam midspan. For the bottom longitudinal bars under tension, two strain gauges were installed at the beam's midspan. During the testing process, the applied horizontal and vertical loads, GFRP strain, vertical and horizontal displacements were monitored. Their results were recorded using the data acquisition system connected to the computer.

3.5 Experimental Test Results and Discussion

In this section, the test specimens' most significant experimental results were investigated in terms of failure modes, load-deformation behavior, load-strain behavior, moment-curvature behavior, and axial load-moment behavior. The test specimen's ultimate moment capacity at their load corresponding to ultimate concrete strain at extreme concrete fiber at the compression zone, their tensile strain, quarter-span, and mid-span deflections are presented in Table 3-5. The moment listed in Table 3-5 was calculated based on the applied lateral load from the test data multiplied by shear span, plus the corresponding vertical deflection times the axial load applied for the specimens tested with 2 % and 4% axial load. There was no premature failure observed while testing any of the nine beam specimens. By comparing the ultimate bending resistance, three test specimens' test results, B-R1.7-P0, B-R2.5-P4, and B-R3.3-P4, were not as expected. In B-R1.7-P0, the beam at pure bending failed at a relatively lower load than predicted values from the analytical model, whereas test specimens B-R2.5-P0 and B-R3.3-P4 failed at higher load when subjected to

the axial load of 4 %.

Table 3-5 Test results summary

Sl. No.	Specimen ID	Reinforcement Ratio (%)	Axial Load (kN)	Peak Load (kN)	Mu (kNm)	Mid-span Vertical Deflection (mm)	Mode of Failure
1	B-R1.7-P0	1.7	0	454.0	248.7	33.8	CC*→SF
2	B-R1.7-P2	1.7	125	488.0	268.4	37.2	CC→SF
3	B-R1.7-P4	1.7	250	498.3	274.1	34.7	CC→FC
4	B-R2.5-P0	2.5	0	550.6	302.8	33.3	CC→SF
5	B-R2.5-P2	2.5	125	508.4	279.6	27.2	CC→SF
6	B-R2.5-P4	2.5	250	555.7	305.7	31.0	CC→SF
7	B-R3.3-P0	3.3	0	587.2	323.0	26.9	CC→SF
8	B-R3.3-P2	3.3	125	559.1	307.5	26.1	CC→SF
9	B-R3.3-P4	3.3	250	641.9	353.1	28.3	CC*→SF

SF = Shear Failure

CC = Concrete Crushing

FC = FRP Crushing

* = Concrete crushing was not visible during the test, but the extrapolated value of concrete strain reached 3000 μmm/mm

The possible source of error observed during the testing was the movement of the testing frame outward by 3 mm due to the axial load applied. The testing frame moved upward caused the slip in the load, which the fluctuation can see in the plotted strain diagram in some cases, center to center of the beam support location were out by ± 5 mm, variation in the shape and dimension of the c-shaped stirrups, load eccentricity in the applied axial load at either end of the beam by ±5 mm, fluctuation in the applied axial load by ±2 kN and due to the variation in the thickness of the grout bags. The following section explains the specimen's behavior during testing, failure pattern, and the resulting outcome.

3.5.1 Failure Modes

The GFRP beams were designed as an over-reinforced section in this research with preferred failure mode as concrete crushing when the maximum compressive strain of the concrete reaches 3000 μmm/mm according to ACI 440.1R-15 (ACI 2015). Based on the experimental testing of the beam specimens, three types of failure mode were experienced by nine beams, out of which six beams had exhibited similar failure pattern by typical concrete crushing as the primary mode of failure, which occurred once the concrete reached the ultimate compressive strain of 3000 μmm/mm and followed by shear failure as the secondary failure.

B-R1.7-P0

B-R1.7-P2

B-R1.7-P4

Fig 3-9 Failure Pattern – Beams with 1.7% Reinforcement Ratio

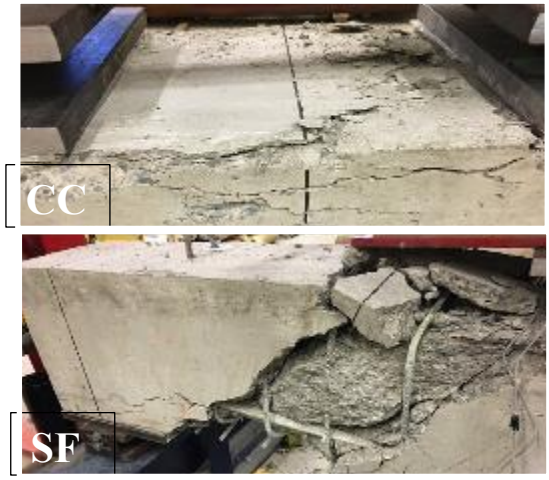

B-R2.5-P0

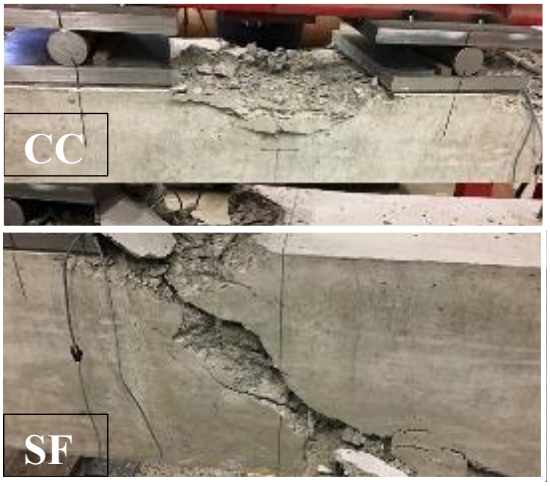

B-R2.5-P2

B-R2.5-P2

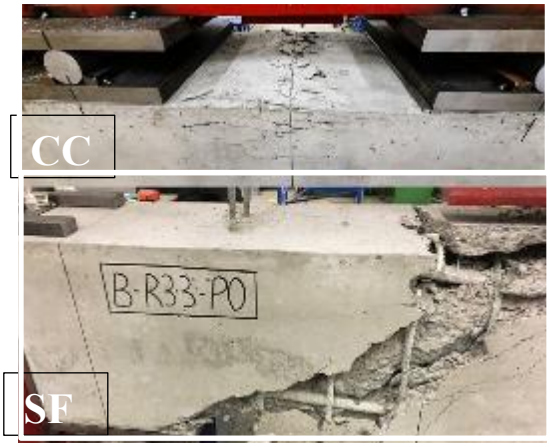

B-R3.3-P0

B-R3.3-P2

B-R3.3-P4

Fig 3-10 Failure Pattern – Beams with 2.5% and 3.3% Reinforcement Ratio

One beam failed by flexure by crushing of concrete at top compressive zone at the center whereas the other two beams failure mode were not by concrete crushing even after exceeding the ultimate compressive strain, but the beams had abruptly failed in shear by GFRP rupture. All three types of failure patterns – concrete crushing, flexure, and shear failure are shown in Fig. 3-9 and Fig. 3-10. When the concrete crushing happened at the top compression zone of the GFRP beam at the center, the concrete strain was higher than 3000 μmm/mm specified by ACI 440.1R-15 (ACI 2015). The failure mode of the test specimens was designed as an over-reinforced FRP beam to exhibit concrete crushing as a failure pattern according to ACI 440.1R-15 (ACI 2015) when the calculated reinforcement ratio (ρ_f) was greater than the balanced reinforcement ratio (ρ_{fb}) based on the equation (3-1) and (3-2).

$$\rho_f = \frac{A_f}{bd} \qquad (3-1)$$

$$\beta_1 = \frac{A_f f_{fu}}{0.85 f'_c bc} \qquad (3-2)$$

$$\rho_{fb} = 0.85\beta_1 \frac{f'_c}{f_{fu}} \frac{E_f \varepsilon_{cu}}{E_f \varepsilon_{cu} + f_{fu}} \qquad (3-3)$$

where: b = width of the beam

d = effective depth of the beam

A_f = area of FRP reinforcement

f'_c = concrete compressive strength (MPa)

f_{fu} = FRP tensile strength (MPa)

E_f = modulus of elasticity of FRP reinforcement (MPa)

ε_{cu} = ultimate concrete strain (μmm/mm)

β_1 = factor for equivalent stress block depth

The failure pattern of all the nine-testing specimen was similar with the initial formation of vertical cracks in the constant moment region from the bottom concrete fiber perpendicular to the longitudinal reinforcement at the midspan, which was then followed by the propagation and widening of flexural cracks and development of vertical cracks at

shear span with the increase in loading. The lower reinforcement ratio cracks are more compared to the beams with a higher reinforcement ratio. The GFRP beams continued to sustain the higher load until the maximum strain of the concrete reaches the ultimate limit, which corresponds to the maximum flexural capacity at which the concrete in the top compression zone cracked and crushed.

3.5.2 Load – Deflection Behavior

The deflection of the GFRP beam was the most significant parameter measured using the linear potentiometer (LP) attached to the beam's bottom during the specimen testing. Variation of deflection was captured by one at both quarters spans and two at mid-span. Additionally, the string pot was attached at the bottom center of the mid-span to verify the linear potentiometer's deflection.

The deflection for the load variation during testing was measured using the data acquisition system connected to the testing machine. Each deflection curve represents the average of deflection from the two LP's were plotted against the load in Fig 3-11 predicting the load-deflection curve for test specimen plotted for reinforcement ratio of 1.7%, 2.5%, and 3.3% against the pure bending and axial load of 125 kN and 250 kN. The deflection of all test specimens before cracking was minimal as expected, and after post-cracking, there was a sudden increase in deflection. There were noticeable fluctuations in most of the deflection curves during concrete crushing. The sudden drop in the load had created the decrease in deflection, which gradually increased later as the GFRP bars actively contributed to sustaining the further applied load until the test specimen's failure either by shear or flexure.

(a)

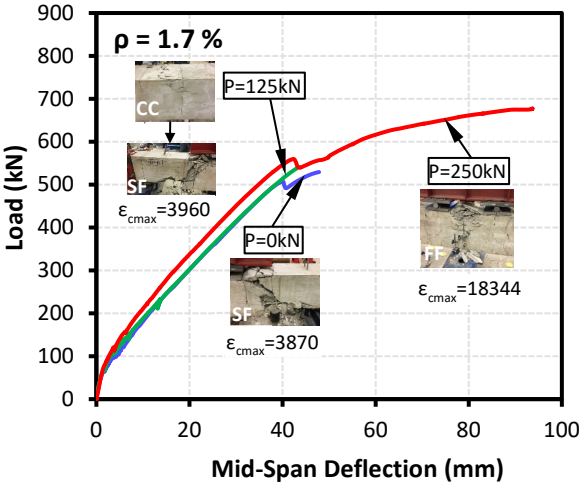

(b)

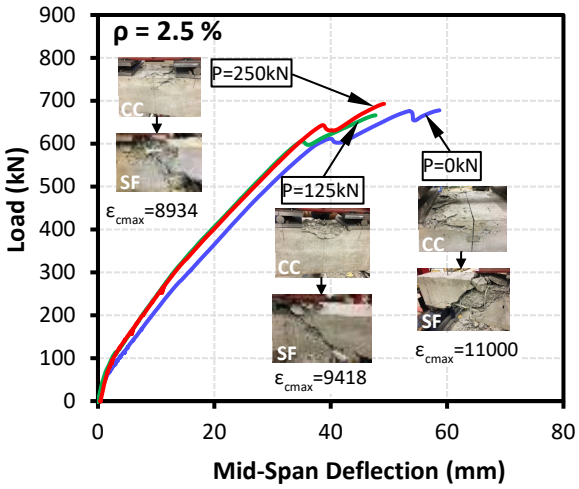

(c)

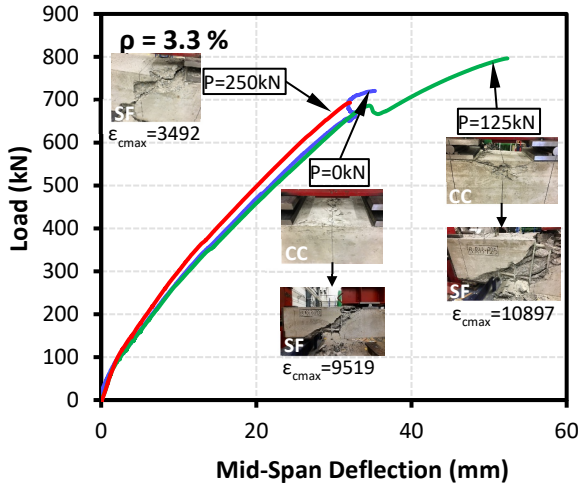

Fig 3-11 Load vs deflection curve at mid-span (a) ρ = 1.7% (b) ρ = 2.5% (c) ρ = 3.3%

In Fig 3-11, the curve fluctuation corresponds to concrete crushing, and the endpoint of each curve corresponds to the failure of the test specimen at peak load. From the load-deflection curve, it was visible that the reinforcement ratio directly governing the beam deflection behavior, and the increase of stiffness in the GFRP beam with the reinforcement ratio decreased the deflection. The test specimens subjected to pure bending experienced lesser deflection than the test specimen with a low axial load of 2% and 4%, which had higher deflection, as shown in Fig 3-11.

3.5.3 Load – Strain Behavior

The two-point loads applied at the mid-span through four-point bending of the GFRP beam had created the bending moment and deflection, directly corresponding to the compressive strain in the top layer and tensile strain in the bottom layer of GFRP bars. Two strain gauges mounted at the top compression layer of the GFRP bars at the mid-span top location to monitor the compressive strain and two strain gauges mounted at the outer bottom layer of GFRP bars bottom face on either end to monitor the tensile strain at mid-span.

All the strain gauges mounted inside the concrete beam before pouring the concrete had registered the consistent reading during the experimental testing process. The readings from the strain gauges were recorded through the data acquisition system connected to the testing machine. The increase of load had subsequently increased the strain, which can be observed from the load-strain diagram shown in Fig 3-12 plotted based on the average strain of two strain gauges at the top and two strain gauges at the bottom. There was no noticeable reading shown from the strain gauges until the initiation of cracks in the concrete, after which there was a drastic jump in the strain gauge reading recorded. From the tested specimens, the average ultimate tensile strain reached by the bottom layer of GFRP bars was 13000 μmm/mm, whereas the average ultimate compressive strain reached by the top layer of GFRP bars was 7000 μmm/mm. The test specimen B-R1.7-P4 experienced the maximum compressive strain of 10000 μmm/mm before the failure of GFRP bars in crushing at the compression zone.

(a)

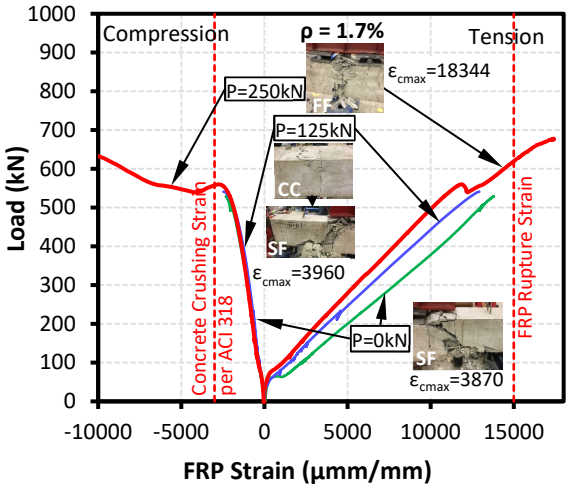

(b)

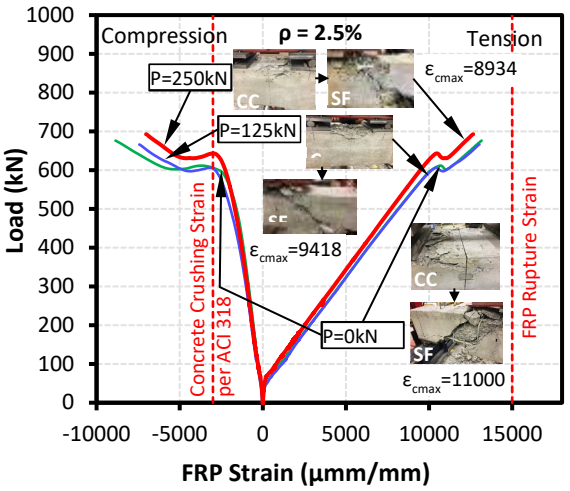

(c)

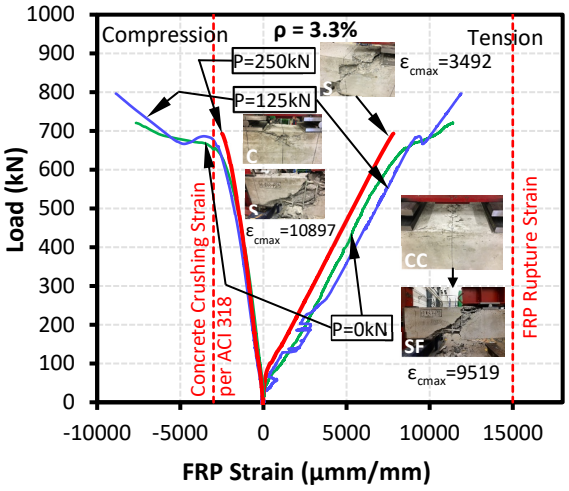

Fig 3-12 Load vs GFRP strain at mid-span (a) ρ = 1.7% (b) ρ = 2.5% (c) ρ = 3.3%

The highest tensile strain recorded was 17000 μmm/mm for test specimen B-R1.7-P4, and the highest compressive strain recorded was 15000 μmm/mm for test specimen B-R1.7-P4. The compressive and tensile strain of the GFRP bars had shown linear behavior until it reached the first peak load at which the concrete crushes and further extends with semi-linearity until it reaches the beam's ultimate bending resistance, after which failure happens either by flexure or shear. Fig 3-12 shows that tensile strain in the GFRP bar had decreased with the increase of reinforcement ratio from 1.7% to 3.3%. The test specimen with a 1.7% reinforcement ratio had shown a sharp tensile strain increase compared to the other specimens with a higher reinforcement ratio. The impact of the axial load was minimal; however, there is a noticeable difference in the tensile strain, which had differentiated the curve for zero, 125 kN, and 250 kN axial load. In the case of both compressive and tensile strain, GFRP bars were well below the ultimate strain until it reaches the first peak load of concrete crushing followed by a load drop of around 6 to 8%, further, increase of load caused the GFRP bars to reach the ultimate strain at second peak load resulting in the shear failure of concrete and GFRP rupture of the longitudinal bar at the top.

Fig 3-13 shows the concrete strain in the extreme concrete fiber of compression zone for all test specimens at mid-span based on reinforcement ratios of 1.7%, 2.5%, and 3.5%. No separate strain gauge was used to measure the concrete strain in this testing process; however, two strain gauges mounted in the top layer of the GFRP bars recorded the compressive strain during the testing process were used to calculate the concrete strain. As the strain profile was linear, any particular load's neutral axis was determined using the compressive and tensile strain in the GFRP bars. With the neural axis and compressive strain, the compressive strain of concrete was determined by extrapolation by a similar triangle method. From the nine GFRP beam test performed, all the specimens had surpassed the ultimate concrete strain of 3000 μmm/mm, however, seven specimens had shown the concrete crushing as the primary mode of failure, which was noticed to happen at the concrete strain range of 3000 μmm/mm to 3500 μmm/mm.

(a)

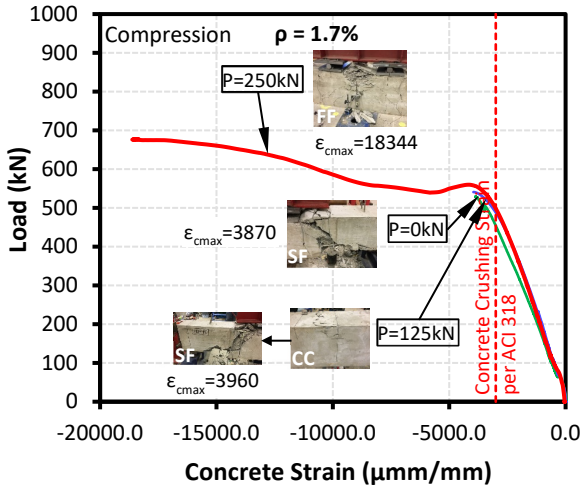

(b)

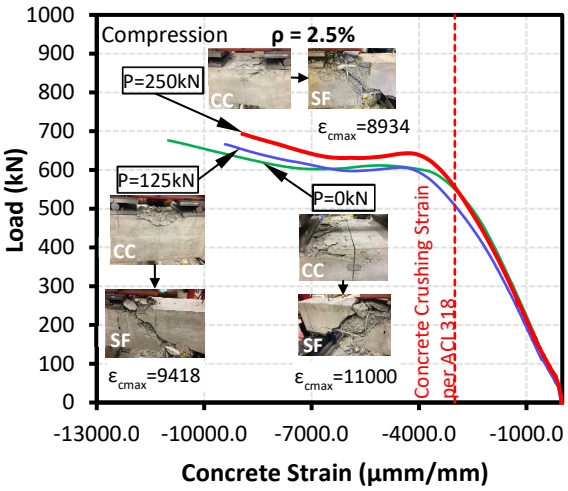

(c)

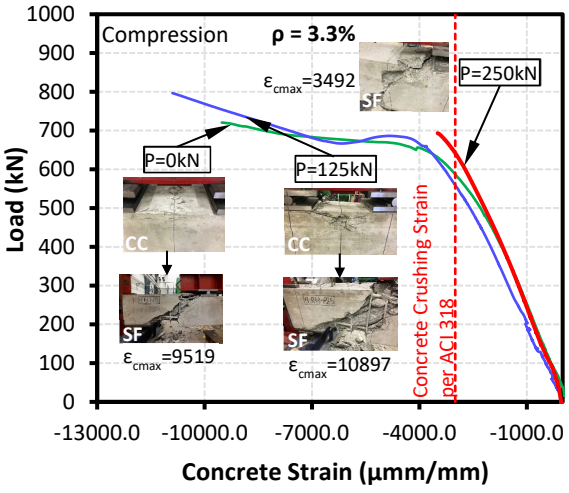

Fig 3-13 Load vs extreme concrete strain (extrapolated) at mid-span (a) ρ = 1.7% (b) ρ = 2.5% (c) ρ = 3.3%

From Fig 3-13, it was noticeable that the concrete strain curve was steeper and linear until concrete crushing at first peak load; however, the indirect concrete strain from GFRP strain had shown semi-linearity between the first peak load and before the failure due to the second peak load. Furthermore, the concrete strain had a minimal increase with the axial load's intrusion to the tested specimen. At a lower reinforcement ratio, the concrete strain had reached the ultimate strain earlier than the test specimens with a higher reinforcement ratio.

3.5.4 Moment – Curvature Behavior

Fig 3-14 illustrates the moment-curvature behavior of the GFRP reinforced concrete beams subjected to combined bending and low axial loading, which was tested under four-point bending. The variation of load applied as transverse and axial load to the beam affects the cracking load and curvature, which further results in the neutral axis variation. The curvature for any particular load was calculated using sectional analysis by finding the difference in the average experimental tensile and compressive strain of the GFRP bars divided by difference in depth (d) of strain gauge location using Eq 3-3.

$$\varphi_m = \frac{\varepsilon_{ft} - \varepsilon_{fc}}{s_d} \qquad (3-3)$$

where: ϕ_m = curvature at mid-span (rad/km)

ε_{ft} = average tensile strain in bottom GFRP bar (μmm/mm)

ε_{fc} = average compressive strain in top GFRP bar (μmm/mm)

s_d = distance between the strain gauges in the top and bottom reinforcement (mm)

The behavior of moment-curvature was similar to the behavior of FRP and concrete strain. The moment-curvature curve had shown the linear behavior with the first peak load fluctuation due to concrete crushing from all the tested specimens. The curve continued with the linear behavior further until failure due to flexure or shear at second peak load.

(a)

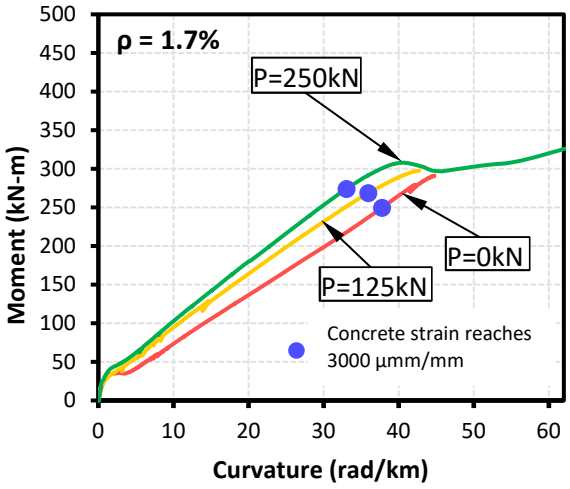

(b)

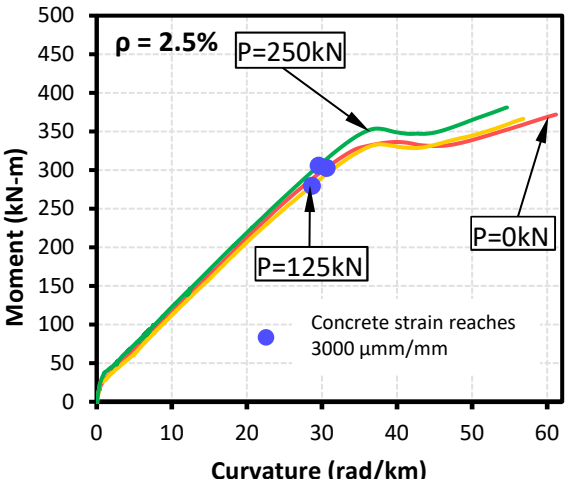

(c)

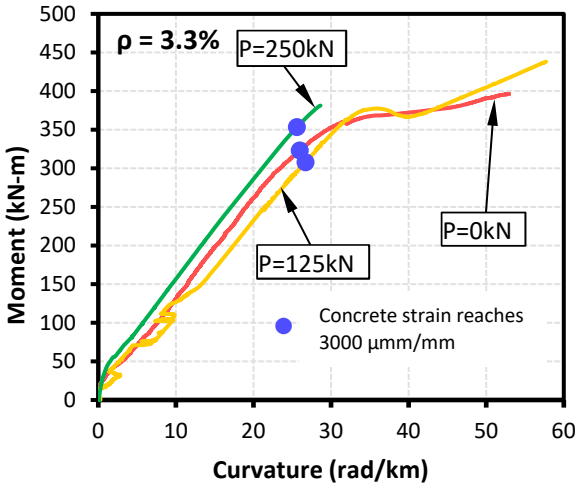

Fig 3-14 Moment vs Curvature at mid-span (a) ρ = 1.7% (b) ρ = 2.5% (c) ρ = 3.3%

Alternatively, the GFRP specimen reached its ultimate bending resistance, where the

equilibrium was reached when the tested specimen reaches the ultimate concrete strain at the first peak load. There was a drop in the load, which happened at the first peak load due to concrete crushing; however, the GFRP beam was able to sustain a higher load with an increase in bending resistance because of GFRP bars contribution until the second peak load where the GFRP ruptures. The curvature had increased gradually with the growth of compressive strain in the GFRP bars, which had contributed to compression comparatively higher than the concrete resulting in the increased bending resistance of the beam climbing upward until the GFRP bar fails in compression. The highest curvature of the tested beams was 91.2 rad/km from specimen B-R1.7-P4. It failed in flexural, which had experienced the higher deflection before the concrete crushes completely in the mid-span compression zone. The lowest curvature was 28.5 rad/km from specimen B-R3.3-P4, which failed abruptly in shear before the concrete crushing. However, the curvature was directly proportional to the beam's deflection; in comparison, the higher deflection beam had experienced more curvature. Furthermore, the increase in moment capacity was more pronounced with the increase of the reinforcement ratio from 1.7% to 3.3%, which might be directly due to the rise in the beam's stiffness.

3.5.5 Neutral Axis Depth Behavior

Fig 3-15 compares the tested specimen's neutral axis with the reinforcement ratio of 1.7%, 2.5%, and 3.3% under zero, 2%, and 4% axial load. All the neutral axis are calculated from the mid-height of the GFRP beam based on the test data. The average of compressive strain in the top strain gauge and average of tensile strain in the bottom strain gauge was used to determine the neutral axis location from the following equation (3-4) from the acquired recordings of strain data.

(a)

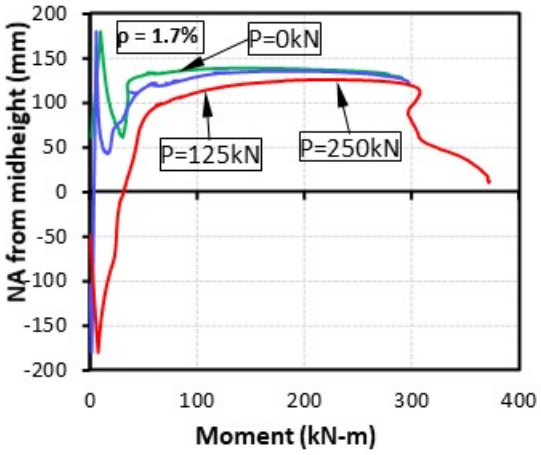

(b)

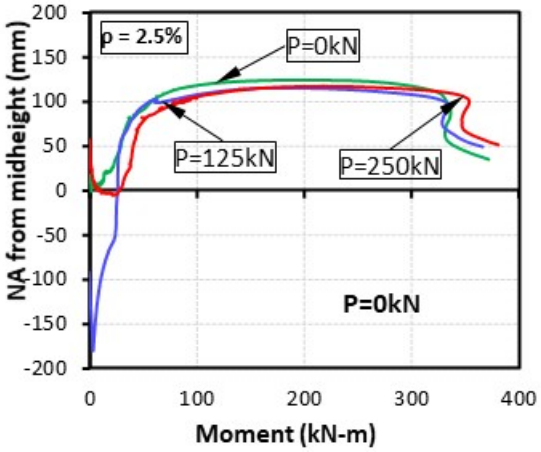

(c)

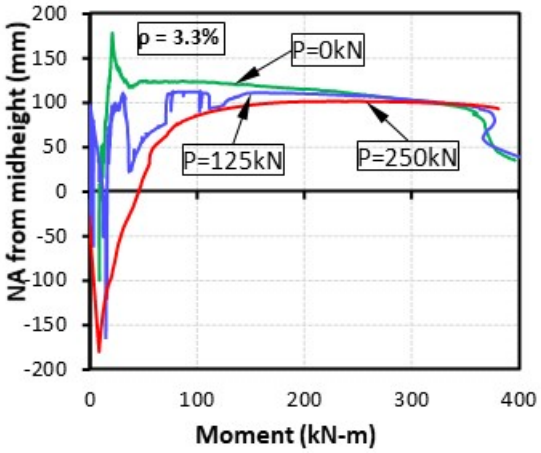

Fig 3-15 Neutral Axis vs Moment at mid-span (a) ρ = 1.7% (b) ρ = 2.5% (c) ρ = 3.3%

$$\text{NA} = \left[\frac{h}{2}\right] - \left[\left[\frac{\varepsilon_{fc}}{\varepsilon_{fc}+\varepsilon_{ft}}\right] s_d + d_s + \text{cover}\right] \qquad (3-4)$$

where: NA = neutral axis

ε_{ft} = average tensile strain in bottom GFRP bar (μmm/mm)

ε_{fc} = average compressive strain in top GFRP bar (μmm/mm)

s_d = distance between the strain gauges in the top and bottom reinforcement (mm)

ds = diameter of stirrups (mm)

In terms of the neutral axis, applying the axial load had a marginal effect of lowering the neutral axis compared to the test specimen under pure bending. However, there was no change in the neutral axis pattern in any of the tested specimens.

3.5.6 Axial Load – Moment Behavior

The effect of low axial load applied to the GFRP beam subjected to four-point bending was the fundamental purpose of this research studied and compared as shown in Fig 3-16. There were three different reinforcement ratios of 1.7%, 2.5%, and 3.3% compared with zero, 125 kN, and 250 kN axial load, which was 2% and 4% axial capacity of the beam. With nine test specimens, the low axial load was applied to six specimens using a hydraulic actuator, which was mounted on both the end of the beam; the axial compressive load was applied initially load was maintained throughout the test with the error of ±2 kN. The test specimen's ultimate bending resistance was calculated from the applied load corresponding to the ultimate concrete strain of 3000 μmm/mm. Compared to the different reinforcement ratios, the ultimate bending resistance trend with low axial load showed a similar behavior pattern. The data points of each test were plotted in P-M interaction diagram and observed that the ultimate bending resistance of the beam at pure bending decreased with the induced axial load of 125 kN (2%) to the beam; however, the ultimate bending capacity increased when the induced axial load was increased to 250 kN (4%).

(a)

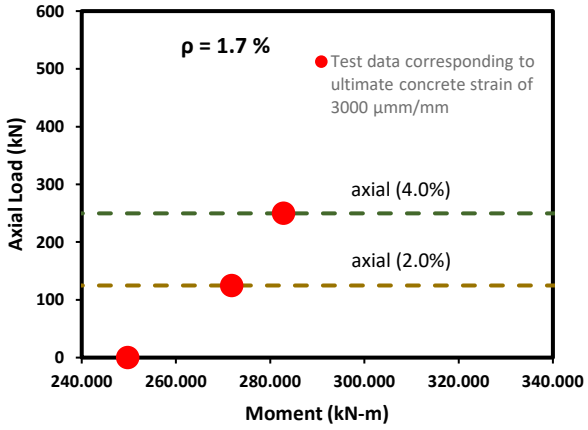

(b)

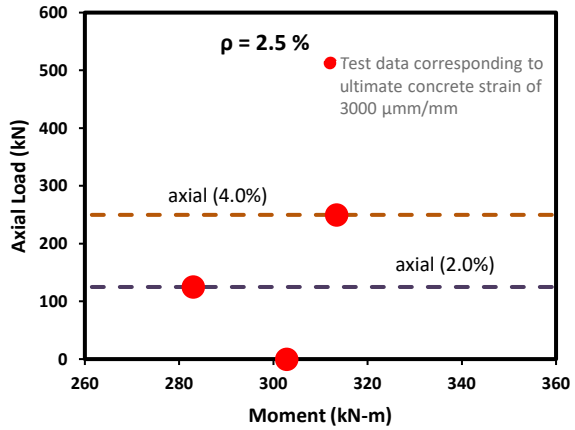

(c)

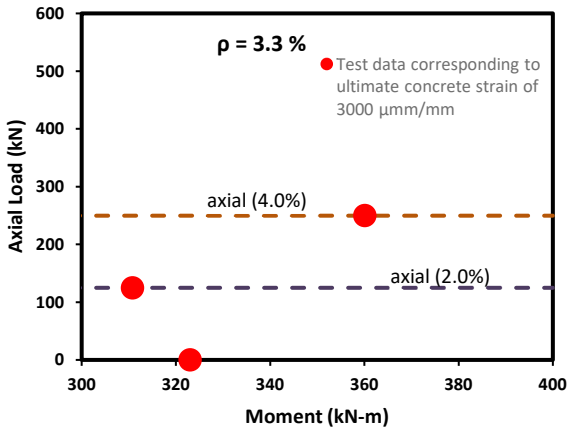

Fig 3-16 Axial load vs Moment at mid-span (a) ρ = 1.7%
(b) ρ = 2.5% (c) ρ = 3.3%

CHAPTER 4 ANALYTICAL STUDY

The current research analytical model was developed for the GFRP reinforced concrete beam, which was verified using the experimental investigation and justifies the results presented in Chapter 3 of this thesis. This analytical model was further verified through the parametric study conducted in the following sections of this chapter. In this analytical study, the model was created to analyze the GFRP reinforced beam under bending and low axial compressive load. From the recent research and design codes, it is well known that GFRP bars' contribution in compression was yet to be determined, and, hence, the consideration in design is completely ignored. The outcome of the result presented from the analytical model demonstrates that ignoring the low axial compressive load in the GFRP reinforced beam subjected to flexure causes design failure. The effect of axial compressive load should be considered while finding the bending capacity of the GFRP beam, which directly affects the strength of the actual beam.

4.1 Failure Criteria

The analytical model developed for the P-M interaction diagram accounts for the following failure due to the materials. The type of failure that was considered as part of this model was (i) crushing of concrete in compression at a compressive strain of 3000 μmm/mm following ACI 440.1R-15 (ACI 2015) (ii) GFRP rebar failure due to tensile rupture reaches the ultimate tensile strength (f_{ftu}) of 808 MPa or crushing of GFRP rebar in compression reaches the ultimate compressive strength (f_{fcu}) of 568 MPa. While the first option was the preferred mode of failure, the test specimens were designed and fabricated as over-reinforced. The tension side's GFRP bars are provided with the reinforcement ratio higher than the balanced reinforcement ratio to ensure the concrete crushing in compression. The GFRP beam's failure was initiated by concrete crushing at the top mid-span, which was then be followed by FRP rupture of FRP compression as the flexural failure. The GFRP test specimens were provided with adequate shear reinforcement to ensure the first mode of failure as a flexural failure by concrete crushing and to avoid any premature shear failure.

4.1.1 Axial and Bending Failure

The analytical model was developed to describe the axial load versus bending moment interaction diagram and determine the capacity of the beam under lower axial load according to the design provisions and the guidelines mentioned in ACI 440.1R-15 (ACI 2015) and CSA S806-12 (CSA 2012). The procedure used for the computation of axial load and bending moment was followed with the same procedure as a concrete beam with steel reinforcement. The interactive diagram shape for the GFRP beam was not the same as the steel reinforced beam, which was entirely different due to the material behavior. There are three main zones for the steel-reinforced beams: 1) compression-controlled failure due to crushing of concrete, 2) both compression of the concrete reaches the maximum ultimate compressive strain and tension of the reinforcement reaches the maximum ultimate tensile strain, 3) tension-controlled failure due to yielding of steel reinforcement. In the GFRP beam interaction diagram, the failure cannot be differentiated by zone, which was by linear elastic failure.

The concrete model proposed for the research was explained in Fig-4.1 shows the strain profile and the parabolic stress diagram with the appropriate symbols. The beam cross-section consists of three layers of longitudinal reinforcement, out of which one layer was top compression reinforcement, and two layers are bottom tension reinforcement. The longitudinal reinforcement in the beam cross-section was tied together by two C-shaped stirrups at an equally placed distance of 150 mm center to center at the mid-span and 75 mm center to center at the end span. The spacing between the bottom longitudinal reinforcement was controlled by a spacer bar spaced at regular intervals. In the below figure, beam length, width, cross-sectional area, effective depth, location of the rebar layer, and neutral axis are represented in a short form as “b”, ”h”, ”A”, ”d”, ”d_1” and “c”

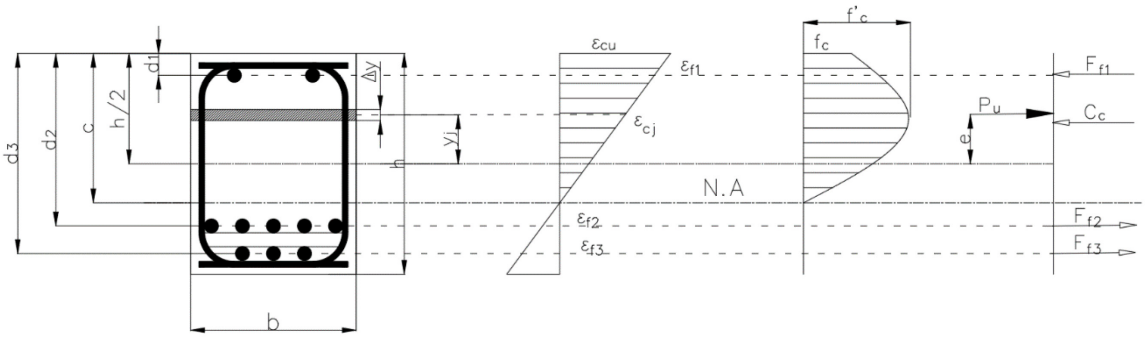

Fig 4-1 Stress and strain profile of GFRP beam cross-section

4.1.1.1 Assumptions

In ACI 440.1R-15 (ACI 2015), it was mentioned to avoid relying upon FRP bars to resist the compressive forces because of the lower elastic modulus, whereas CSA806-12 (CSA 2012) allows for the use of FRP bars in compression member without considering the compressive strength of the bar in design. It was understood from the code CSA806-12 (CSA 2012) that it has a higher limitation in the usage of GFRP bars in compression. This model's first step was a cross-section analysis of the GFRP beam subjected to combined flexure and axial compression experience the strain gradient, which was determined using the stress-strain curve method. The procedure followed was the same as the traditional steel-reinforced concrete beam method, except the type of reinforcement analyzed was GFRP. The beam cross-section was considered to be divided into concrete fibers of 20 segments with equal thickness. Furthermore, it was also verified that dividing the beam into more segments does not impact predicted axial compression and bending moment accuracy. The concrete was considered only to resist the compression, whereas the tensile stress in concrete was completely ignored. Hence, the concrete below the neutral axis was assumed to be cracked with no contribution to the moment resistance.

It was assumed that full composite action exists between concrete and GFRP so that the strain profile was linear throughout the section from the top-end compressive face to the bottom end tensile face of the beam. The ultimate concrete strain limitation of the extreme concrete fiber at the beam top was 3000 μmm/mm as per ACI 440.1R-15 (ACI 2015). The

GFRP bar ultimate axial tensile strain was determined using the following equation:

$$\varepsilon_{fu} = \frac{f_{fu}}{E_f} \qquad (4-1)$$

where: ε_{fu} = ultimate axial strain of GFRP bar

f_{fu} = ultimate tensile stress of GFRP bar (MPa)

E_f = modulus of elasticity of GFRP bar (MPa)

The strain at each segment of concrete fiber was determined, and the corresponding stresses were calculated at each segment. The analysis was comprehensive for both axial and bending resistance, considering the GFRP bar's full contribution in compression. Furthermore, Young's modulus of reinforcement in tension was deemed to be equivalent to Young's modulus of reinforcement in compression.

4.1.1.2 Limitations

This section describes the limitations of the analytical model that was adopted in the development of this model. The axial and the bending resistance of the beam section were calculated through comprehensive analysis by considering the complete contribution of GFRP bars in compression. The shear deformation of the beam section was ignored based on the classic beam theory. This model's purpose was to develop a P-M interaction diagram, and there was no involvement of P-Delta analysis for generating this model. The maximum strain limit for the GFRP bars was calculated as 18000 μmm/mm based on the ultimate tensile strength and modulus of elasticity of the GFRP bars. The beam interaction diagram was developed for 3000 μmm/mm as per ACI 440.1R-15 (ACI 2015); however, the procedure used and the program can handle the strain limit of 3500 μmm/mm as per CSA806-12 (CSA 2012), CSA S6-14 (CSA 2014) and CSA A23.3-14 (CSA 2014). All ϕ factors for the compression and tension-controlled part of this beam section were considered to be unity.

4.1.1.3 Analysis Procedure

In this analytical model, the initial step was to determine the ultimate axial strain of the GFRP bar, which was followed by computation of actual strain in each layer of the reinforcement to determine the axial compressive force (Pu) and its corresponding bending moment for every neutral axis depth out of 20 neutral axis depth assumed for the beam section using the following equation:

$$\varepsilon_{fi} = \frac{\varepsilon_{cj}}{\varepsilon_{cu}}(c_q - d_i) \qquad (4-2)$$

where: ε_{fi} = axial strain of the GFRP bar (where i = 1, 2, 3)

ε_{cj} = axial strain of the concrete fiber (where j = 1, 2...20)

ε_{cu} = ultimate concrete strain taken as 0.003 mm/mm

f_{cj} = concrete stress corresponding to axial strain of concrete fiber (MPa)

c_q = neutral axis of the beam section (mm) (where q = 1, 2…20)

d_i = depth of each reinforcement layer (mm)

From the axial strain in the GFRP bar, it was compared with the ultimate axial strain to ensure the calculated strain was within the maximum limit. The following equation calculates the equivalent compressive and tensile stress:

$$f_{fi} = E_f \varepsilon_{fi} \qquad (4-3)$$

where: f_{fi} = axial stress of the GFRP bar (MPa)

The stress-strain curve method was used in the cross-sectional analysis of the GFRP beam. In 1973, Popovics (1973) proposed the convenient expression to determine the concrete in compression, which predicted accurately for the ascending portion of the stress-strain curve as follows:

$$f_{cj} = f'_c \frac{\varepsilon_{cj}}{\varepsilon'_c} \frac{n}{n-1+(\varepsilon_{cj}/\varepsilon'_c)^n} \qquad (4-4)$$

And the above expression was slightly modified and suggested by Thorenfeldt et al. (1987) to include the additional k factor to precisely predict the descending part of the stress-strain curve as follows:

$$f_{cj} = f'_c \frac{\varepsilon_{cj}}{\varepsilon'_c} \frac{n}{n-1+(\varepsilon_{cj}/\varepsilon'_c)^{nk}} \quad (4-5)$$

$$n = 0.8 + \frac{f'_c}{17} \text{ (MPa)} \quad (4-6)$$

$$k = 0.67 + \frac{f'_c}{62} \text{ (MPa)} \quad (4-7)$$

$$\varepsilon'_c = \frac{f'_c}{E_c} \frac{n}{n-1} \quad (4-8)$$

where: f'_c = unconfined concrete maximum compressive strength at 28 days (MPa)
n = curve fitting factor governing for ascending slope
k = curve fitting factor governing for descending slope
ε'_c = strain when f_c reaches the maximum compressive stress f'_c

The modulus of elasticity of concrete material was determined using the following equation per ACI 318-19 (ACI 2019):

$$E_c = 4700\sqrt{f'_c} \quad (4-9)$$

where: E_c = modulus of elasticity of concrete (MPa)

The axial compression or tension force in the GFRP bar was linear with the same modulus of elasticity. It was determined by multiplying the area of GFRP bars using the following equation:

$$F_{fi} = f_{fi} A_{fi} \quad (4-10)$$

where: F_{fi} = axial force of GFRP bars (kN)
A_{fi} = gross area of GFRP bars (mm^2)

The axial compressive force of each concrete fiber above the neutral axis was determined by multiplying with the width of the section and thickness of each segment. Then, the total compressive forces were calculated by summation of forces from each concrete fiber deducting the concrete area at the location of GFRP bars using the following equation:

$$C_c = \sum_{j=1}^{20} f_{cj}\, b\, \Delta y - \sum_{i=1}^{3} f_{ci}\, A_{fi} \qquad (4-11)$$

where: C_c = total concrete compressive force of beam section

b = width of beam cross-section (mm)

Δy = thickness of concrete segment (mm)

The total axial compressive force of the beam section was the addition of compressive force due to the concrete fibers, and the axial force due to the GFRP bars in the compression zone of the beam section was determined using the following equation:

$$P_u = C_c - \sum_{i=1}^{3} F_{fi} \qquad (4-12)$$

where: P_u = total compressive force of beam section (kN)

The bending moment due to axial compression or tension force in GRP bars was determined by multiplying the force in GFRP bars with lever arm from neutral axis using the following equation:

$$M_f = \sum_{i=1}^{3} F_{fi}\ (h/2 - d_i) \qquad (4-13)$$

where: M_f = bending moment due to axial force of GFRP bars (kNm)

The bending moment due to the axial compressive force in each concrete fiber above the neutral axis was determined by multiplying with the section's width, the thickness of each segment, and the lever arm from the center of the section (h/2). Then, the total bending

moment was calculated by summation of the moment due to the axial forces in each concrete fiber deducting the concrete area at the location of GFRP bars using the following equation:

$$M_c = \sum_{j=1}^{20} f_{cj}\, b\, \Delta y\, (h/2 - c) - \sum_{i=1}^{3} f_{ci}\, A_{fi}\, (h/2 - d_i) \qquad (4-14)$$

where: M_c = total bending moment due to axial force in concrete fiber (kNm)

h = height of beam cross-section (mm)

The total bending moment of the beam section was the addition of bending moment due to the forces in concrete fibers, and the moment due to the axial force in GFRP bars located within the compression zone of the beam section was determined using the following equation:

$$M_u = M_c - \mathrm{M}_f \qquad (4-15)$$

where: M_u = total bending moment of beam section (kNm)

The above process was repeated for different values of the neutral axis to determine the compressive force (P_u), which leads to the corresponding bending moment (M_u) of the beam required for the forming of the P-M interaction diagram based on the flowchart as shown in Fig 4-2.X. Henceforth, the model developed based on this procedure was chosen to perform the analytical study for the test specimens selected as part of this research and for the parametric study to investigate further the behavior of the beam section under different scenarios in the following section.

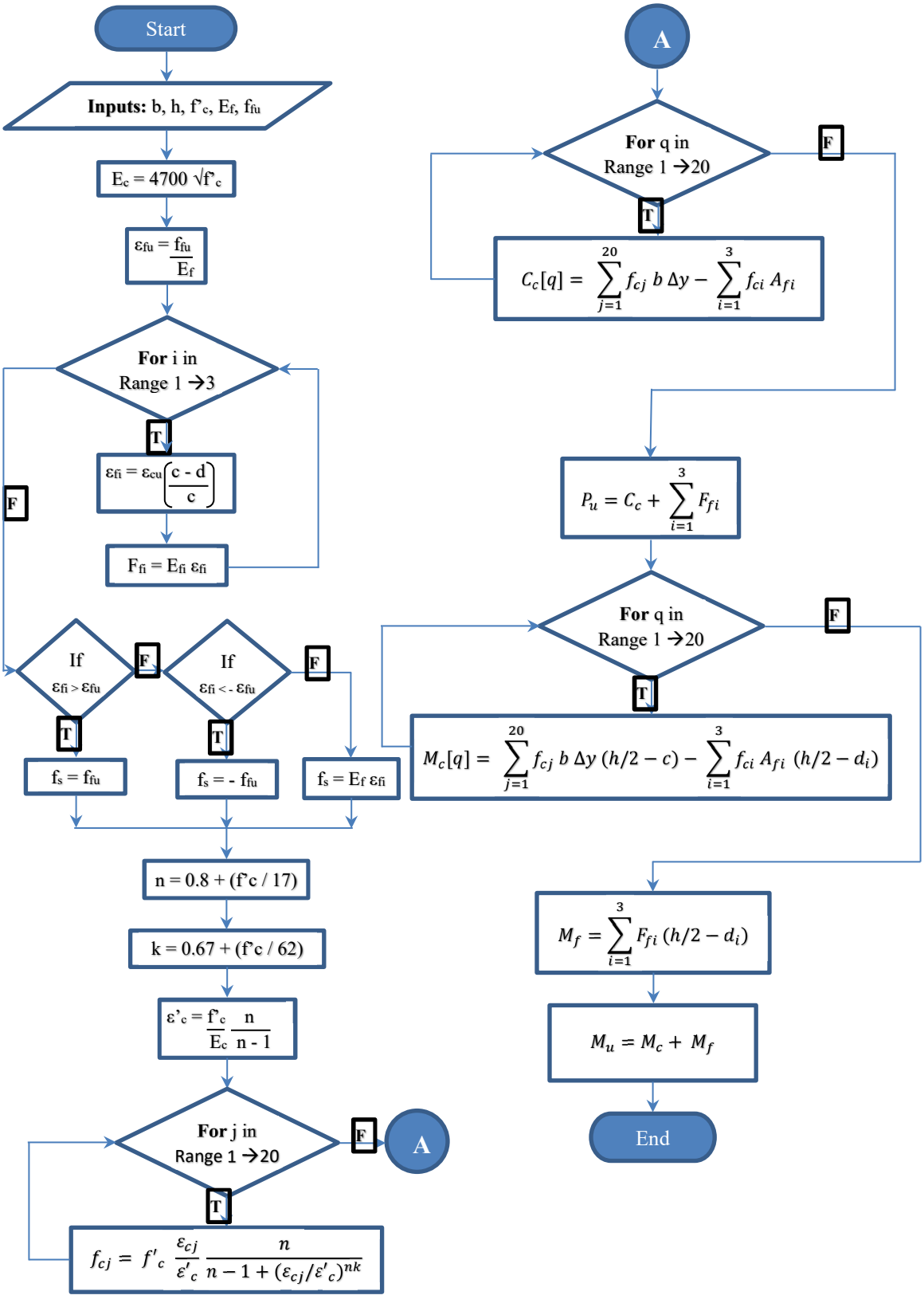

Fig 4-2 Analytical model flow chart

4.1.1.4 Verification Against the Current Experimental Study

Fig 4-4 compares the analytical model developed in this chapter with the GFRP reinforced concrete beam's experimental test data using the P-M interaction diagram. From the experimental test data, the compressive strain of 3000 mm/mm at which the concrete crushes were calculated from extrapolation of compressive strain at the top reinforcement. This applied load corresponding to the ultimate concrete strain was used to determine the bending resistance, which was plotted in the P-M interaction diagram and compared with the analytical model as shown in Fig 4-4.

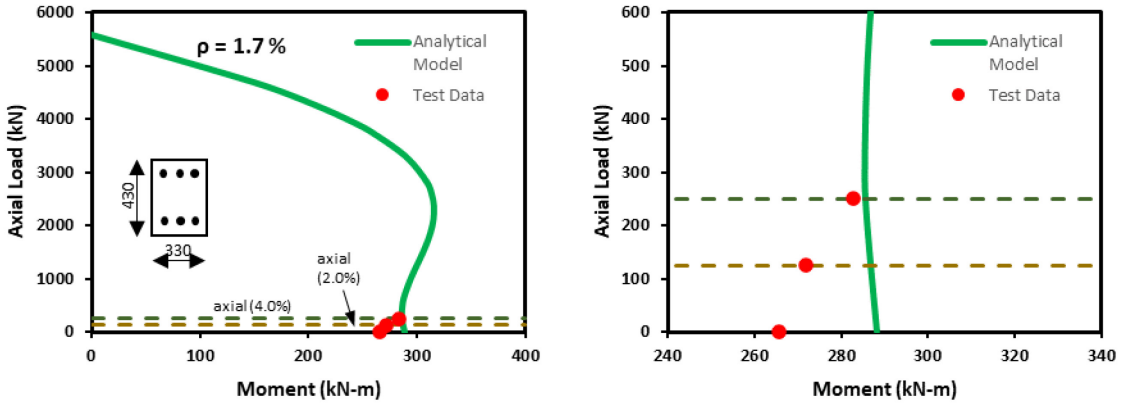

(a)

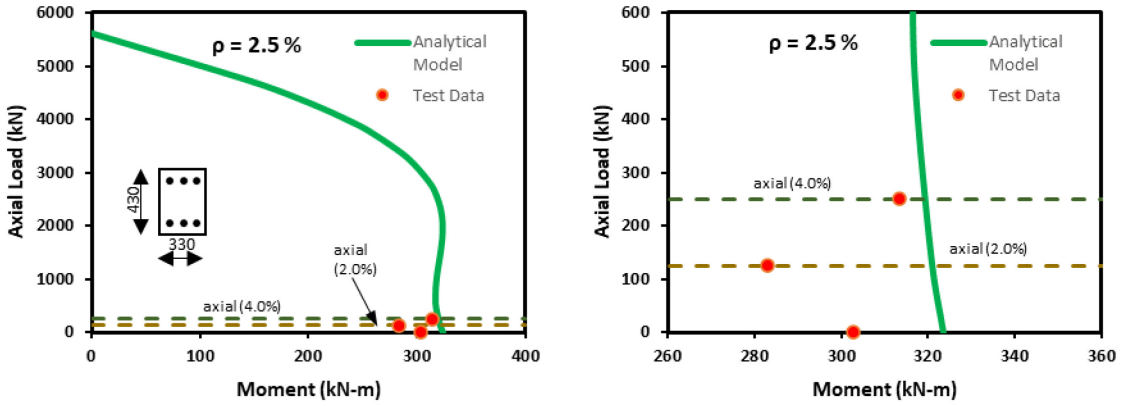

(b)

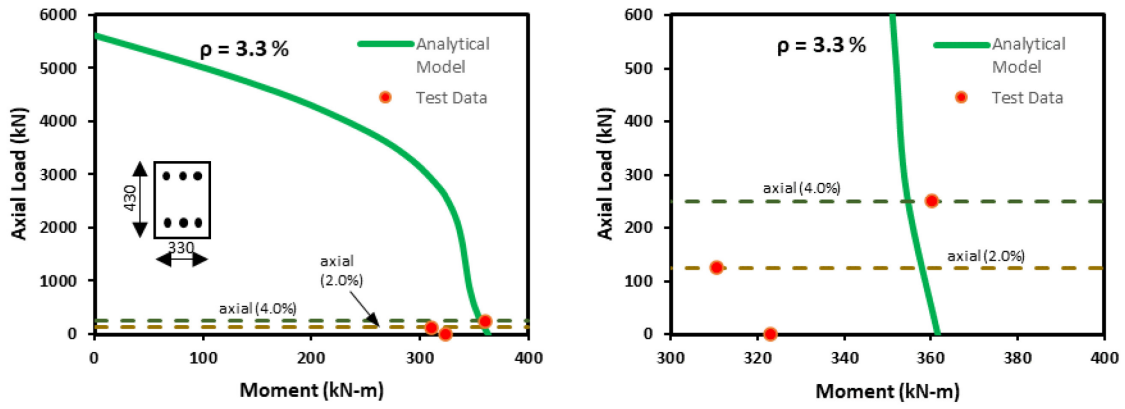

(c)

Fig 4-3 Axial load vs moment (a) ρ = 1.7% (b) ρ = 2.5% (c) ρ = 3.3% (analytical and experimental comparison)

The effect of axial load at a higher reinforcement ratio of 3.3% was closer to the pattern of the curve that was predicted through an analytical model, which implies that the bending resistance of 323 kNm at zero axial loads determined by experimental testing shows a reduction to 311 kNm on inducing low axial load of 2% to the beam. Similarly, for a 2.5% reinforcement ratio, the bending resistance of 303 kNm at zero axial loads decreased to 283 kNm with induced 2% axial load. However, for a lower reinforcement ratio of 1.7%, the curve's pattern was exactly the opposite, which shows bending resistance of 266 kNm at zero axial loads had increased to 271 kNm with the low axial load of 2%. From comparing different reinforcement ratios, it was more pronounced that applying low axial load at higher reinforcement reduces the bending resistance of the GFRP beam compared to the lower reinforcement ratio.

4.1.1.5 Verification Against Khorramian and Sadeghian (2017)

The analytical model was developed based on the paper's procedure by Khorramian and Sadeghian (2017) to study the experimental and analytical behavior of short concrete columns reinforced with GFRP bars under eccentric loading. In this paper, nine specimens with the size of 150 mm x 150 mm x 500 mm long were casted with different eccentricity to width ratio of 0.1, 0.2, and 0.3 for experimental investigation with geometric and

material nonlinearity, which was verified against the analytical model that was developed using the Popovics (1973) stress-strain curve method. This model has generated the stress-strain, load-strain, and axial-moment diagram. Furthermore, the paper recommended that GFRP bars take the higher strain and load-bearing effect of GFRP bars when used as longitudinal reinforcement cannot be ignored.

As Khorramian and Sadeghian (2017) proposed, an identical procedure was followed to create the analytical model to verify against the experimental test data and analytical model in this journal paper. In the development of this analytical mode1, first, it was developed based on Popovics (1973) stress-strain curve method. Later with Thorenfeldt et al. (1987) stress-strain equation was used with the same specimen size and concrete strength to calculate the axial and bending moment from which the P-M interaction diagram was plotted and compared with Khorramian and Sadeghian (2017) experimental test data and analytical model as presented in Fig 4-4. Similarly, the stress-strain curve was considered linear until the specimen failure, but the outcome of the stress-strain curve was more accurate in predicting the ascending branch of the stress-strain curve with the lack of accuracy in the descending branch of the curve.

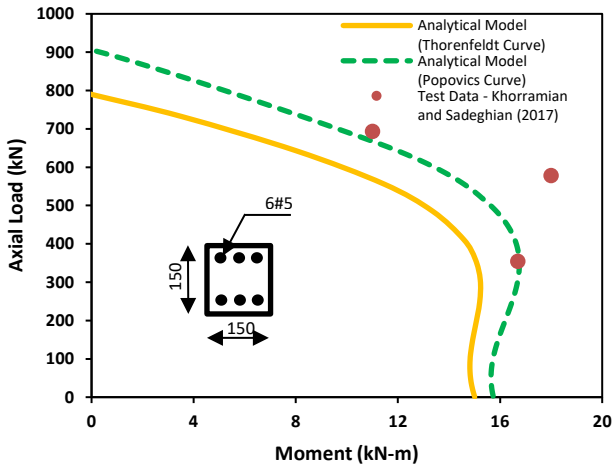

Fig 4-4 Verification of the analytical model against the analytical model and test data by Khorramian and Sadeghian (2017).

This analytical model Thorenfeldt et al. (1987) developed using the Mathcad showed reasonable agreement with the pattern of the P-M interaction diagram as shown in Fig 4-4. The analytical model's curve area was comparatively smaller due to the curve fitting factor used in the Thorenfeldt et al. (1987). Furthermore, the P-M interaction diagram confirms the philosophy that at the maximum ultimate moment of the GFRP beam, ignoring any accidental axial load causes the design failure and makes the beam unsafe. Still, through this method, the design failure was marginal. However, considering the pattern of the P-M interaction diagram, further verification was performed in the following section with Khorramian and Sadeghian's (2020) experimental test data based on the analytical model developed using Popovics (1973) and Thorenfeldt et al. (1987) stress-strain equation.

4.1.1.6 Verification Against Khorramian and Sadeghian (2020)

In this second verification, an analytical model developed was further verified against the experimental test data and analytical model of the research performed by Khorramian and Sadeghian (2020). They have investigated the short and slender concrete column of rectangular cross-section reinforced with GFRP bars under eccentric load. Ten concrete columns with a cross-sectional size of 205 mm x 306 mm having longitudinal reinforcement of #6 GFRP bars were tested with four different slenderness ratios of 16.6, 21.5, 39.7 and 59.5 considering two different reinforcement ratios of 2.78% and 4.80%. The slender columns were fabricated in the length of 1020 mm, 1320 mm, 2440 mm, and 3660 mm, having a rebar nominal cross-sectional area of 285 mm2 with a cover of 25.4 mm and concrete compressive strength of 48.4 MPa. The P-M interaction diagram was plotted with the analytical model as shown in Fig 4-5 (a) and (b) based on Popovics (1973) and Thorenfeldt et al. (1987) against the experimental test data. This comparative study has shown that the analytical model based on Thorenfeldt et al. (1987) was in reasonable agreement with the experimental test data, same as the previous verification of Khorramian and Sadeghian (2017).

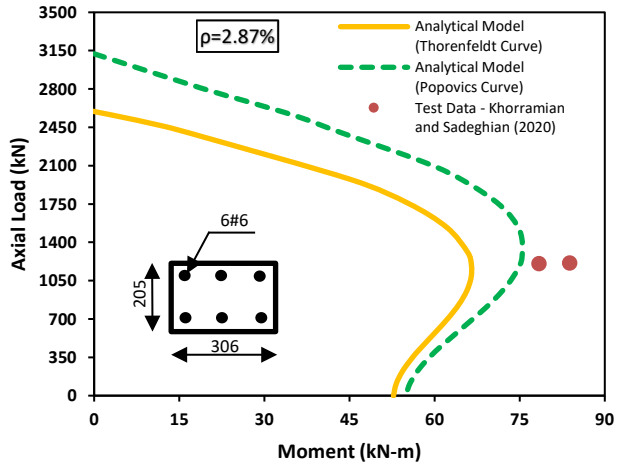

(a)

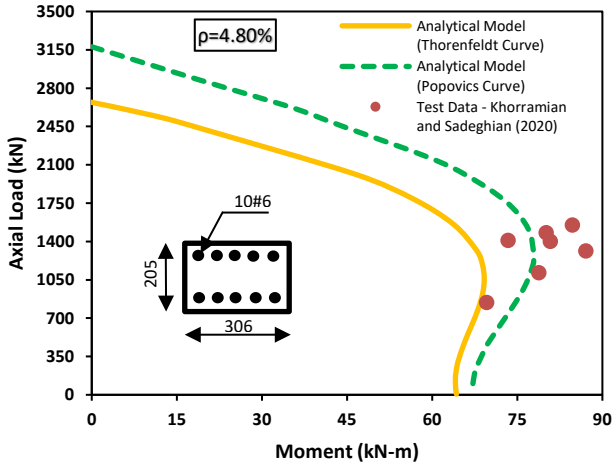

(b)

Fig 4-5 Verification of the analytical model against the analytical model and test data by Khorramian and Sadeghian (2020): (a) ρ = 2.87% (b) ρ = 4.80%

4.1.1.7 Verification Against Salah-Eldin et al. (2019)

In this section, the analytical model developed was further verified against the experimental test data and analytical model of the research performed by Salah-Eldin et al. (2019) to study the Axial-Flexural performance of High Strength Concrete bridge compression member reinforced with Basalt FRP bars. In this research, eight concrete columns of

400mm x 400mm x 2000mm were casted, and the analytical study was performed with varying concrete strength, reinforcement ratio, and load eccentricity. The research had precisely developed the analytical model by advancing one step forward in using the stress-strain curve method proposed by Thorenfeldt et al. (1987). The two main differences from the previous method of Popovics (1973), the first being the curve fitting factor proposed by Thorenfeldt et al. (1987), accurately predicted the stress-strain curve's descending branch. While the second difference was Popovics (1973) method was used for the beams and columns with normal strength concrete (NSC), but the Thorenfeldt et al. (1987) proposed for concrete beams with high strength concrete (HSC). The cross-sectional analysis was based on the design provision of ACI 440.1R-15 (ACI 2015) and CAN/CSA S806-12 (CSA 2012) and considered the maximum concrete strain of 3500 μmm/mm as per CAN/CSA S806-12. Two scenarios were considered in the stress-strain model, considering BFRP bars in compression and other scenarios ignoring the contribution of BFRP bars in compression. This research's main objective was to predict the axial and flexural strength, which was compared by plotting the axial-moment interaction diagram and load-eccentricity diagram, which was verified against the experimental investigation.

In this third verification, the analytical model was verified against Salah-Eldin et al. (2019) with the same beam section 400 mm x 400 mm x 2000 mm and the concrete strength 71.2 MPa, BFRP tensile strength 1646 MPa, elastic modulus 63.7 GPa, and all other parameters were used same as specified this journal paper. In this study, with the same concrete strength, reinforcement ratio, and consideration of BFRP bars, the input data was applied in the developed model. The P-M interaction diagram comparison was plotted as shown in Fig 4-6 against Salah-Eldin et al. (2019) experimental test data and analytical model based on Popovics (1973) and Thorenfeldt et al. (1987). The curve fitting factor proposed by Throrenfeldt et al. (1987) was most accurate in predicting the descending branch of the stress-strain curve, which created the correction in the trend of the P-M interaction diagram specifically at the lower portion of the curve, which was tension controlled by BFRP bars whereas the impact in the upper portion of the curve controlled by concrete compression was negligible. The axial load and bending moment curve shows that the analytical model's result was almost the same as the Salah-Eldin et al. (2019) analytical model. Based on this

verification, it can be concluded that the analytical model was in good agreement with this journal paper which considers the stress-strain equation proposed by Thorenfeldt et al. (1987), and from the parametric studies presented in this paper its evident that the failure at the maximum ultimate bending moment of the beam section caused by applying 2.5% little axial load which exactly supports the basic philosophy of this thesis.

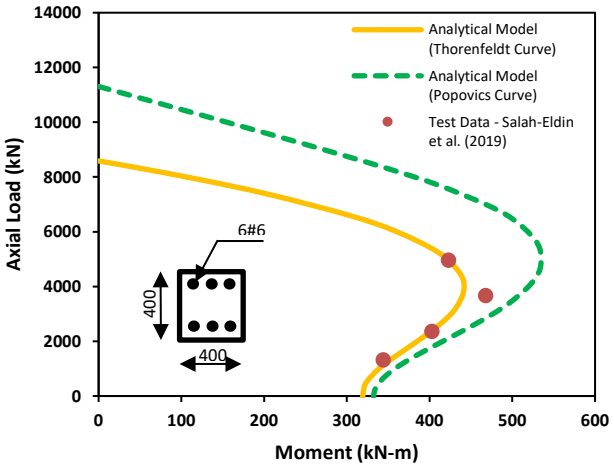

Fig 4-6 Beam interaction diagram - axial load vs bending moment Salah-Eldin et al. (2019)

4.1.1.8 Verification Against Salah-Eldin et al. (2020)

In this section, the fourth verification was considered to verify the developed analytical model against the experimental and analytical study performed by Salah-Eldin et al. (2020) to evaluate the effect of reinforcement ratio on strength and stiffness in high strength concrete column (G1) with longitudinal reinforcement of six #6 GFRP bars with a diameter of 20 mm and a column (G2) with longitudinal reinforcement of eight #8 GFRP bars with a diameter of 25 mm was tested. The #6 GFRP bar's nominal cross-sectional area was 285 mm2, and the #8 GFRP bar was 510 mm2, both column specimens with a concrete cover of 40 mm. The GFRP ties of size #3 (diameter of 10 mm) with a midspan spacing of 150 mm and end spacing of 100 mm was used in the transverse direction for both the column type. In this paper, there was twelve high strength GFRP reinforced concrete columns

(HSC) with a square cross-sectional size of 400 mm x 400 mm and the height of 2000 mm, average concrete compressive strength of 71.2 MPa (28 days strength), elastic modulus 62.7 GPa, ultimate GFRP tensile strength 1036 MPa with varying GFRP reinforcement ratio of 0.5%, 1.0% and 2.5% under different load eccentricities was tested.

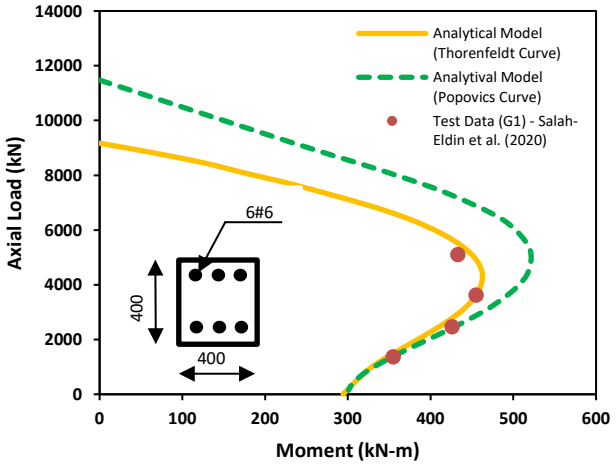

(a)

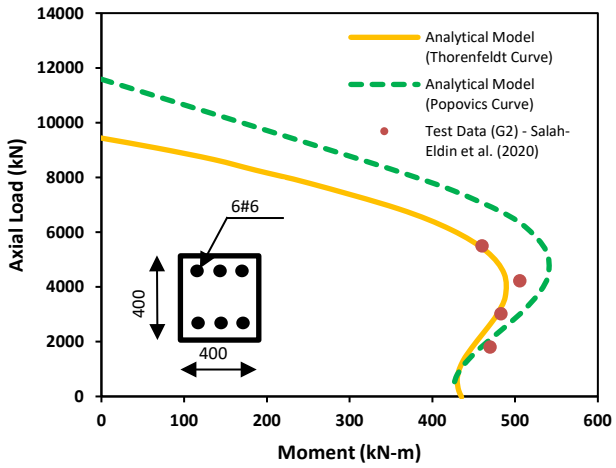

(b)

Fig 4-7 Beam interaction diagram - axial load vs bending moment Salah-Eldin et al. (2020): (a) tested column G1 (b) tested column G2

The analytical model approach was based on the stress-strain relationship equation proposed by Thorenfeldt et al. (1987), the maximum concrete strain of 3000 μmm/mm as

per ACI 2015 and the contribution of GFRP bars in compression was considered to develop and compare the moment-curvature and axial load-deflection diagram with experimental results. In the tested columns, G1 and G2 with the four load eccentricities of 80 mm, 120 mm, 160 mm, and 240 mm (e/h = 0.2, 0.3, 0.4, and 0.6) were verified against the developed analytical model by plotting the P-M interaction diagram comparison which was successfully predicted as shown in Fig 4-7 (a) and (b). Overall, the plotted comparison chart shows that the analytical model was in good agreement with the experimental test performed by Salah-Eldin et al. (2020). The verified analytical model was used to conduct the parametric study considering the various parameters such as reinforcement ratio, concrete strength, cross-sectional shape, and FRP modulus.

4.1.2 Shear Failure

The current design guidelines ACI 440.1R-15 (ACI 2015), CAN/CSA S806-12 (CSA 2012), and CAN/CSA S6-14 (CSA 2014) proposed different design approaches to predict the shear strength due to concrete and web reinforcement of GFRP beams. To account for the shear resistance due to concrete and webs reinforcement, ACI 440.1R-15 (ACI 2015) recommends the following equation for flexural members.$V_c = \frac{2}{5}\sqrt{f'_c}b_w(k_n d)$ (2 – 1)

$$k_n = \sqrt{2\rho_f n_f + (\rho_f n_f)^2} - \rho_f n_f \qquad (2-2)$$

$$V_f = \frac{A_{fv} f_{fv} d}{s} \qquad (2-3)$$

$$f_{fv} = 0.004E_f \leq f_{fb} \qquad (2-4)$$

$$f_{fb} = \left[0.05\frac{r_b}{d_b} + 0.3\right] f_{fvu} \leq f_{fvu} \qquad (2-5)$$

where: V_c = nominal shear strength of concrete (kN)

b_w = width of web (mm)

k_n = ratio of depth of neutral axis to reinforcement depth

d = distance from extreme concrete fiber to centroid of tension reinforcement (mm)

ρ_f = fiber-reinforced polymer reinforcement ratio

n_f = ratio of modulus of elasticity of FRP bars to modulus of elasticity of concrete

V_f = shear resistance by FRP stirrups (kN)

A_{fv} = amount of FRP shear reinforcement within spacing s (mm^2)

f_{fv} = tensile strength of FRP for shear design (MPa)

s = stirrup spacing (mm)

f_{fb} = strength of bent portion of FRP bar (MPa)

r_b = internal radius of bent (mm)

d_b = diameter of reinforcing bar (mm)

Based on Canadian code CAN/CSA S806-12 (CSA 2012), the design provisions to calculate the shear capacity of concrete and web reinforcement of GFRP beams are as follows.

$$V_c = 0.05\,\lambda\,\varphi_c k_m k_r \sqrt[3]{f'_c}\, b\, d_v \qquad (2-6)$$

$$k_m = \sqrt{v_f d / M_f} \leq 1.0 \qquad (2-7)$$

$$k_r = 1 + \sqrt[3]{E_{fv}\rho_{fw}} \qquad (2-8)$$

$$d_v = \max\,[0.9d, 0.72h] \qquad (2-9)$$

$$V_{fv} = \frac{0.4\,\varphi_f A_{fv} f_{fv} d_v}{s} \cot \alpha_s \qquad (2-10)$$

$$\alpha_s = 30° + 7000\,\varepsilon_x \qquad (2-11)$$

$$\varepsilon_x = \frac{\frac{M_f}{d_v} + V_f}{2\,E_{fv}\,A_{fv}} \qquad (2-12)$$

where: λ = factor for concrete density

φ_c = resistance factor for concrete

k = beam width

d_v = effective shear depth

E_{fv} = modulus of elasticity of FRP shear reinforcement

ρ_{fv} = FRP web-reinforcement ratio

ϕ_f = resistance factor for FRP

α_s = inclination angle of the main diagonal compressive strut

ε_x = average longitudinal strain at mid-span of the section

To calculate the shear resistance due to concrete and web reinforcement based on Canadian code CAN/CSA S6-14 (CSA 2014) are as follows.

$$V_c = 2.5\beta\varphi_c f_{cr} b d_v \quad (2-13)$$

$$\beta = \frac{0.4}{1+1500\varepsilon_x} \times \frac{1300}{1000+s_{ze}} \quad (2-14)$$

$$f_{cr} = 0.4\sqrt{f'_c} \quad (2-15)$$

$$d_v = \max[0.9d, 0.72h] \quad (2-16)$$

$$V_{fv} = \frac{\varphi_f A_{fv} f_{fv} d_v}{s} \cot\alpha_s \quad (2-17)$$

$$\alpha_s = (29 + 7000\,\varepsilon_x)(0.88 + \frac{s_{ze}}{2500}) \quad (2-18)$$

$$\varepsilon_x = \frac{\frac{M_f}{d_v}+V_f}{2\,E_f\,A_f} \leq 0.003 \quad (2-19)$$

$$f_{fv} = \min\{0.004E_f, \left[0.05\frac{r_b}{d_{bfv}} + 0.3\right] f_{fvu} \quad (2-20)$$

where: f_{cr} = cracking strength of concrete (MPa)

β = factor for the shear resistance of cracked concrete

The comparison between the experimental shear strength and theoretical shear strength prediction was based on the different design codes and guidelines such as ACI 440.1R-15 (ACI 2015), CSA S806-12 (CSA 2012), and CSA S6-14 (CSA 2014) were presented in

Table 4-1. The reduction factor ϕ was considered as unity in the theoretical calculation for all three design codes. From the comparison, it was clear that Canadian codes (CSA 2012) and (CSA 2014) underestimated the shear strength due to the stringent procedure used to calculate the contribution of GFRP stirrups in shear strength. However, the shear strength predicted based on the American code (ACI 2015) was conservative and on the higher side compared to experimental shear strength results.

Table 4-1 Theoretical Shear strength prediction for test specimen

Sl. No.	Specimen ID	Experimental	ACI 440.1R-15		CSA S806-12		CSA S6-14	
		V_{exp} (kN)	V_{pred} (kN)	V_{exp}/V_{pred}	V_{pred} (kN)	V_{exp}/V_{pred}	V_{pred} (kN)	V_{exp}/V_{pred}
1	B-R1.7-P0	265	125	2.12	84	3.15	83	3.19
2	B-R1.7-P2	270	125	2.16	84	3.21	83	3.25
3	B-R1.7-P4	339	125	2.71	84	4.04	83	4.08
4	B-R2.5-P0	339	137	2.47	84	4.04	83	4.08
5	B-R2.5-P2	333	137	2.43	84	3.96	83	4.01
6	B-R2.5-P4	346	137	2.53	84	4.12	83	4.17
7	B-R3.3-P0	360	147	2.45	84	4.29	83	4.34
8	B-R3.3-P2	398	147	2.71	84	4.73	83	4.80
9	B-R3.3-P4	347	147	2.36	84	4.13	83	4.18

4.2 Load-FRP Strain Behavior

Fig 3-8 shows the strain response of the GFRP bars with varying load from the experimental that was compared against the strain extracted from the analytical model. In terms of strain comparison, the experimental strain data were in good agreement with the analytical model. The experimental data shows that the initial strain data was lesser, which confirms that GFRP bars in top and bottom had experienced the lower strain value because of uncracked concrete, and the strain recorded was claiming rapidly after the concrete cracks.

(a)

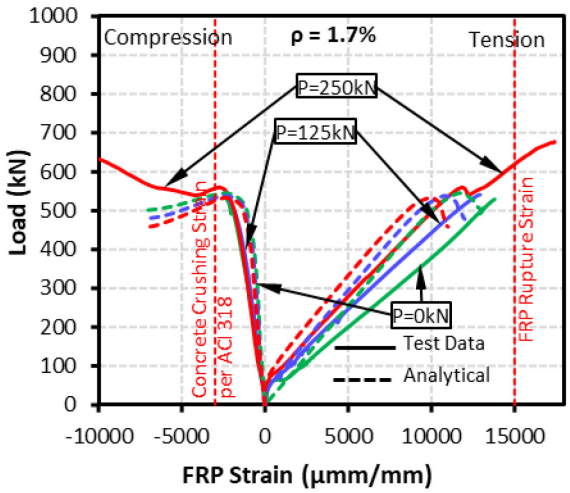

(b)

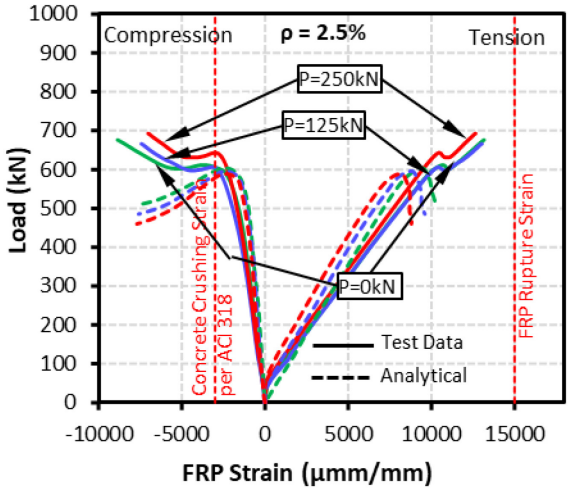

(c)

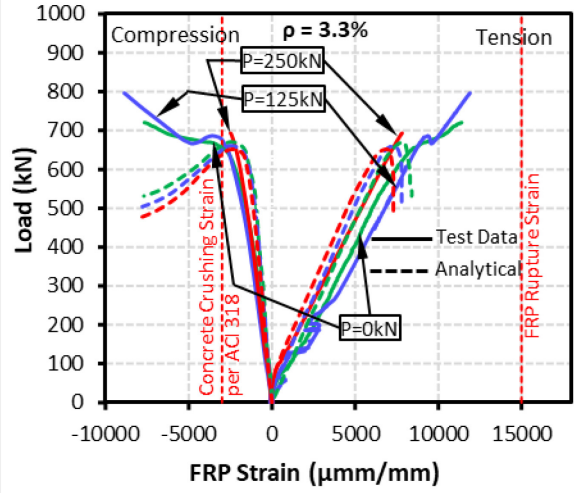

Fig 4-8 Load vs FRP strain at mid-span (a) ρ = 1.7% (b) ρ = 2.5% (c) ρ = 3.3%

However, the analytical model was based on cracked concrete, which shows the initial stage's linear curve. In the experimental model's case, after the crushing of concrete at the strain of 3000 μmm/mm, strain value had claimed predominantly up to the second peak load until the specimen's failure by shear and flexure. Furthermore, it was observed from the test data of all test specimens that the average compressive and tensile strain GFRP bars experienced after the crushing of concrete were 4000 μmm/mm and 10,000 μmm/mm, respectively. This compressive and tensile strain sustained by the GFRP bars above the crushing of concrete had contributed to the test specimens' increased moment capacity.

4.3 Neutral Axis-Moment Behavior

The neutral axis behavior at the midspan of the test specimens was plotted from the beam section's mid-height against the corresponding moment to compare the experimental and analytical models for the reinforcement ratio of 1.7%, 2.5%, and 3.3%. The curve's initial stage difference was due to the uncracked concrete in the experimental testing against the analytical model designed as a cracked section. The neutral axis showed non-linear behavior with the load's variation both experimentally and theoretically extracted from the model. However, the experimental testing's neutral axis-moment curve had demonstrated good agreement with the analytical model for all the reinforcement ratios compared in Fig. 4-9. The experimental model shows that there was a shift in the neutral axis towards the mid-height of the specimen after the crushing of concrete, which further increased the strain in the GFRP bars, resulting in the additional moment capacity for all test specimens until the failure.

(a)

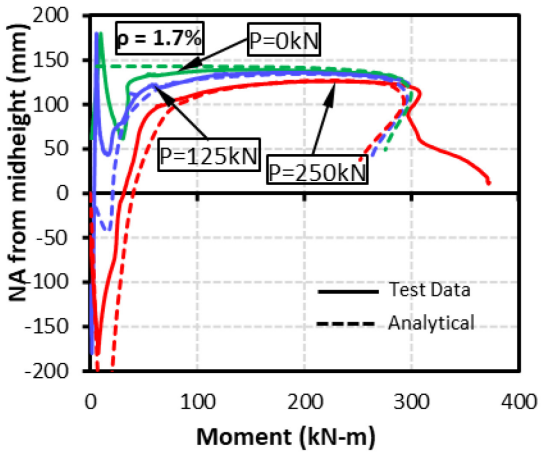

(b)

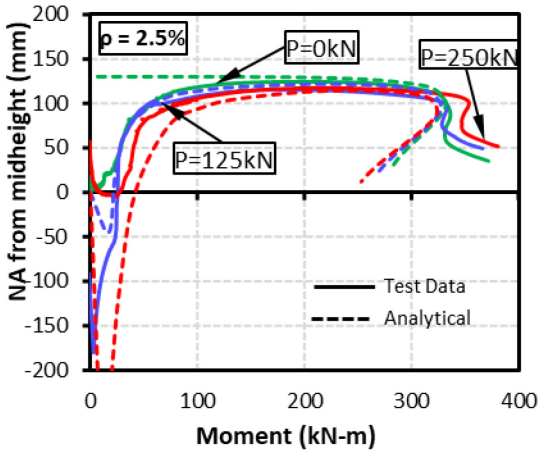

(c)

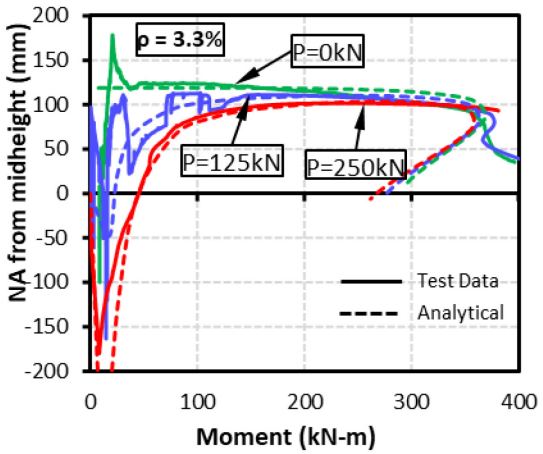

Fig 4-9 Neutral axis vs moment at mid-span (a) ρ = 1.7% (b) ρ = 2.5% (c) ρ = 3.3%

4.4 Moment-Curvature Model

When the GFRP beam was subjected to transverse load and low axial load that creates the bending and axial compression, there was a significant shift in the neutral axis due to the variation in the applied load, further related to the direct impact in the curvature of the beam. The analytical model was developed to investigate the moment-curvature behavior of the GFRP beam using the same stress-strain curve method proposed by Thorenfeldt et al. (1987) to develop the P-M interaction diagram. The model was developed using Matlab software using Romberg's numerical integration method and Secant root finding method. Curvature was determined by assuming the concrete's extreme compressive strain, thereby finding the beam's neutral axis with the equilibrium condition of ∑Fx = 0. With the neutral axis, axial capacity and moment resistance of the beam section was determined, further used to find the curvature using equation (4 – 16).

$$\psi_m = \frac{\varepsilon_{cu}}{c} \qquad (4 - 16)$$

where: ψ_m = curvature at middle of the beam (rad/km)

ε_{cu} = ultimate compressive strain of concrete (μmm/mm)

c = neutral axis depth of beam cross-section (mm)

The procedure mentioned above was repeated for different concrete compressive strain values to arrive at the moment-curvature diagram's various data points. The analytical model was plotted against the moment-curvature diagram determined from the experimental test data, as shown in Fig 4-10. The lower longitudinal ratio of 1.7% had shown higher curvature and lower moment resistance against the higher reinforcement ratio of 2.5% and 3.3%, which had experienced lower curvature and higher moment resistance. The comparison between the analytical model of moment-curvature was in good agreement with experimental test data calculated from the average values of top and bottom strain gauges of the test specimen.

(a)

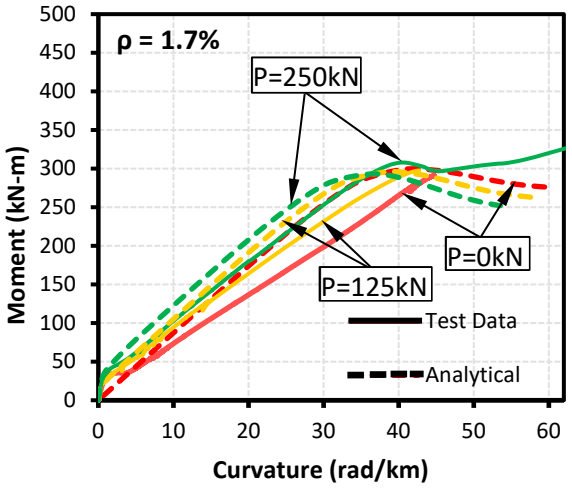

(b)

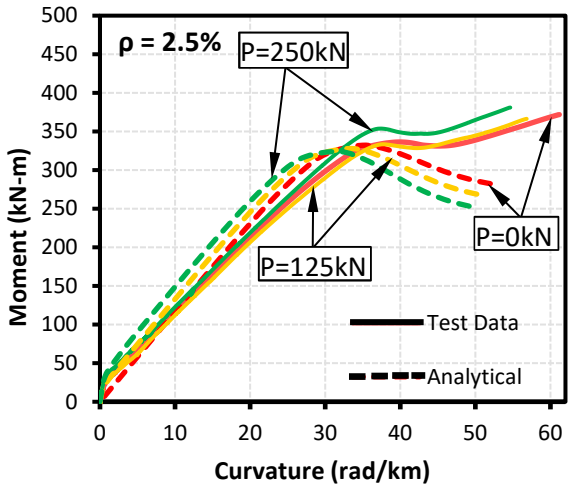

(c)

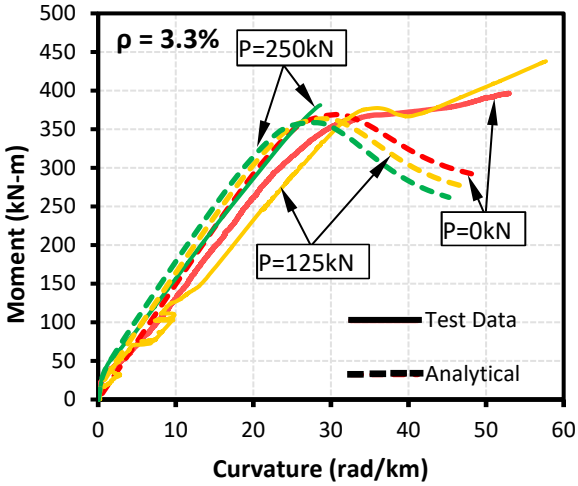

Fig 4-10 Moment vs curvature at mid-span (a) ρ = 1.7% (b) ρ = 2.5% (c) ρ = 3.3%

4.5 Load-Deflection Model

For the GFRP reinforced beam subjected to four-point bending, the vertical deflection varies from zero to the maximum deflection at the mid-span of the beam, calculated based on the moment-curvature relationship model developed in the previous section. The curvature at the mid-span of the beam was calculated for the varying transverse load and its corresponding moment. From the curvature, the vertical deflection was computed using the moment-area method at the mid-span by integrating the area under the curvature for any particular load and strain of the extreme concrete fiber. The shear deformation of the GFRP beam was considered defined in the following equations (4-17) and (4-18).

$$\gamma = \frac{k_v V}{G_c A_e} \qquad (4-17)$$

$$A_e = A_g \left[\frac{M_{cr}}{M_{max}}\right]^3 + A_{cr}\left[1 - \left[\frac{M_{cr}}{M_{max}}\right]^3\right] \qquad (4-18)$$

where: γ = shear strain (μmm/mm)

k_v = shear coefficient depending on cross-section (1.2 for rectangular section)

V = external shear force (kN)

G_c = shear modulus of elasticity of concrete (GPa)

A_e = effective section area (mm^2)

A_g = area of the gross section (mm^2)

A_{cr} = area of the cracked section (mm^2)

M_{cr} = flexural cracking moment (kNm)

M_{max} = maximum moment (kNm)

(a)

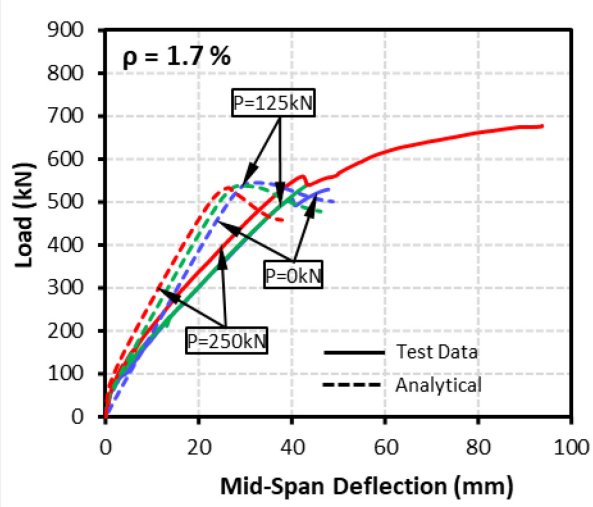

(b)

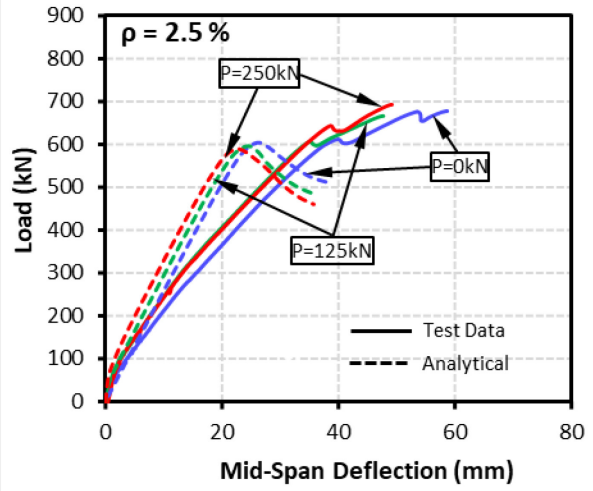

(c)

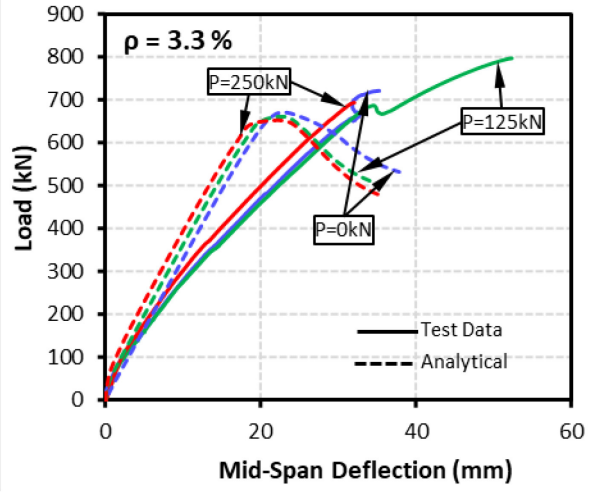

Fig 4-11 Load vs vertical deflection at mid-span (a) ρ = 1.7%
(b) ρ = 2.5% (c) ρ = 3.3%

The procedure was repeated for different curvature values, calculated for various data points in the curve depending on the values of extreme concrete strain and its corresponding neutral axis in determining the bending moment for varying load. The analytical model developed based on Thorenfeldt et al. (1987) stress-strain curve method predicted the deflection up to the first peak load behavior of concrete crushing. The transverse load vs vertical deflection on the GFRP beam at the mid-span was compared experimentally and theoretically are presented in Fig 4-11. The experimental curve had shown that the vertical deflection of the specimen experienced more deflection at the first peak load where the crushing of concrete occurred, but the deflection had extended further until the failure of the specimen by flexure or shear. All the test specimens had shown a noticeable load drop when the first failure of concrete crushing happened at the first peak load. It was observed from the comparison that the GFRP beam subjected to pure bending without axial load had experienced more deflection than the beams with axial load of 2% and 4%. The GFRP beam with a lower reinforcement ratio of 1.7% deflected comparatively more than the beam with a higher reinforcement ratio of 2.5% and 3.3%. The test specimen B-R1.7-P4, which had continued deflecting after the first peak load of concrete crushing, had experienced the higher deflection of all the specimen and the difference of 2.5 times higher than its counterpart B-R1.7-P0 and B-R1.7-P2 under zero and low axial load that failed in shear. The analytical model that was plotted until the first peak load of concrete crushing had shown good agreement with the experimental model.

4.6 Parametric Study (P-M Interaction Model)

This section presents the parametric study conducted to assess the effect of five significant parameters using cross-sectional analysis in the GFRP reinforced beam section's behavior. The parameters used in the investigation were reinforcement ratio, concrete strength, cross-sectional shape, GFRP modulus, and axial load. In this study, the test specimen with the rectangular beam size of 300 mm x 400mm and another specimen with the square beam size of 300mm x 300mm. The reinforcement ratio used was in the range of 2% to 4% and with the concrete strength (f'_c) variation of 30, 40, 50, 60, and 70 MPa. The reason to select another specimen with a square cross-section was to study the effect of cross-sectional shape variation. The axial load applied longitudinally to the beam was 2.5% and 5% to the

beam's axial capacity. This study's result was compared with the P-M interaction diagram and presented in the figures shown in the below section. This detailed investigation paved the way for the number of predominant conclusions in the concrete beam's behavior reinforced with GFRP bars.

4.6.1 Effect of Reinforcement Ratio

In this section, the investigation was carried out with different reinforcement ratios for the test specimen to study the effect of reinforcement ratio in the flexural behavior of GFRP reinforced rectangular beam. The reinforcement ratio was the ratio of the area of longitudinal reinforcement (A_f) provided in the tensile zone to the gross cross-sectional area of the beam (A_g). For the comparison, four different reinforcement ratios (ρ) at the bottom side of the beam of 2.0%, 3.0%, 4.0%, and 5.0% were examined with concrete compressive strength (f'_c) of 60 MPa in this parametric study. The reinforcement ratio specified were used in the analytical model, and its results were plotted as a comparison in the below Fig 4-12.

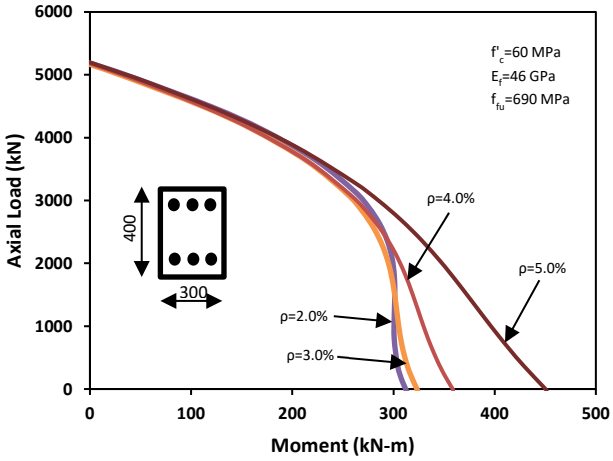

Fig 4-12 Effect of reinforcement ratio comparison

The number of compression reinforcement considered was similar in all cases; hence, the interaction diagram in Fig 4-12 summarizes the results by showing that the curve remains identical in the top upper portion, a compression-controlled zone. The trend varies mainly at the bottom part of the tension-controlled zone with the enlargement due to the difference in tension reinforcement distribution (e.g., ρ = 5.0%). The gradual increase of reinforcement ratio 2.0% to 5% shows that the beam's bending moment resistance increased from 315 to 450 kNm. The bending moment resistance has increased gradually in the percentage of 2.9%, 10.8%, and 25.7%, based on the reinforcement ratio increase from 2.0% to 5.0%, respectively. Moreover, at a lower reinforcement ratio, the lower end of the curve shows a steep decline relatively gradual decline of the curve at a higher reinforcement ratio. From the percentage increase of bending moment resistance, the curve at lower and higher reinforcement ratio gives a clear indication that the beam's failure can occur due to applying minimum accidental axial load, which was more pronounced at a higher reinforcement ratio. In comparison, the effect was negligible at a lower reinforcement ratio.

4.6.2 Effect of Concrete Strength

The variation in concrete strength (f'_c) and its impact were analytically investigated to study the effect of stiffness and strength, directly resulting in the rectangular beam section. To examine the effect of concrete strength and its flexural behavior, there were four different concrete strength of 30 MPa, 40 MPa, 50 MPa, and 60 MPa with the steady increment of 10 MPa were selected and applied in the developed analytical model to perform the section analysis with four different reinforcement ratio in the range of 2.0%, 3.0%, 4.0% and 5.0% with the increment of 1.0% were used to calculate the axial (P_u) and moment resistance (M_u) to form the comparative axial load – bending moment interaction diagram developed based on section analysis, using Eqs. (4 - 12) and (4 - 15) as shown in the Fig 4-13 (a), (b), (c) and (d). The increase of reinforcement ratio (ρ) comparison shown in the previous section was more pronounced towards the increase of bending resistance in the tension controlled section, whereas the increase of concrete strength has resulted in the larger interaction curve of not only increasing the bending resistance but also change the axial capacity of uncracked concrete. Henceforth, this observation's physical meaning

shows that the gradual increase of concrete strength (f'_c) from 30 MPa to 60 MPa has increased the axial and bending capacity of the considered rectangular beam section in the range of 15% to 20%.

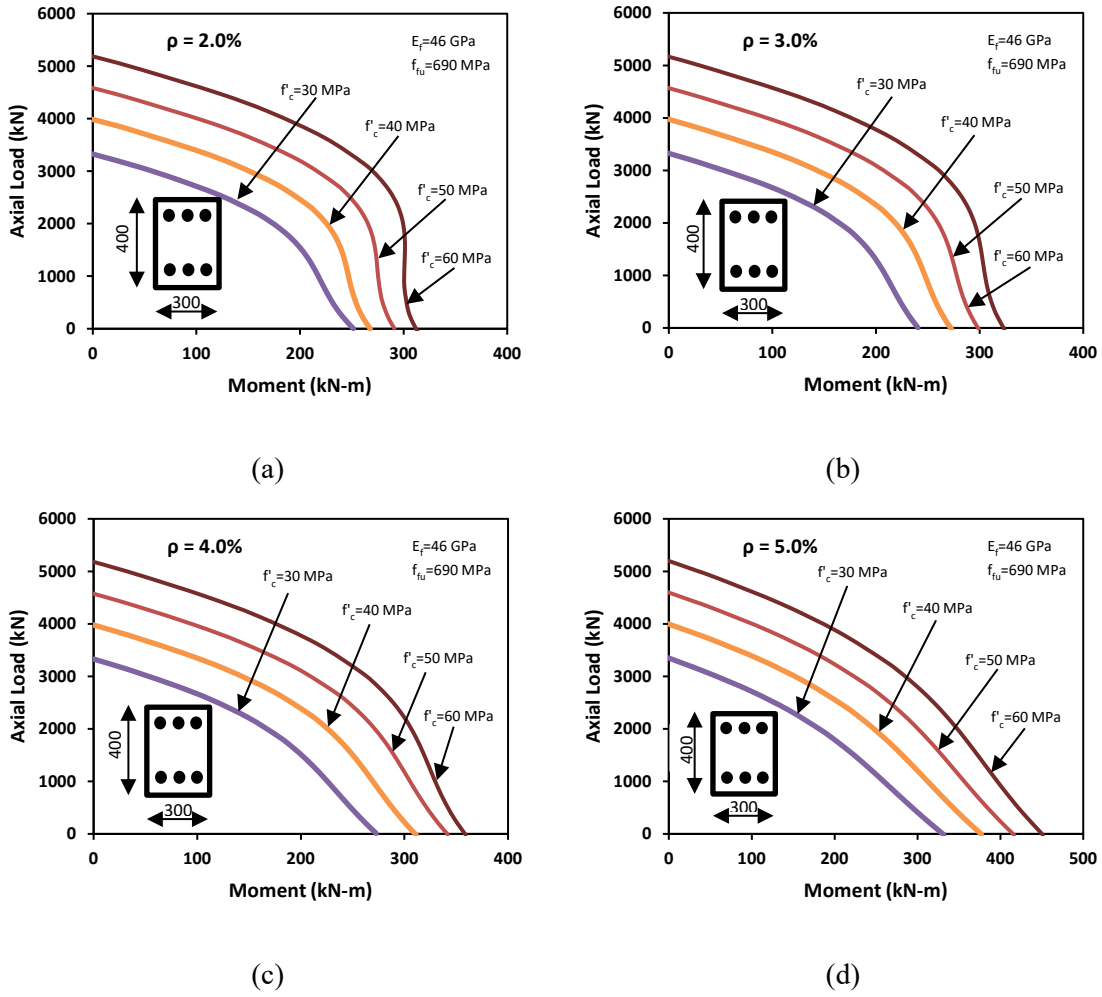

Fig 4-13 Effect of concrete strength: (a) reinforcement ratio (ρ = 2.0%) (b) reinforcement ratio (ρ = 3.0%) (c) reinforcement ratio (ρ = 4.0%) (d) reinforcement ratio (ρ = 5.0%)

From the Fig 4-13 (a) and (b), for the reinforcement ratio (ρ) of 2.0% and 3.0%, the axial load - bending moment interaction curves for each concrete compressive strength (f'_c) have enlarged in size gradually without affecting the trend of the curve except for the concrete strength of 30 MPa which was flatter hence the strength impact due to the application of accidental axial load was consequently lesser as the descent was steeper at the lower portion

of the curve. However, Fig 4-13 (c) and (d) shows that, for the reinforcement ratio (ρ) of 3.0% and 4.0%, the trend of the axial load (P_u) – bending moment (M_u) interaction diagram was flatter with the increase of concrete strength and the slope descent of the curve was gradual which was evident that minimum axial load applied in this condition causes the reasonable strength impact that cannot be ignored. Thus, it can be concluded that the effect of the concrete strength parameter plays an insignificant role in comparison with the effect of reinforcement ratio, which plays a crucial role in reducing the beam strength due to any accidental axial load.

4.6.3 Effect of Cross-sectional Shape

To find out the effect due to the cross-sectional shape of the beam, the comparative study was performed with the test specimen having a rectangular size of 300 mm (b) x 400 mm (h) and the square beam specimen of 345 mm (b) x 345 mm (h) was selected as shown in the below Fig 4-14. The square beam's unusual dimension was selected to match the rectangular beam's cross-sectional area (Ag).

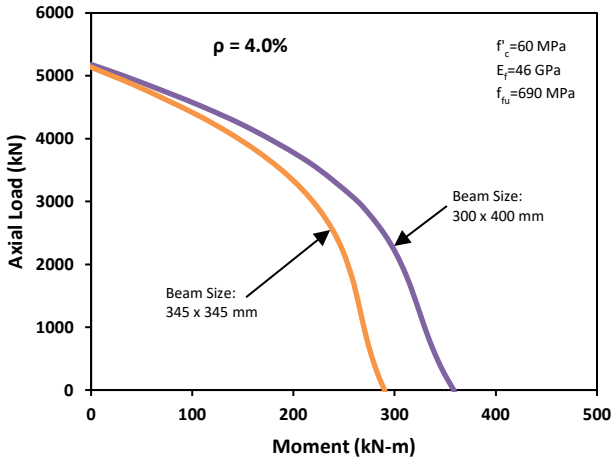

Fig 4-14 Cross-sectional shape comparison – Axial load vs bending moment interaction diagram

The other parameters selected was reinforcement ratio (ρ = 4.0%), elastic modulus (Ef = 46 GPa), tensile strength (f_{fu} = 690 MPa) and concrete compressive strength (f'_c) as 60 MPa with the maximum of concrete strength used in the parametric study. The analytical

model was used for this parametric study with the different beam shapes. The model's result was plotted as axial load (Pu) – bending moment (Mu) interaction curves to predict and compare the impact in flexural strength behavior of GFRP concrete beams. Fig 4-14 shows that the bending resistance for the rectangular beam was 359 kNm which was comparatively higher as against the square beam bending resistance of 290 kNm. The moment difference has shown that for the same cross-sectional area, the beam's shape plays a key feature in achieving the ultimate strength of the section. The axial load–bending moment diagram presented in Fig 4-10 summarizes the results that the square beam has lost 24% of its bending resistance against the rectangular beam. However, the lower portion of the curve was flatter in the rectangular beam compared to the square beam's steep curve. Applying minimum accidental axial load to rectangular beam causes a substantial decrease in the moment capacity compared to the marginal decline in the square beam case.

4.6.4 Effect of FRP Modulus

In this section, the effect of FRP modulus (E_f) for the GFRP beam was studied with a range of 35 to 50 GPa applied to the analytical model with a gradual increase of 5 GPa.

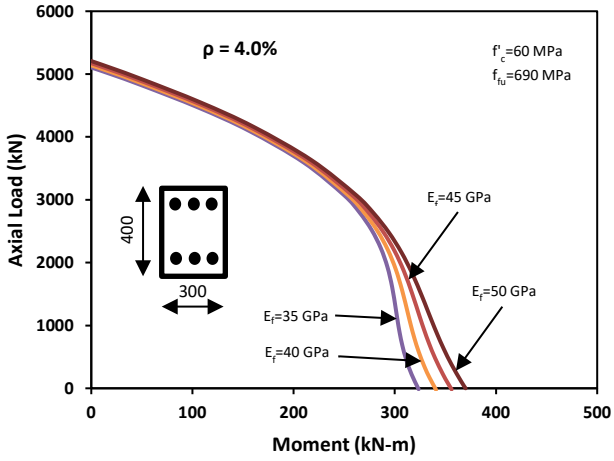

Fig 4-15 Effect of GFRP modulus comparison

The interaction diagram for axial load vs bending moment was plotted for four different GFRP modulus values for the concrete strength of 60 MPa and reinforcement ratio of 4.0%, while tensile strength (f_{fu}) remains as constant for all four values of GFRP modulus. Below,

Fig 4-15 shows the comparison of the interaction diagram for various GFRP values. From the lower to higher GFRP modulus value, the interaction diagram enhances marginally at the lower portion of the curve, whereas there was no noticeable difference at the upper portion of the curve. As the E_f value increased from 35 to 50 GPa, the bending resistance of the GFRP beam has shown a 3% to 5% increase with negligible changes in the axial resistance.

4.6.5 Effect of Axial Load

In this section, the impact of the minor axial load applied to the GFRP beam subjected to full flexural bending was studied considering the two-minimum range of 5% and 10% of the concrete strength capacity of the beam section. The variation in the reinforcement ratio was considered to study four different interaction diagrams with constant value of concrete strength (f'_c = 60 MPa), GFRP modulus (E_f = 46 GPa) and tensile strength (f_{fu} = 690 MPa). Fig 4-16 shows the axial load vs bending moment interaction diagram for all four reinforcement ratio conditions.

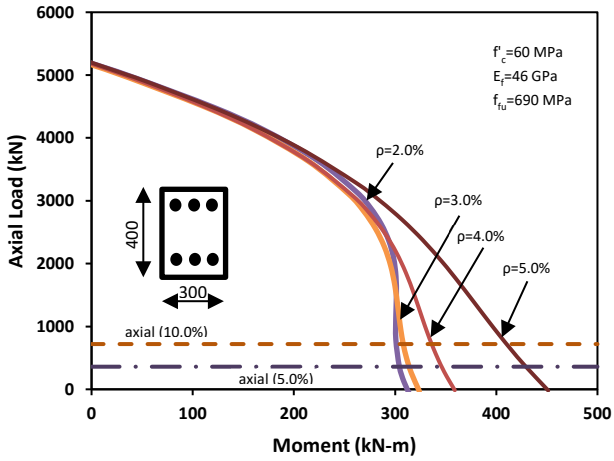

Fig 4-16 Performance of GFRP beam against minimum axial load

The two horizontal dotted lines shown at the curve's bottom are the axial load of 5% and 10%. Besides, the figure summarizes the ultimate bending resistance of the GFRP beam ranging from 316 kNm to 451 kNm with the increase of reinforcement ratio from 2% to 5%. Furthermore, at the minimum axial load (P_u) of 5% and 10%, the bending resistance

(M_u) of the beam has decreased, being marginal at a lower reinforcement ratio to critical at a higher reinforcement ratio. For example, at the reinforcement ratio of 5.0%, the beam ultimate bending resistance was 451 kNm when the axial load of 5% (360 kN) was applied to the beam, the bending resistance has shown the decrease to 430 kNm resulting in the loss of capacity by 4.7%. And a further increase of axial load (P_u) to 10% (720 kN), the bending resistance (M_u) decreased to 410 kNm shows that the overall capacity reduced by 9.1%.

4.7 Parametric Study (Moment-Curvature Model)

The moment-curvature analytical model developed was used for this parametric study to investigate the effect of increasing compression top reinforcement in the beam cross-section of test specimen B-R3.3-P0. The axial load of zero, 120 kN, and 240 kN were used for comparison of beams with different reinforcement ratios for compression reinforcement, while the reinforcement ratio of tensile bottom reinforcement was maintained as 3.3% throughout the parametric study. The normal concrete strength considered was 44.2 MPa from the concrete cylinder testing; the elastic modulus of GFRP bars in compression and tension was taken as average from the material testing performed, which was 48 GPa and 45 GPa, respectively. The compression reinforcement of four varying parameters such as 2, 4, 6, and 8 bars was considered, and their reinforcement ratio was calculated and presented in Table 4-2.

Fig 4-17 demonstrated the change in behavior of the FRP strain in compression and tension with the increase of compression reinforcement from 2 bars to 8 bars. The model was developed and extended with the limitation of 10000 μmm/mm as concrete strain on the extreme concrete fiber for which the corresponding strain in the compression and tensile reinforcement was determined. The FRP strain had shown no significant difference until the crushing of concrete at 3000 μmm/mm for all three comparisons of the axial load. However, the impact of the compression reinforcement ratio was significant, and it was observed that the curve's trend had shown a drastic difference.

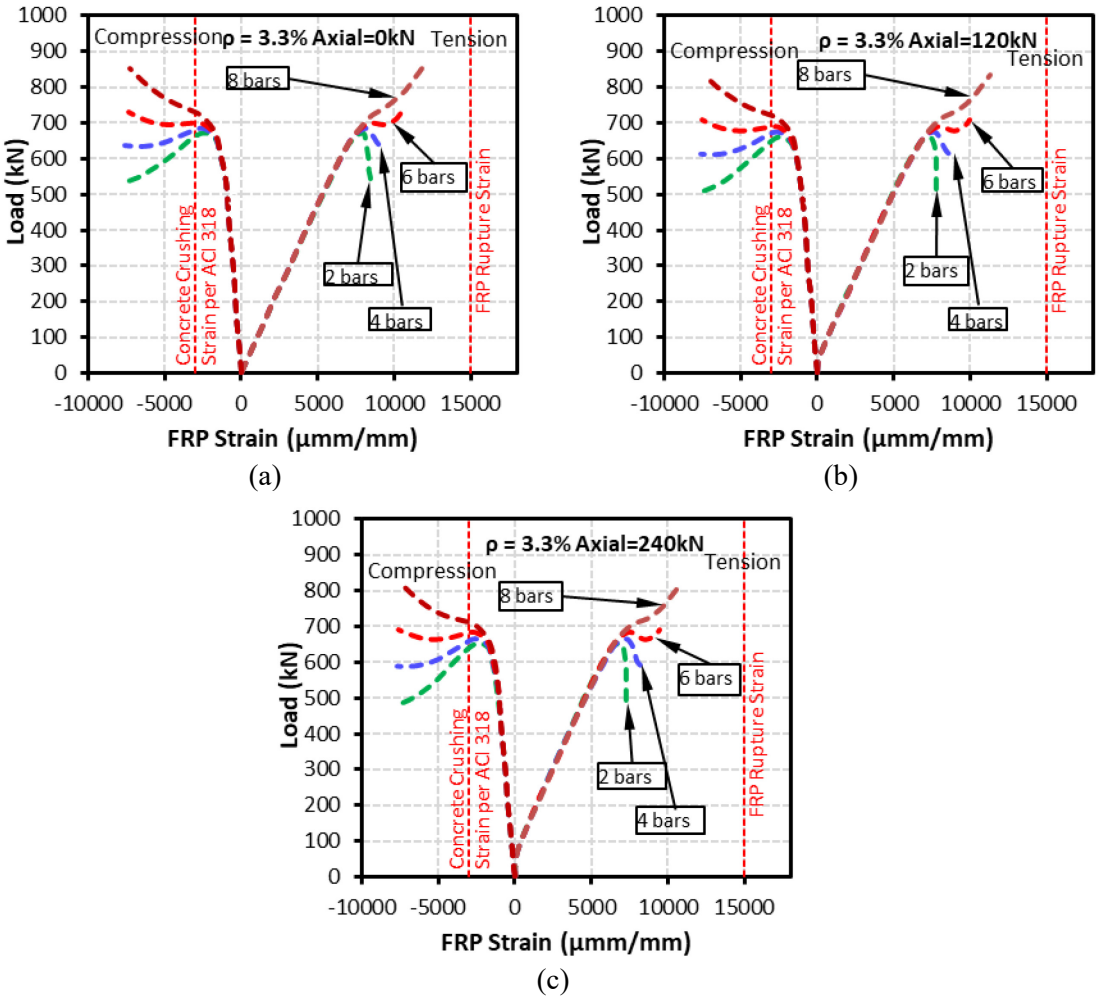

Fig 4-17 Load vs FRP strain (a) P = 0 kN (b) P = 120 kN (c) P = 240 kN

The curve started descending after reaching the ultimate concrete strain for the compression reinforcement ratio of 0.9 and 1.7%. However, the curve had shown an upward trend for the compression reinforcement ratio of 2.6 and 3.7%. The corresponding tensile strain curve descending for the lower compression reinforcement ratio showed the ascending trend for the higher compression reinforcement ratio.

Fig 4-17 demonstrated the change in strain behavior of the extreme concrete fiber in the compression side of the beam cross-section at mid-span with the increase of compression reinforcement from 2 bars to 8 bars.

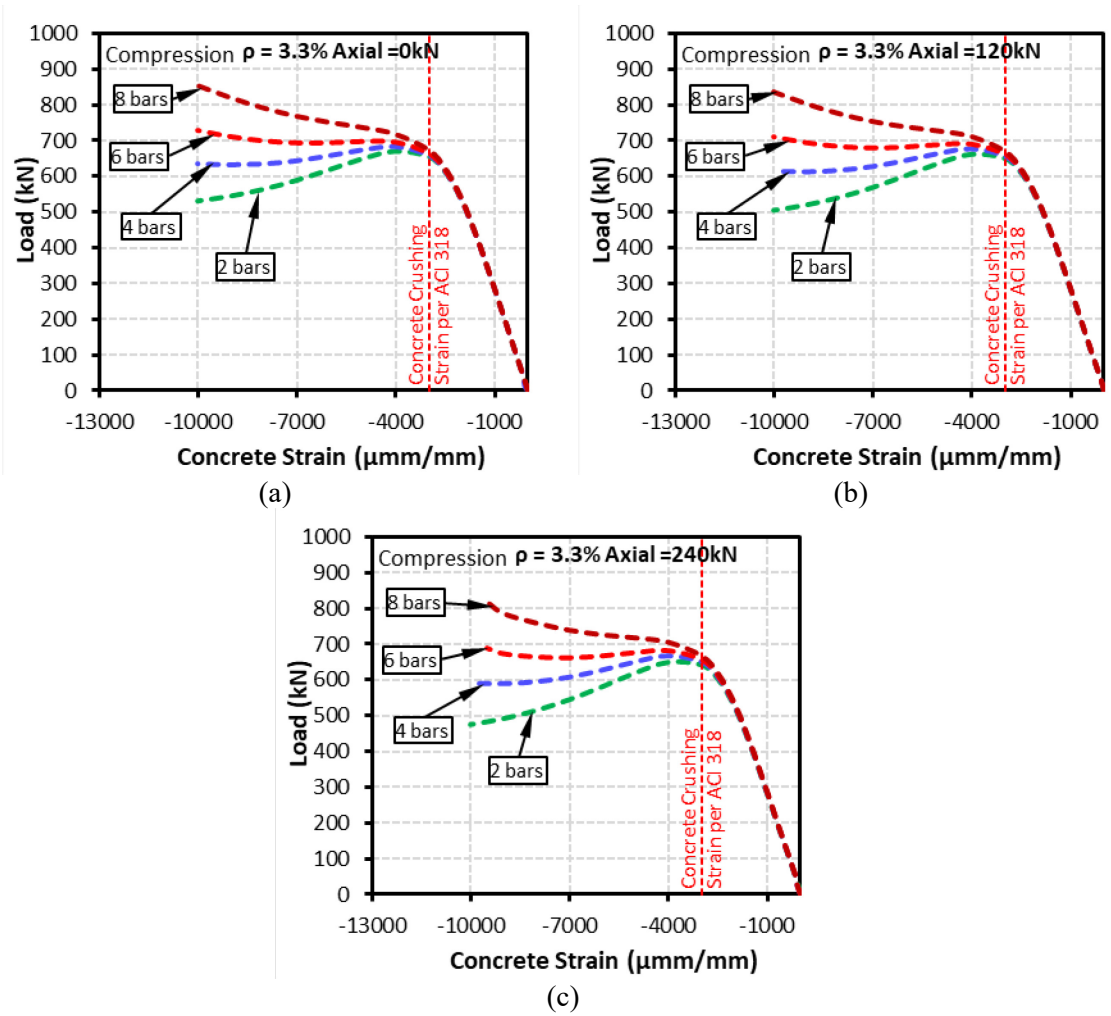

Fig 4-18 Load vs concrete strain (a) P = 0 kN (b) P = 120 kN (c) P = 240 kN

The concrete strain of the extreme concrete fiber was the assumed values in the range 0 to 1000 µmm/mm for which the neutral axis was determined. Further neutral axis was used to determine the FRP strain at the top compression and tensile reinforcement as the strain profile was linear. The concrete strain had shown the linear behavior until crushing at 3000 µmm/mm, whereas the curve had demonstrated the ascending and descending trend based on the compression reinforcement ratio.

The neutral axis-moment behavior was plotted in Fig 4-19 for various reinforcement ratios on the compression side. The neutral axis at lower load and strain started closer to the mid-section for pure bending, whereas for a beam with axial load of 120 kN and 240 kN, the neutral axis started below the mid-section.

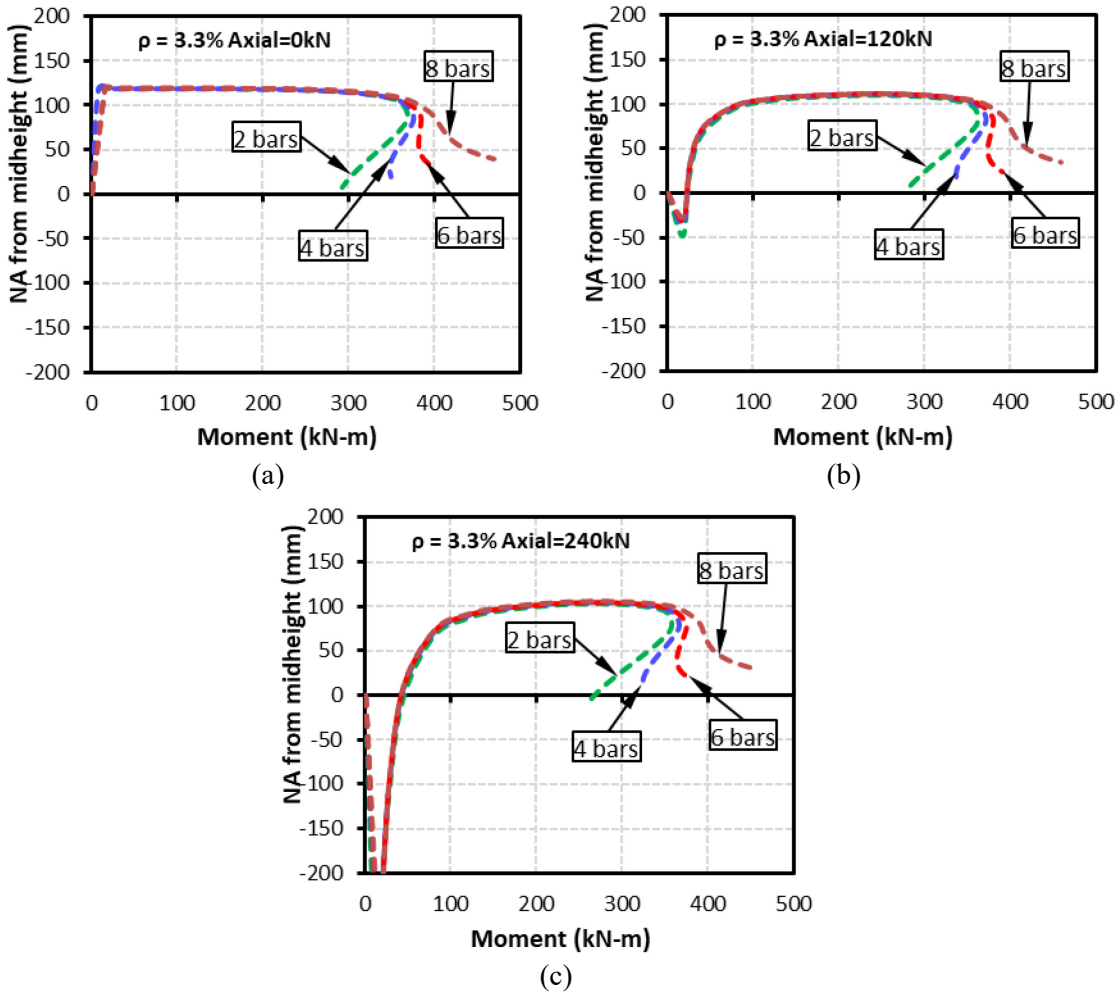

Fig 4-19 Neutral vs moment (a) P = 0 kN (b) P = 120 kN (c) P = 240 kN

The neutral various had maintained consistent value just below the compression reinforcement and above the mid-section of the beam until concrete crushing. However, after concrete crushing, the neutral axis lowered towards the mid-section with a decrease in bending resistance for lower compression reinforcement ratio and increased bending resistance for higher compression reinforcement ratio.

Fig 4-20 shows the moment-curvature behavior of the beam with an increase in compression reinforcement ratio for 2, 4, 6, and 8 bars. No visible difference was observed in the model, with moment and curvature remains similar until the concrete crushing at 3000 μmm/mm at first peak load.

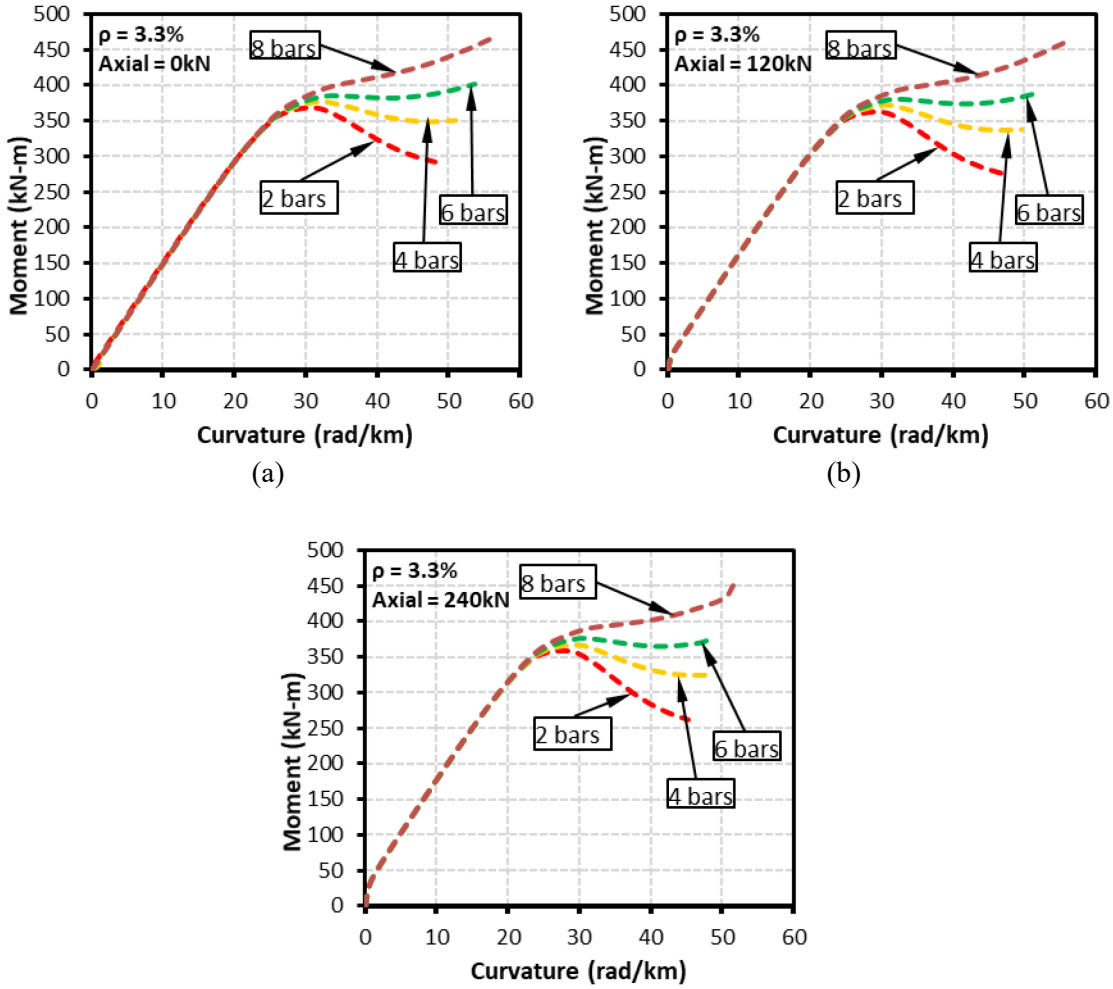

Fig 4-20 Moment vs curvature (a) P = 0 kN (b) P = 120 kN (c) P = 240 kN

The model started behaving differently just before reaching the ultimate concrete strain in the bending resistance, where it began taking deviation. However, the moment capacity of the beam section decreases at a lower reinforcement ratio, and an increase in moment capacity occurred at a higher reinforcement ratio. From this comparison, it should be noted that the contribution of GFRP bars in compression was more predominant after concrete crushing, and this was more pronounced in the case of higher reinforcement ration which had a major contribution towards the second-moment capacity and sustained the higher peak load until the failure of GFRP bars by rupture.

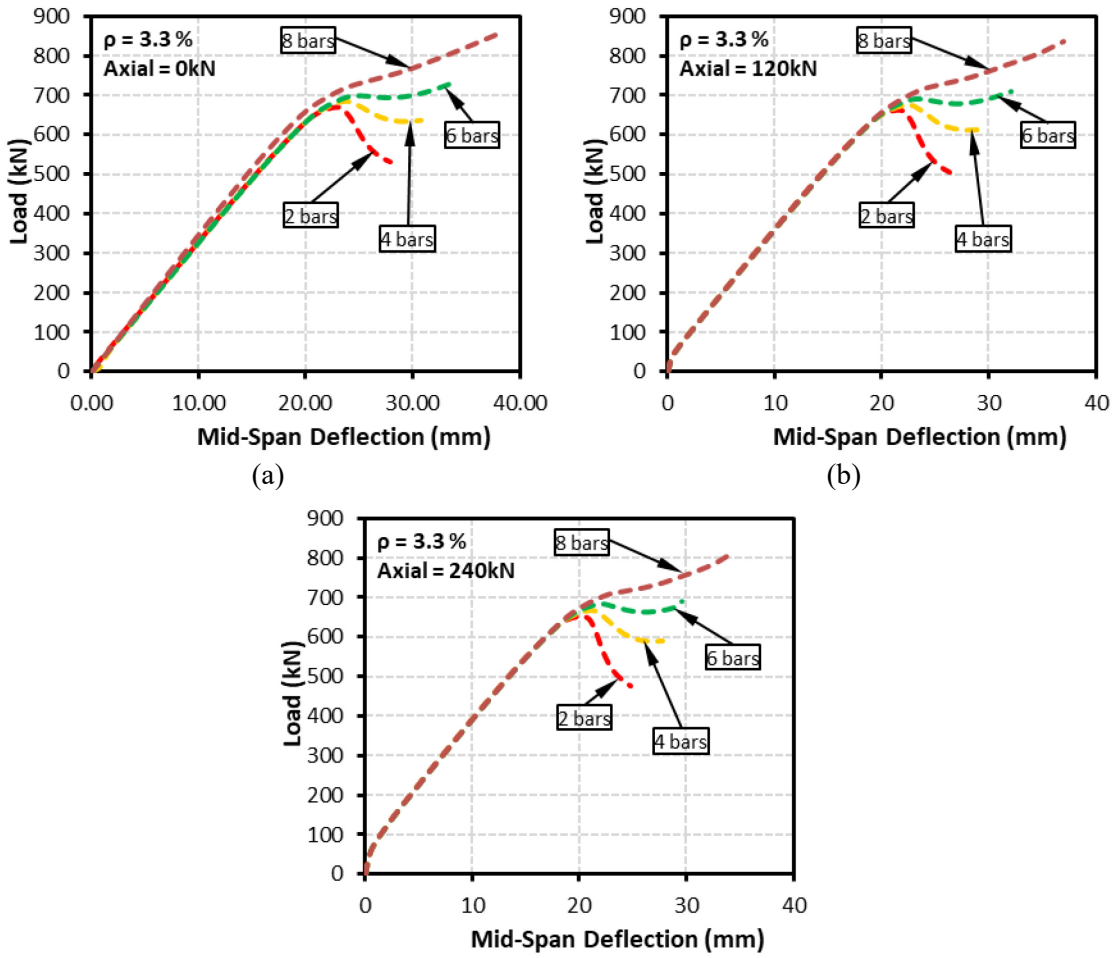

Fig 4-21 Load vs defelction (a) P = 0 kN (b) P = 120 kN (c) P = 240 kN

The load-deflection behavior of the model was compared for different compression reinforcement ratios and under varying low axial in Fig 4-21. The model demonstrated a curve with linear behavior with varying compression reinforcement ratio until concrete crushing except for beam with 8 bars as compression reinforcement where a minor difference in the curve was noticed. The load sustained by the beam started descending after the first peak load for a lower compression reinforcement ratio of 0.9 % and 1.7 %. However, the ascending behavior was shown by the beam section with a higher reinforcement ratio of 2.6 % and 3.4 %. The contribution of GFRP reinforcement after concrete crushing was visible and more pronounced in the case of the beam section with a higher compression reinforcement ratio where it sustained higher peak loads and deflection.

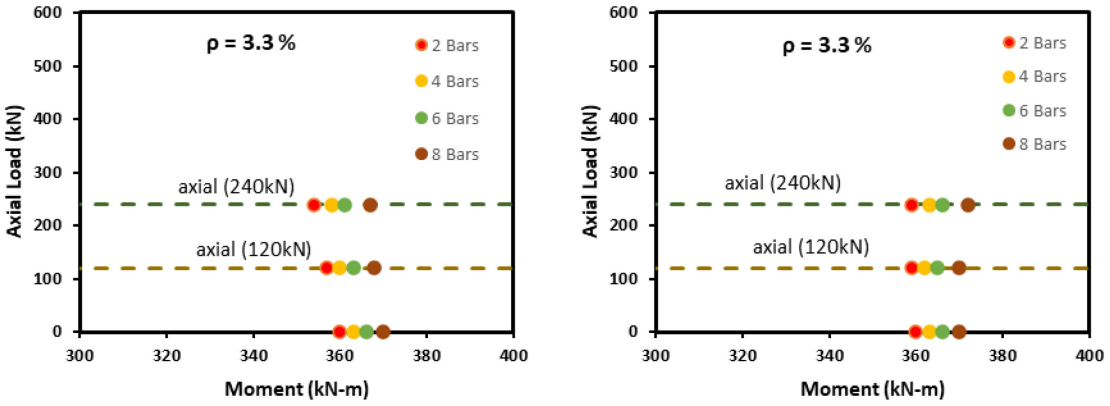

(a) (b)

Fig 4-22 Axial load vs moment (a) with P-Delta (b) without P-Delta

Fig 4-22 shows the axial load–moment behavior of the beam section with varying reinforcement ratios in the compression zone. The first load sustained by the beam section in each case at concrete crushing was noted and the corresponding flexural moment capacity was determined using the shear span. The bending moment resistance of each beam section for pure bending, an axial load of 120 kN and 240 kN, were plotted as three data points for each compression reinforcement ratio. Two diagram was plotted and compared considering the effect due to P-delta. Fig 4-22 (a) without the P-delta effect had shown the decrease in the ultimate moment capacity for all compression reinforcement ratios with an induced axial load of 120 kN and 240. However, considering the P-delta effect had shown that ulmate moment capacity remains constant with induced axial load at lower reinforcement ratio of 0.9 % and 1.7 %, but the moment capacity had shown an increase with the axial load for higher reinforcement ratio of 2.6 % and 3.4 %.

Table 4-2 Parametric study results summary

Sl. No.	Case ID	Rho = Af/bd	No. of Compression bars	Rho' = Af'/bd	Axial Load (kN)	Load at concrete strain of 3000 μmm/mm	Moment W/o P-Delta (kNm)	Moment With P-Delta (kNm)
1	B-R3.3-P0-C2	4.3	2	0.9	0	655	360	360
2	B-R3.3-P0-C4	5.2	4	1.7	0	660	363	363
3	B-R3.3-P0-C6	6.0	6	2.6	0	665	366	366
4	B-R3.3-P0-C8	6.9	8	3.4	0	673	370	370
5	B-R3.3-P2-C2	4.3	2	0.9	120	649	357	359
6	B-R3.3-P2-C4	5.2	4	1.7	120	655	360	362
7	B-R3.3-P2-C6	6.0	6	2.6	120	661	363	365
8	B-R3.3-P2-C8	6.9	8	3.4	120	670	368	370
9	B-R3.3-P4-C2	4.3	2	0.9	240	643	354	359
10	B-R3.3-P4-C4	5.2	4	1.7	240	651	358	363
11	B-R3.3-P4-C6	6.0	6	2.6	240	657	361	366
12	B-R3.3-P4-C8	6.9	8	3.4	240	667	367	372

Table 4-2 summarize the parametric study performed with case ID, overall reinforcement ratio, bars in the compression zone, and compression reinforcement ratio. The first peak load and its corresponding moment were compared for all case IDs. It can be observed that the trend had shown a marginal increase in peak load and flexural bending moment resistance with the increase of compression reinforcement ratio. Also, the bending moment resistance was calculated with and without considering the P-delta effect.

CHAPTER 5 CONCLUSION AND RECOMMENDATIONS

In this research program, a total of nine concrete beams reinforced with glass fiber reinforced polymer bars measuring 330 mm x 430 mm in cross-sectional shape and 3100 mm length were investigated both experimentally and analytically to study the combined effect of bending and shear when subjected to low axial loads. All specimens were divided into three groups of reinforcement ratio 1.7%, 2.5%, and 3.3% and tested under four-point bending under varying axial load of zero, 125 kN, and 250 kN. The analytical model was developed to verify the experimental results and perform the parametric study for different parameters. Based on the presented test results and comparison, the following conclusions were drawn:

- A coupon test was performed for the GFRP bars to determine the compression and tensile properties to verify the material used in this research. In the compression test, the method was perfectly implemented to obtain the mode of failure as crushing of GFRP bar at free length between the anchor, which was 100% successful in using this test method.
- The coupon test found that the modulus of elasticity in the GFRP bar's compression was slightly more than the modulus of elasticity in tension. The compression strength of the GFRP bar was noted as 70% of the tensile strength.
- All the GFRP beams tested had shown the crushing of concrete in the compression side as the flexural failure, which was the preferred mode of failure for the beam designed as an over-reinforced section refrain from tension side GFRP rupture. However, loading on the test specimen continued after concrete crushing until the beam's final failure, which was shear due to the diagonal tension failure of concrete and longitudinal compression reinforcement.
- Deflection, compressive and tensile strain had experienced the bilinear behavior showing the first linearity from the initial load stage to the first peak load of concrete crushing and continued with the second linearity until the failure.
- The GFRP bars in the compression side had experienced an average compressive strain of 7000 μmm/mm which was 50% of the ultimate compressive strain determined through material testing of coupons. Similarly, the tension side of the

GFRP bars had experienced an average tensile strain of 13000 μmm/mm equivalent to 72 % of ultimate tensile strain to maintain the sectional equilibrium with increasing bending resistance of test specimen.

- P-M interaction diagram developed based on the analytical model following ACI 440.1R-15 (ACI 2015) and CSA S806-12 (CSA 2012) showed that the moment capacity of the GFRP beam predicted was closer to experimental results. In other words, the moment capacity based on experimental test data was greater than or equal to 90% of the analytical model.
- The effect of low axial load on the GFRP beam from the P-M interaction diagram shows that the beam's ultimate moment capacity was reduced with inducted axial load of 2% at the reinforcement ratio of 2.5% and 3.3%. The axial load that had caused the impact to reduce the moment capacity was more pronounced in higher reinforcement ratio than lower reinforcement ratio, which had shown a slight increase. However, more testing was required to confirm this effect due to axial load.
- Moment-curvature model developed using numerical integration method considering the Thorenfedt et al. (1987) stress-strain curve method to predict GFRP beam's behavior had revealed a good agreement with the experimentally plotted moment-curvature curve.
- The load-deflection model predicted from the moment-curvature analytical model using the moment area method, including the shear deformation, showed the analytical model's stiffness was slightly higher than the experimental load-deflection model, which experienced relatively more deflection. Furthermore, it was observed that the rate at which the deflection decreases directly influenced the increase of the reinforcement ratio.
- The parametric study was performed based on the developed analytical model to investigate further the behavior of concrete beam reinforced with GFRP bars considering five significant parameters such as reinforcement ratio, concrete strength, cross-sectional shape, GFRP modulus, and axial load. It was observed that reinforcement ratio and cross-sectional shape were a more critical parameter in

controlling the lower end of the P-M interaction diagram, which causes the reduction in ultimate bending capacity with induced low axial load.

- Theoretical shear strength prediction based on the Canadian codes (CSA 2012) and (CSA 2014) found to be underestimated compared to experimental results. However, the shear strength predicted by the American code (ACI 2015) was conservative and on the higher side against the experimental results.

Following additional future experimental research on concrete beam reinforced with GFRP bars is recommended based on the above findings and conclusions drawn from the experimental and analytical study.

- Effect of low axial load less than 10% of ultimate beam axial capacity should not be ignored in concrete beam reinforced with FRP as it may reduce the ultimate bending resistance in some cases at a higher reinforcement ratio
- Varying the reinforcement ratio and percentage of low axial load to further study the effect in reduction of ultimate moment capacity of the GFRP concrete beam
- For the moment-curvature model, the inclusion of Strut and tie behavior considering the compressive force due to the diagonal tension strut, which can accommodate the additional bending capacity contribution from the GFRP bars after concrete crushing until the second peak load.
- Shear span to depth ratio and shear reinforcement parameters, mainly to isolate the flexural and shear failure modes.
- More analytical work will be required in developing the shear strength model for GFRP concrete beam to accurately predict the ultimate shear strength capacity effectively considering the GFRP stirrups contribution.

BIBLIOGRAPHY

Abdelkarim, O. I., A. Ahmed, E., M. Mohamed, H., Benmokrane, B. (2019). "Flexural Strength and Serviceability Evaluation of Concrete Beams Reinforced with Deformed GFRP Bars." *Engineering Structures*, 186(2019), 282-296.

ACI Committee 318. (2019) – *Building Code Requirements for Structural Concrete*, ACI 318-19, American Concrete Institute, Farmington Hills, MI, USA

ACI Committee 440. (2015) – Guide for the Design and Construction of Structural Concrete Reinforced with Fiber-Reinforced Polymer (FRP) Bars, ACI 440.1R-15, American Concrete Institute, Farmington Hills, MI, USA

Ahmed, E. A., El-Salakawy, E. F., Benmokrane, B. (2010). "Performance Evaluation of Glass Fiber-Reinforced Polymer Shear Reinforcement for Concrete Beams." *ACI Structural Journal*, (2010), 107-S06.

AlAjarmeh, O.S., Manolo, A. C., Benmokrane, B., Vijay, P.V., Ferdous, W., Mendis, P. (2019). "Novel Testing and Characterization of GFRP Bars in Compression." *Construction and Building Materials*, vol.225, 2019, pp. 1112-1126. https://doi:10.1016/j.conbuildmat.2019.07.280.

Arivalagan, S. (2012). "Engineering Performance of Concrete Beam Reinforced with GFRP Bars and Stainless Steel." *Global Journal of Researches in Engineering*, Volume-12 Issue-1 (2012), 0975-5861.

ASCE: American Society of Civil Engineers (2021) - Report Card for America's Infrastructure

ASTM. (2018). C33/C33M – Standard Specification for Concrete Aggregates, ASTM International, West Conshohocken, PA, USA

ASTM. (2012). C39/C39M – Standard Test Method for Compressive Strength of Cylindrical Concrete Specimens, ASTM International, West Conshohocken, PA, USA

ASTM. (2020). C109/C109M – Standard Test Method for Hydraulic Cement Mortars, ASTM International, West Conshohocken, PA, USA

ASTM. (2018). C1611/C1611M – Standard Test Method for Slump Flow of Self-Consolidating Concrete, ASTM International, West Conshohocken, PA, USA

ASTM. (2015). D695 – Standard Test Method for Compressive Properties of Rigid Plastics, ASTM International, West Conshohocken, PA, USA

ASTM. (2016). D7205/D7205M – Standard Test Method for Tensile Properties of Fiber Reinforced Polymer Matrix Composite Bars, ASTM International, West Conshohocken, PA, USA

ASTM. (2017). D7957/D7957M – Standard Specification for Solid Round Glass Fiber Reinforced Polymer Bars for Concrete Reinforcement, ASTM International, West Conshohocken, PA, USA

Bank, L. C. (2003). "Structural Design with FRP Materials." *Composites for Construction.*

CSA. (2012) – Code for the Design and Construction of Building Structures with Fiber-Reinforced Polymers, CSA S806-12, Canadian Standards Association, Mississauga, ON, Canada

CSA. (2014) – Canadian Highway Bridge Design Code, CSA S6-14, Canadian Standards Association, Mississauga, ON, Canada

CSA. (2015) – Code for the Design of Concrete Structures, CSA A23.3-14, CSA Group, Toronto, ON, Canada

CSA. (2019) – Canadian Highway Bridge Design Code, CSA S6-19, Canadian Standards Association, Mississauga, ON, Canada

CSA S807-19 – Specification for Fiber Reinforced Polymers, Canadian Standards Association, Mississauga, ON, Canada

De Luca, A., Matta, F., Dong, Nanni, A. (2010). "Behavior of Full-Scale Glass Fiber-Reinforced Polymer Reinforced Concrete Columns under Axial Load." *ACI Structural Journal*, (2010), 107-S58.

Elchalakani, M., Karrech, A., Dong, M., Mohamed Ali, M. S., Yang, B. (2018). "Experiments and Finite Element Analysis of GFRP Reinforced Geopolymer Concrete Rectangular Columns Subjected to Concentrix and Eccentric Axial Loading." *Structures 14*, (2018), 273-289.

Elgabbas, F., Vincent, P., Ahmed, E. A., Benmokrane, B. (2016). "Experimental Testing of Basalt-Fiber-Reinforced Polymer Bars in Concrete Beams." *Composites Part B*, 91(2016), 205-218.

El-Nemr, A., Ahmed, E. A., Benmokrane, B. (2013). "Flexural Behavior and Serviceability of Normal and High-Strength Concrete Beams Reinforced with Glass Fiber-Reinforced Polymer Bars." *ACI Structural Journal*, 110(6), 1077-1087.

El-Nemr, A., Ahmed, E. A., El-Safty, A., Benmokrane, B. (2018). "Evaluation of the Flexural Strength and Serviceability of Concrete Beams Reinforced with Different Types of GFRP Bars." *Engineering Structures*, 173(2018), 606-619.

Fillmore, B., Sadeghian, P. (2018). "Contribution of Longitudinal Glass Fiber-Reinforced Polymer Bars in Concrete Cylinders under Axial Compression." *Canadian Journal of Civil Engineering*, 45(2018), 458-468.

Guerin, M., Mohamed, H. M., Benmokrane, B., C. K. Shield., A. Nanni. (2018). "Effect of Glass Fiber-Reinforced Polymer Reinforcement Ratio on Axial-Flexural Strength of Reinforced Concrete Columns." *ACI Structural Journal*, 115(4), 1049-1061.

Huang, Z., Tu, Y., Meng, S., Sabau, C., Popescu, C., Sas, G. (2019). "Experimental Study on Shear Deformation of Reinforced Concrete Beams using Digital Image Correlation." *Engineering Structures*, 181 (2019) 670-698.

Hasan, H. A., Karim, H., Sheikh, M, N., Hadi, M. N. S. (2019). "Moment-Curvature Behavior of Glass Fiber-Reinforced Polymer Bar-Reinforced Normal-Strength Concrete and High-Strength Concrete Columns." *ACI Structural Journal*, 116-S78.

ISIS Design Manual No.3, Reinforcing Concrete Structures with Fiber Reinforced Polymers (2007). Canadian Network of Center of Excellence for Intelligent Sensing for Innovative Structures, Winnipeg, Manitoba, Canada.

Karim, H., Sheikh, M. N., Hadi, M. N. S. (2016). "Axial Load-Axial Deformation Behavior of Circular Concrete Columns Reinforced with GFRP Bars and Helices." *Construction and Building Materials*, 112(2016), 1147-1157.

Khorramian, K., Sadeghian, P. (2017). "Experimental and Analytical Behavior of Short Concrete Columns Reinforced with GFRP Bars under eccentric loading." *Engineering Structures*, 151(2017), 761-773.

Khorramian, K., Sadeghian, P. (2018). "New testing method of GFRP bars in compression." *CSCE Annual Conference*, MA7-1-MA7-9, Canadian Society for Civil Engineering, Montreal, Canada.

Khorramian, K., Sadeghian, P. (2019b). "Material Characterization of GFRP bars in compression using a new test method." *Journal of Testing and Evaluation 49*, JTE20180873, https://doi.org/10.1520/JTE20180873.

Khorramian, K., Sadeghian, P. (2020). "Experimental Investigation of Short and Slender Rectangular Concrete Columns Reinforced with GFRP Bars under Eccentric Axial Loads." *Journal of Composite Construction*, 2020, 24(6), 04020072.

Maranan, G. B., Manalo, A. C., Benmokrane, B., Karunasena, W., Mendis, P. (2016). "Behavior of Concentrically Loaded Geopolymer-Concrete Columns Reinforced Longitudinally and Transversely with GFRP Bars." *Engineering Structures*, 117(2016), 422-436.

Maranan, G. B., Manalo, A. C., Benmokrane, B., Karunasena, W., Mendis, P., Nguyen, T. Q. (2018). "Shear Behavior of Geopolymer-Concrete Beams Transversely Reinforced with Continuous Rectangular GFRP Composite Spirals." *Composite Structures*, 187 (2018), 454-465.

Mirmiran, A., Shahawy, M., El Khoury, C., Naguib, W. (2000). "Large Beam-Column Tests on concrete-filled Composite Tubes." *ACI Structural Journal*, 97-S29.

Mohamed, H. M., Afifi, M. Z., Benmokrane, B. (2014). "Performance Evaluation of Concrete Columns Reinforced Longitudinally with FRP Bars and Confined with FRP Hoops and Spirals under Axial Load." *Journal of Bridge Engineering*, 19(7), 04014020.

Ovitigala, T., Ibrahim, M. A., A. Issa, M. (2016). "Serviceability and Ultimate Load Behavior of Concrete Beams Reinforced with Basalt Fiber-Reinforced Polymer Bars." *ACI Structural Journal*, 113(4), 757-768.

Popovics, S. (1973). "A Numerical Approach to the Complete Stress-Strain Curve of Concrete." *Cement and Concrete Research Journal*, 3(5), 583-599.

Sadeghian, P., Fam, A. (2014). "Strengthening Slender Reinforced Concrete Columns Using High-Modulus Bonded Longitudinal Reinforcement for Buckling Control." *Journal of Structural Engineering*, American Society of Civil Engineers, 04014127(12), 0733-9445.

Said, M., Adam, M. A., Mahmoud, A. A., Shanour, A. S. (2016). "Experiments and Analytical Shear Evaluation of Concrete Beams Reinforced with Glass Fiber Reinforced Polymer Bars." *Construction and Building Materials*, 102 (2018) 574-591.

Salah-Eldin, A., Mohamed, H. M., Benmokrane, B. (2019). "Axial-Flexural Performance of High-Strength-Concrete Bridge Compression Members Reinforced with Basalt-FRP Bars and Ties: Experimental and Theoretical Investigation." *Journal of Bridge Engineering*, 24(7), 04019069.

Salah-Eldin, A., Mohamed, H. M., Benmokrane, B. (2019). "Structural Performance of High-Strength-Concrete Columns reinforced with GFRP Bars and Ties Subjected to Eccentric Loads." *Engineering Structures*, 185(2019), 286-300.

Salah-Eldin, A., Mohamed, H. M., Benmokrane, B. (2020). "Effect of GFRP Reinforcement Ratio on the Strength and Effective Stiffness of High-Strength Concrete Columns: Experimental and Analytical Study." *Journal of Composite Construction*, 24(5), 04020055.

Thorenfeldt, E., Tomaszewicz, A., Jensen, J.J. (1987). "Mechanical Properties of High Strength Concrete and Application to Design." *Proc., Symp., on utilization of High-Strength Concrete*, 149-159. Trondheim, Norway: Tapir.

Wright, J. K., Richart, F. E. (2016). “Reinforced Concrete Mechanics and Design (7th Edition).” The *University of Michigan.*

Zhu, H., Cheng, S., Gao, D., Neaz, S.M., Li, C. (2018). “Flexural Behavior of Partially Fiber-reinforced high-strength concrete beams reinforced with FRP bars.” *Construction and Building Materials*, 161(2018), 587-597.

APPENDIX A Experimental Test Data

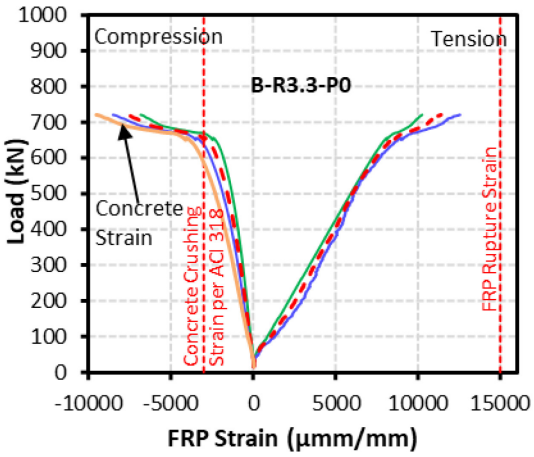

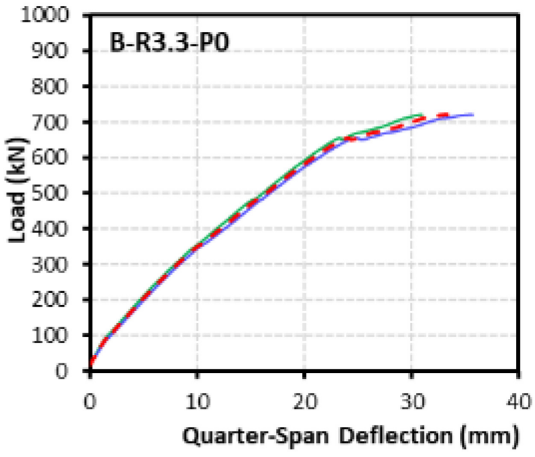

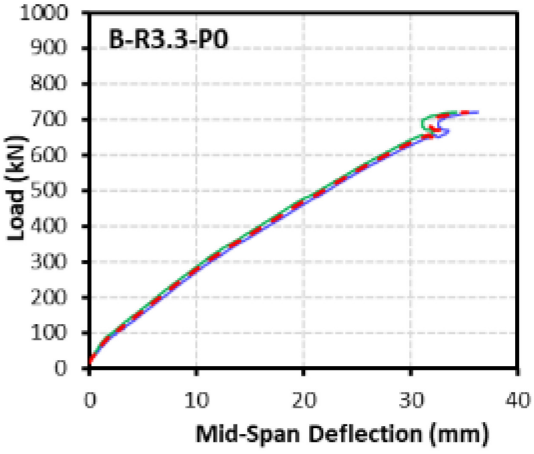

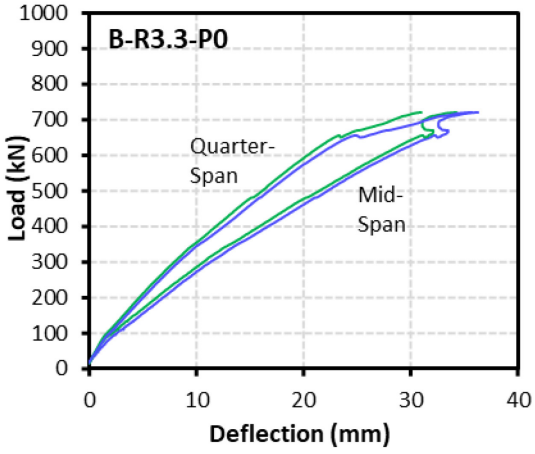

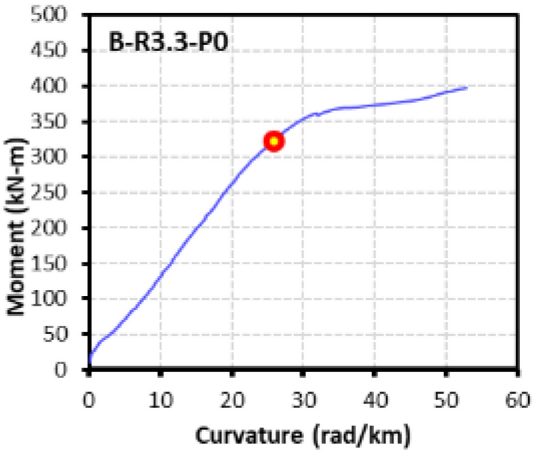

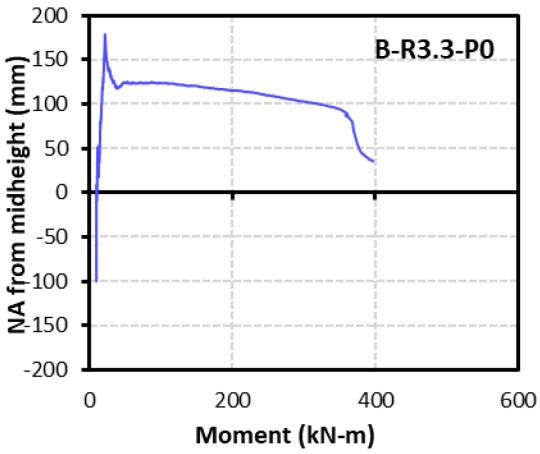

B-R3.3-P0 (ρ = 3.3%, Axial = 0 kN)

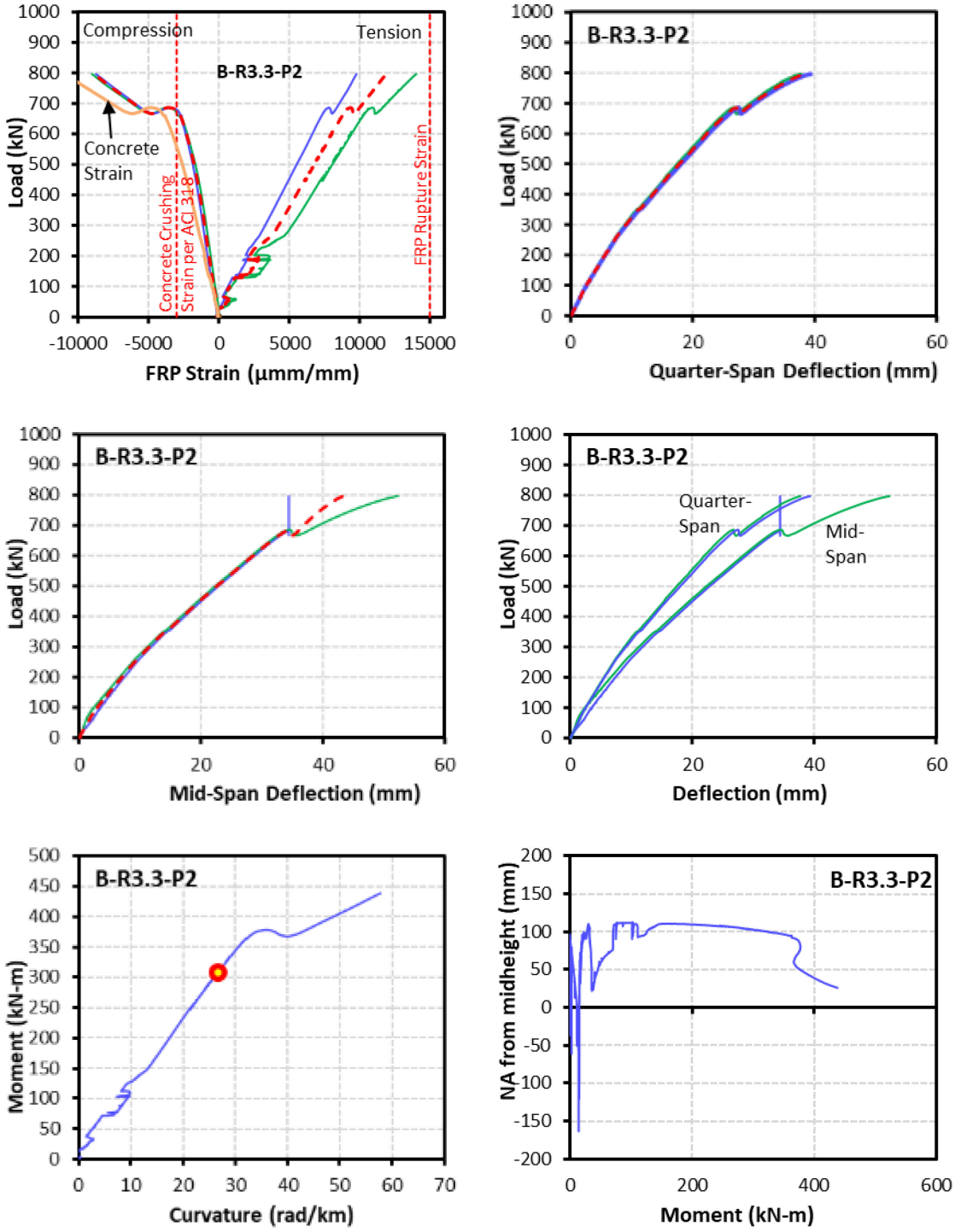

B-R3.3-P2 (ρ = 3.3%, Axial = 125 kN)

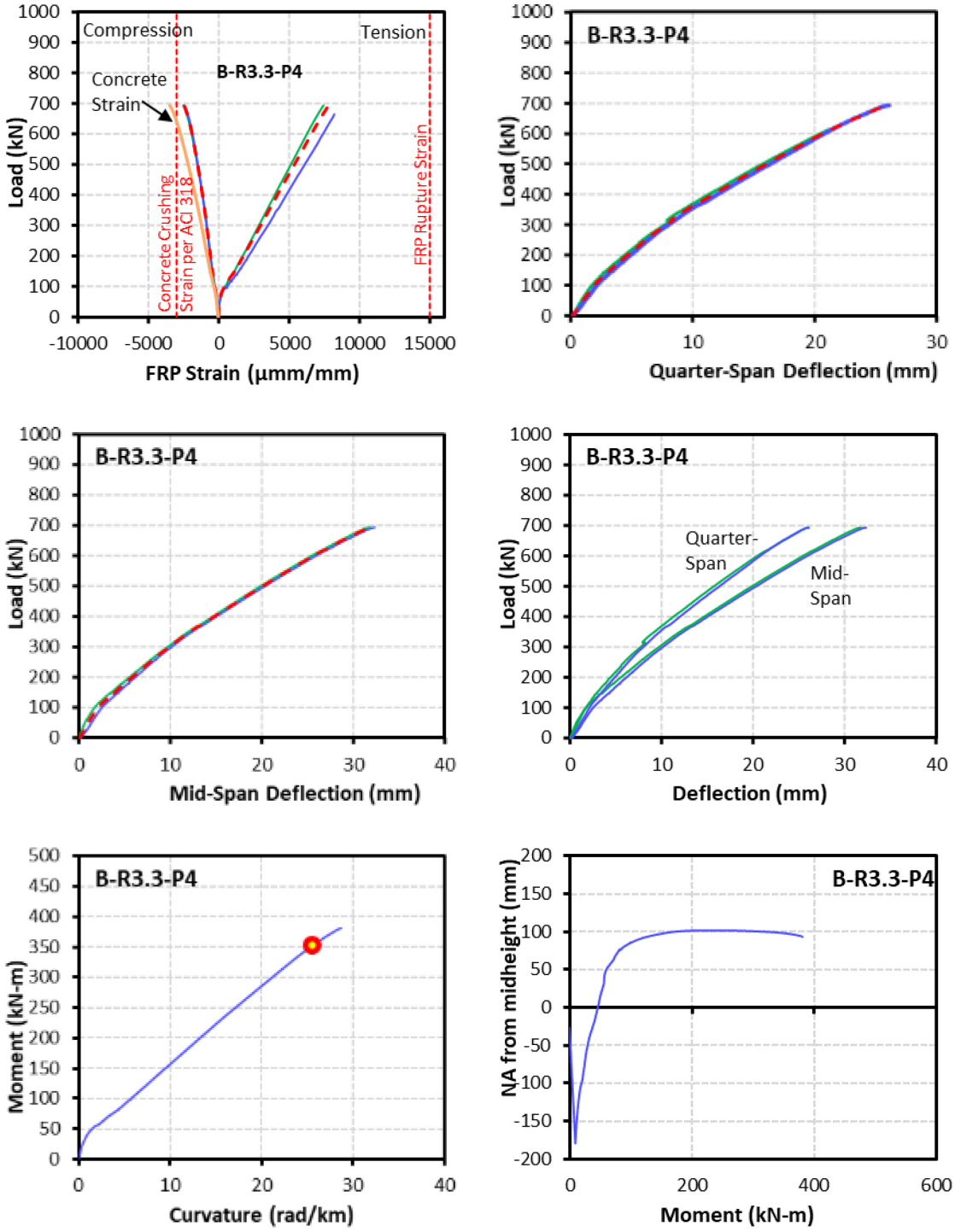

B-R3.3-P4 (ρ = 3.3%, Axial = 250 kN)

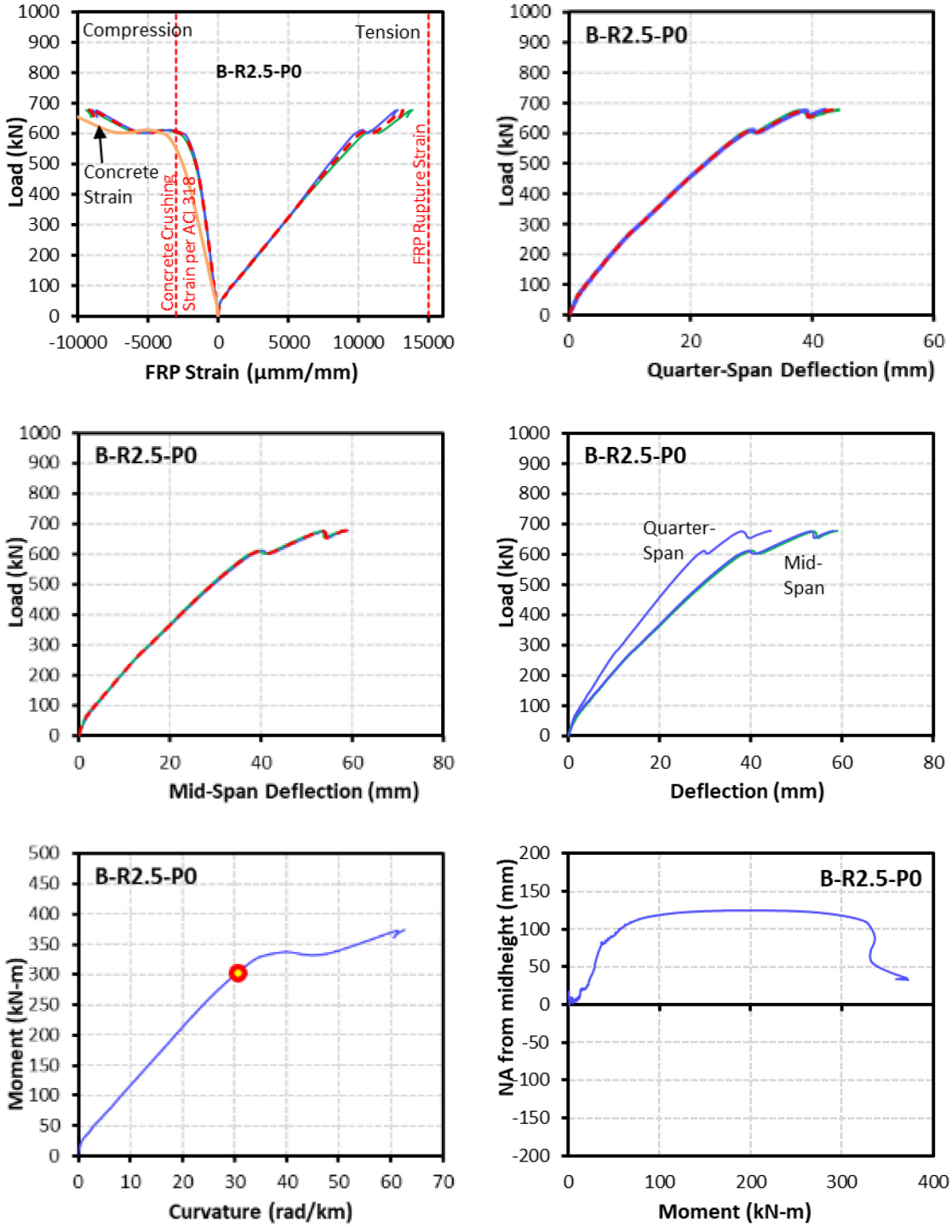

B-R2.5-P0 (ρ = 2.5%, Axial = 0 kN)

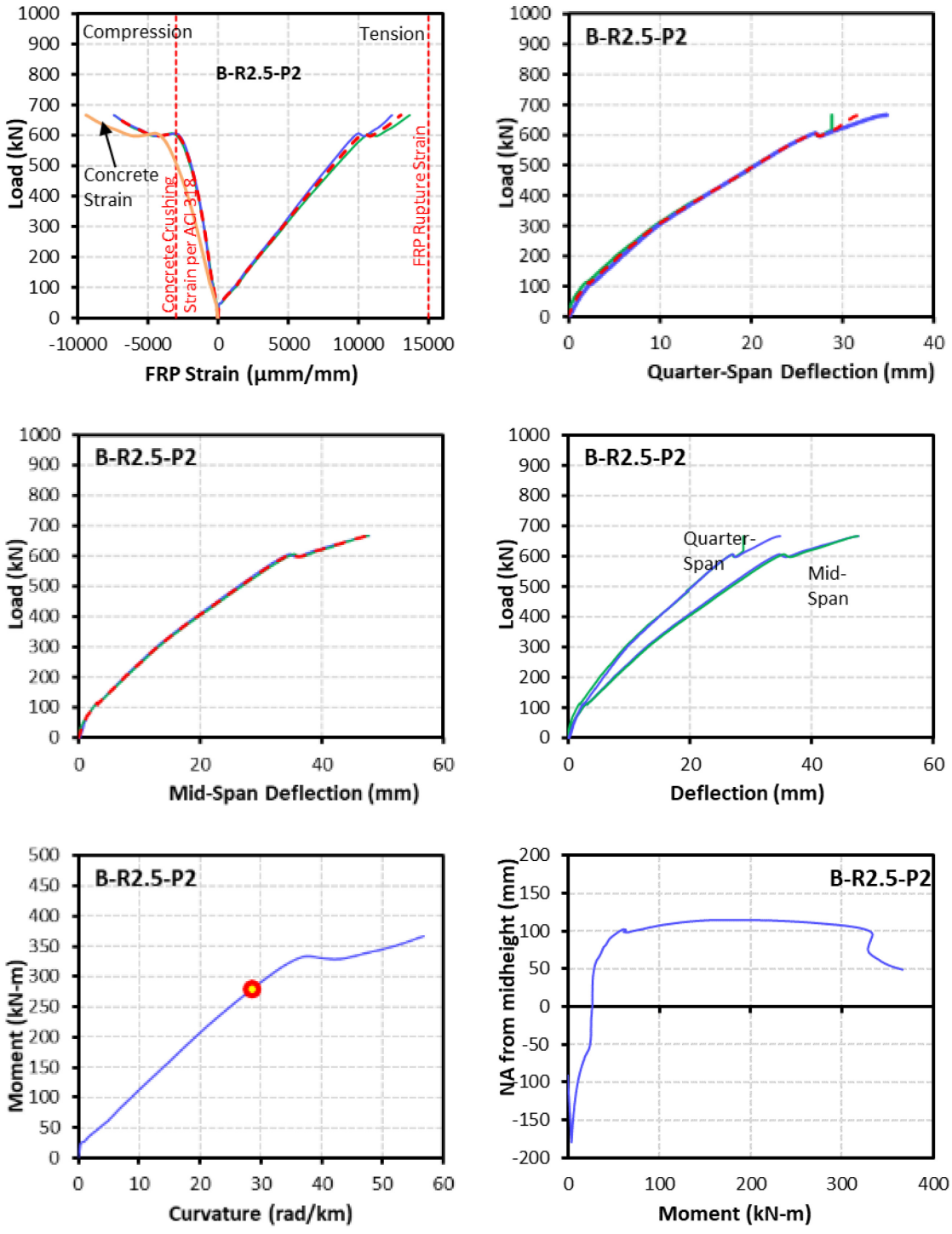

B-R2.5-P2 (ρ = 2.5%, Axial = 125 kN)

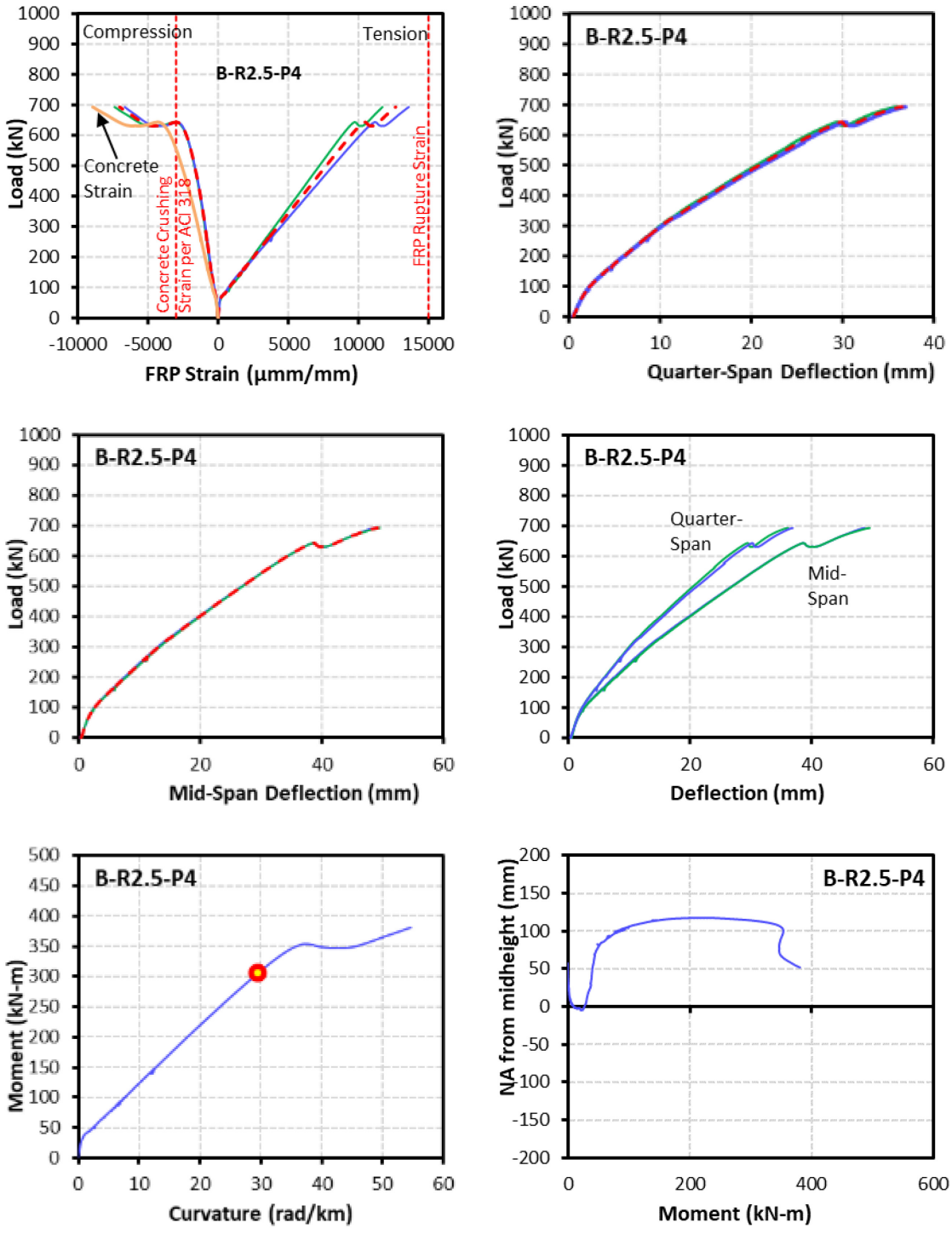

B-R2.5-P4 (ρ = 2.5%, Axial = 250 kN)

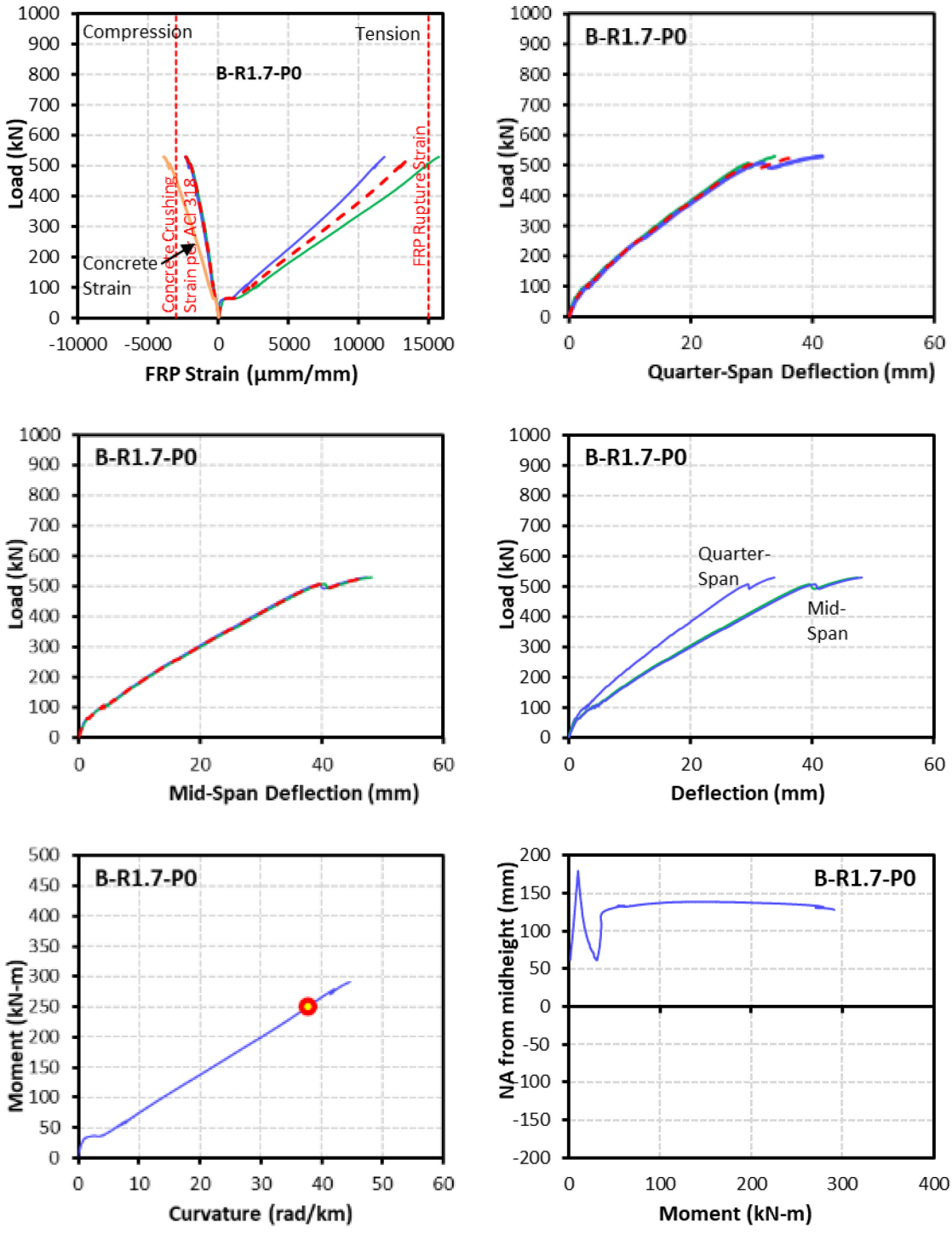

B-R1.7-P0 (ρ = 1.7%, Axial = 0 kN)

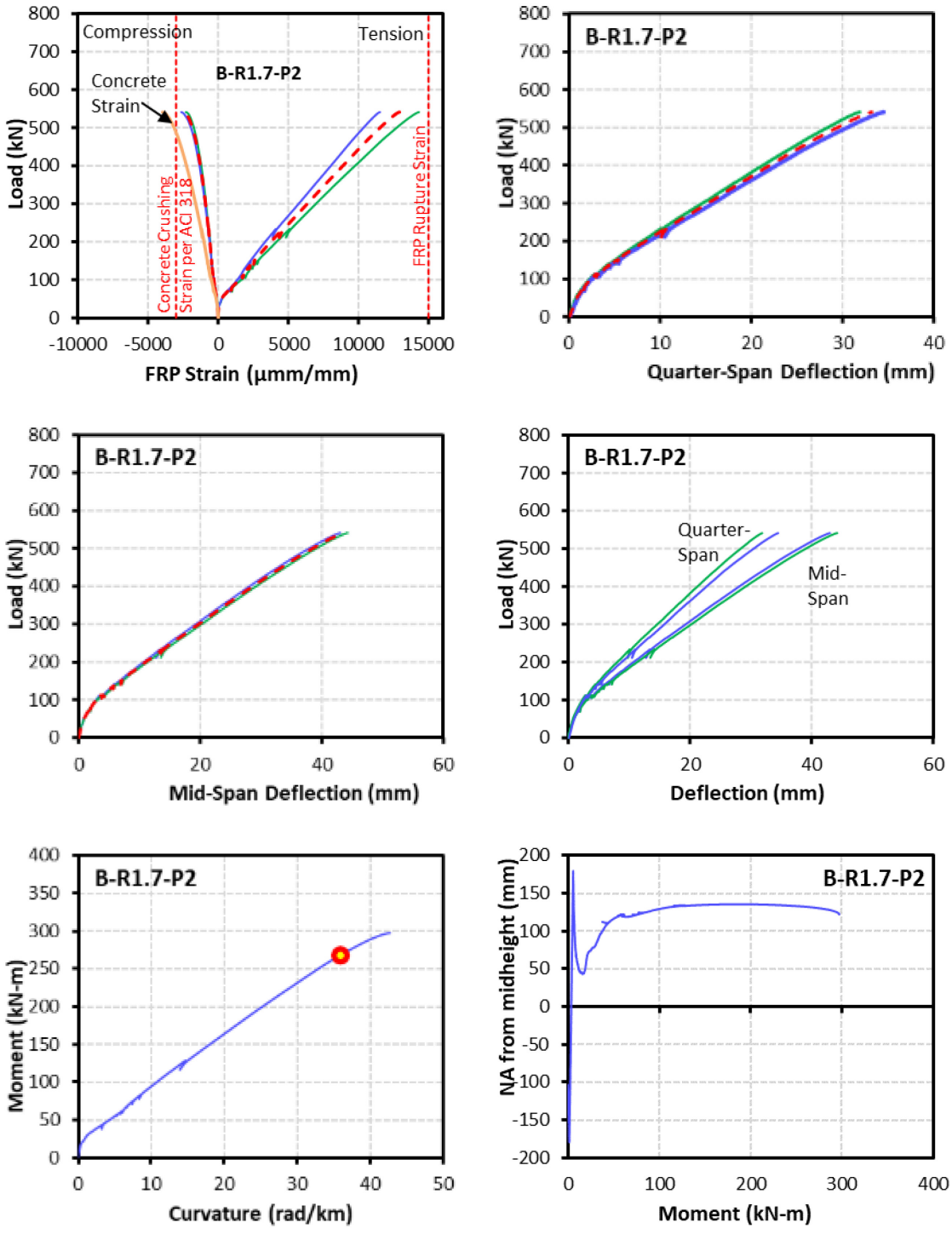

B-R1.7-P2 (ρ = 1.7%, Axial = 125 kN)

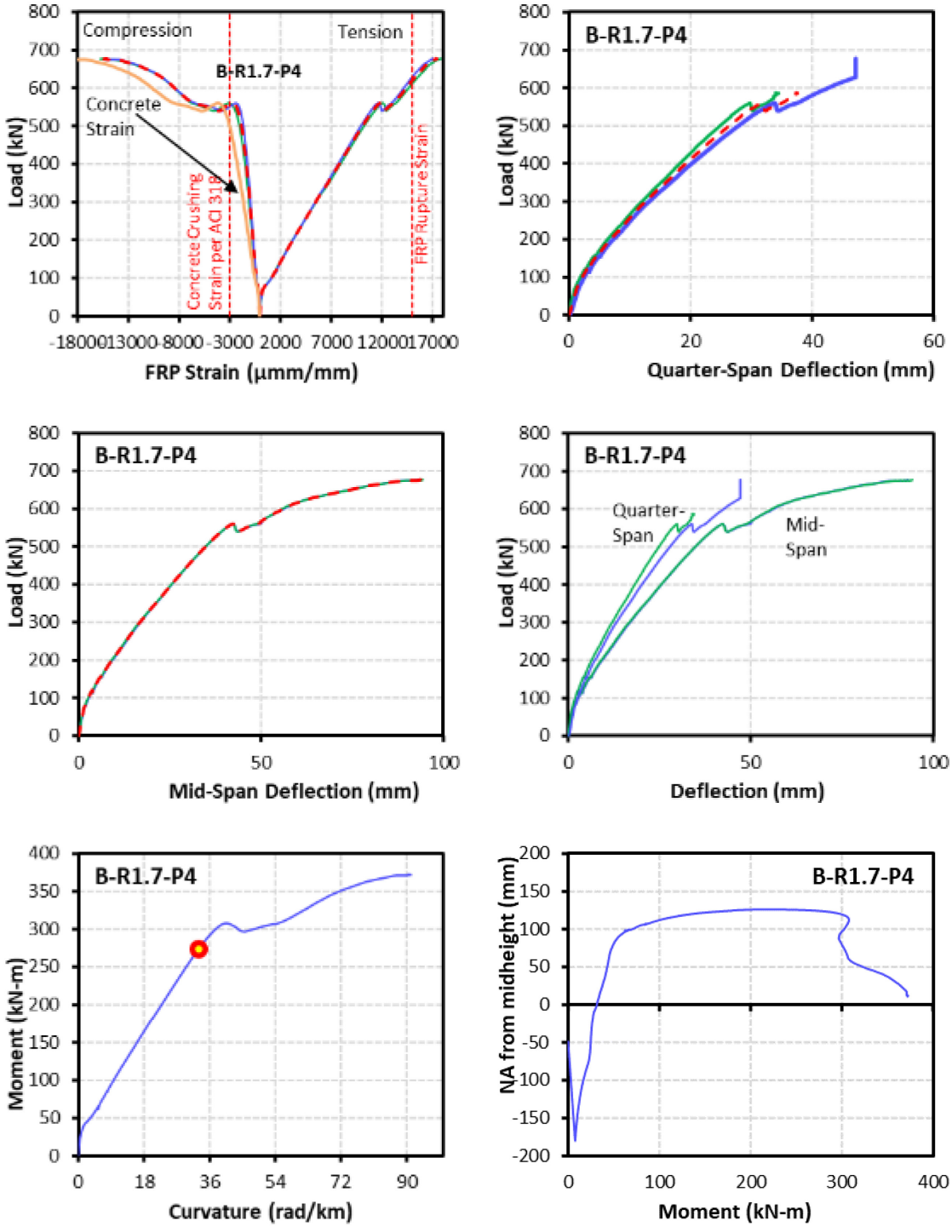

B-R1.7-P4 (ρ = 1.7%, Axial = 250 kN)

APPENDIX B Mathcad Analytical Model Code

B1. Introduction

In this research, the analytical model was developed to perform the beam cross-sectional analysis and determine the axial and moment capacity of the GFRP beam for the different neutral axis to plot the P-M interaction diagram using MATHCAD Prime software and to compare the flexural behavior with the experimental test data. The model was initiated with the assumption of 19 neutral axes, but the entire procedure was repeated for each neutral axis in determining the axial load and moment capacity of the beam cross-section. A strain profile was formed for each neutral axis by finding the strain in the top and bottom GFRP bars; moving forward, the corresponding compressive and tensile stress in the GFRP bars were determined. The parabolic stress block was divided into twenty equal strips to calculate the concrete compressive stress by programming using the Summation function in MATHCAD. Finally, the axial load and bending moment resistance obtained based on the 19 neutral axis serves as the data point to plot the P-M interaction diagram.

B2. Mathcad code for P-M Interaction

Material Properties

$f'_c := 44\ MPa$ $E_{ft} := 45000\ MPa$ $E_{ftc} := 48063\ MPa$

$E_{fc} := 4500 \cdot \sqrt[2]{f'_c} \cdot \frac{N^{\frac{1}{2}}}{mm}$ $E_{fc} = 29850\ MPa$

$f_{fu} := 808\ MPa$ Bar #8 (aslan) $f_{fcu} := 569\ MPa$

Dimensions

$b := 330\ mm$ $\varepsilon_c := 0.003$

$h := 430\ mm$

Reinforcement Data

No. of Bars	$n := 10$	$cover := 25\ mm$	
1st Layer	$n_1 := 2$	Layer Spacing	$L_s := 25\ mm$
2nd Layer	$n_2 := 0$	Dia. of Stirrups	$d_s := 10\ mm$
3rd Layer	$n_3 := 0$		
4th Layer	$n_4 := 5$		
5th Layer	$n_5 := 3$		
Dia. of Bars	$d_b := 25\ mm$		

Area of Longitudinal Reinforcement

Area of Bar	$A := 506.7\ mm^2$	
Total Area of Longitudinal Reinforcement	$A_f := n \cdot A$	
	$A_f = 5067\ mm^2$	
Gross cross-sectional Area	$A_g := b \cdot h$	
	$A_g = 141900\ mm^2$	
Area of Steel 1st Layer	$A_{f1} := n_1 \cdot A$	$A_{f1} = 1013.4\ mm^2$
Area of Steel 2nd Layer	$A_{f2} := n_2 \cdot A$	$A_{f2} = 0\ mm^2$
Area of Steel 3rd Layer	$A_{f3} := n_3 \cdot A$	$A_{f3} = 0\ mm^2$
Area of Steel 4th Layer	$A_{f4} := n_4 \cdot A$	$A_{f4} = 2533.5\ mm^2$
Area of Steel 5th Layer	$A_{f5} := n_5 \cdot A$	$A_{f5} = 1520.1\ mm^2$

Neutral Axis Depth Corresponding to Balanced Condition

Beam effective depth $d := h - cover - d_s - d_b - 0.0125 \cdot m$

$d = 0.358\ m$

Reinforcement Ratio $R_r := \frac{(A_{f4} + A_{f5})}{b \cdot d} \cdot 100 = 3.436$

$\varepsilon_{fu} := \frac{f_{fu}}{E_{ft}}$ $\varepsilon_{fu} = 0.018$

Neutral axis depth $c_b := \frac{\varepsilon_c}{\varepsilon_c + \varepsilon_{fu}} \cdot d$

$c_b = 51.18\ mm$

Estimate the neutral axis depth

$c_2 := 112\ mm$

Effective depth for each reinforcement layer

$d_1 := cover + \frac{d_b}{2} + d_s = 47.5\ mm$

$d_2 := d_1 + L_s + \frac{d_b}{2} = 85\ mm$

$d_3 := \text{if } n_3 > 0 \ \frac{h}{2} \ \text{else} \ 0.\ mm$

$d_3 = 0\ mm$

$$d_4 := h - cover - d_s - d_b - L_s - \frac{d_b}{2} = 332.5 \ mm$$

$$d_5 := h - cover - d_s - \frac{d_b}{2} = 382.5 \ mm$$

$$\varepsilon_{f\_ti} := \varepsilon_c \cdot \left(\frac{c_{ti} - d_{ti}}{c_{ti}} \right)$$

$$\varepsilon_{f\_bi} := \varepsilon_c \cdot \left(\frac{c_{bi} - d_{bi}}{c_{bi}} \right)$$

$$\varepsilon_{fi} := \text{stack}\left(\varepsilon_{f\_ti}, \varepsilon_{f\_mi}, \varepsilon_{f\_bi}\right)$$

$$\varepsilon_{fi} = \begin{bmatrix} 0.002 \\ 0.001 \\ 0 \\ -0.006 \\ -0.007 & \dots \end{bmatrix}$$

Computation of stresses in each reinforcement

$\varepsilon_{fi_{0,0}} = 0.00173$ $\quad$ $\varepsilon_{fi_{3,0}} = -0.0059$ $\quad$ $\varepsilon_{fi_{4,0}} = -0.0072$

$$f_{s1\_2} := \begin{cases} f_{fu} & \text{if } \varepsilon_{fi_{0,0}} > \varepsilon_{fu} \\ -f_{fu} & \text{else if } \varepsilon_{fi_{0,0}} < -\varepsilon_{fu} \\ E_{ftc} \cdot \varepsilon_{fi_{0,0}} & \text{else} \end{cases}$$

$$f_{s4\_2} := \begin{cases} f_{fu} & \text{if } \varepsilon_{fi_{3,0}} > \varepsilon_{fu} \\ -f_{fu} & \text{else if } \varepsilon_{fi_{3,0}} < -\varepsilon_{fu} \\ E_{ft} \cdot \varepsilon_{fi_{3,0}} & \text{else} \end{cases}$$

$$f_{s5\_2} := \begin{cases} f_{fu} & \text{if } \varepsilon_{fi_{4,0}} > \varepsilon_{fu} \\ -f_{fu} & \text{else if } \varepsilon_{fi_{4,0}} < -\varepsilon_{fu} \\ E_{ft} \cdot \varepsilon_{fi_{4,0}} & \text{else} \end{cases}$$

$f_{s1\_2} = 83.037 \ MPa$ $\quad$ $f_{s4\_2} = -265.781 \ MPa$ $\quad$ $f_{s5\_2} = -326.049 \ MPa$

$$f_{si} = \begin{bmatrix} 83.037 \\ 34.76 \\ 0 \\ -265.781 \\ -326.049 \quad \dots \end{bmatrix} MPa$$

Strain Computation for each fibre in Concrete

$$r := 0.8 + \frac{f'_c}{17 \cdot MPa} \qquad r = 3.388$$

$$k := 0.67 + \frac{f'_c}{62 \cdot MPa} \qquad k = 1.38$$

$$\varepsilon'_c := \frac{f'_c}{E_{fc}} \cdot \frac{r}{r-1} \qquad \varepsilon'_c = 0.0021$$

Stresses in concrete at each fibre

$$n := 20$$

$$\Delta y_2 := \frac{c_2}{n} \cdot \frac{1}{mm} \qquad n_2 := \text{round}\left(\frac{c_2 - h}{\Delta y_2 \cdot mm}\right) \qquad i_2 := 1, 2 .. n$$

$$\Delta y_2 = 5.6 \qquad n_2 = -57$$

$$C_{r2} := \left| \sum_{i_2=1}^{n} \frac{f'_c \cdot \left(\frac{\varepsilon_c \cdot \left(\left(i_2 \cdot \Delta y_2 - \frac{\Delta y_2}{2} \right) \cdot mm \right)}{c_2 \cdot \varepsilon'_c} \right) \cdot r}{r - 1 + \left(\frac{\varepsilon_c \cdot \left(\left(i_2 \cdot \Delta y_2 - \frac{\Delta y_2}{2} \right) \cdot mm \right)}{c_2 \cdot \varepsilon'_c} \right)^{r \cdot k}} \cdot b \cdot \Delta y_2 \cdot mm - \frac{f'_c \cdot \left(\frac{\varepsilon_c \cdot \left((c_2 - d_1) \right)}{c_2 \cdot \varepsilon'_c} \right) \cdot r}{r - 1 + \left(\frac{\varepsilon_c \cdot \left((c_2 - d_1) \right)}{c_2 \cdot \varepsilon'_c} \right)^{r \cdot k}} \cdot A_{fl} \right|$$

$$C_{r2} = 1088.635 \ kN$$

Stresses in GFRP

$$F_{rs1} := \phi_s \cdot A_{f1} \cdot f_{s1}$$

$$F_{rs1} = [84.15 \quad \ldots] \ \mathit{kN}$$

$$F_{rs2} := \phi_s \cdot A_{f2} \cdot f_{s2}$$

$$F_{rs2} = [0 \quad \ldots] \ \mathit{kN}$$

$$F_{rs3} := \phi_s \cdot A_{f3} \cdot f_{s3}$$

$$F_{rs3} = [0 \quad \ldots] \ \mathit{kN}$$

$$F_{rs4} := \phi_s \cdot A_{f4} \cdot f_{s4}$$

$$F_{rs4} = [-673.357 \quad \ldots] \ \mathit{kN}$$

$$F_{rs5} := \phi_s \cdot A_{f5} \cdot f_{s5}$$

$$F_{rs5} = [-495.627 \quad \ldots] \ \mathit{kN}$$

Resultant Stresses in Concrete and FRP

$$P_{ri} := C_{ri} + \left(F_{rs1} + F_{rs2} + F_{rs3} + F_{rs4} + F_{rs5}\right)$$

$$P_{ri} = [3.802 \quad \ldots] \ \mathit{kN}$$

$$P_r := P_{ri}$$

$$P_r = [3.802 \quad \ldots] \ \mathit{kN}$$

Factored Moment Resistance

$$M_{rc2} := \left\| \sum_{i_2=1}^{n} \frac{f'_c \cdot \left(\frac{\varepsilon_c \cdot \left(\left(i_2 \cdot \Delta y_2 - \frac{\Delta y_2}{2} \right) \cdot mm \right)}{c_2 \cdot \varepsilon'_c} \right) \cdot r}{r - 1 + \left(\frac{\varepsilon_c \cdot \left(\left(i_2 \cdot \Delta y_2 - \frac{\Delta y_2}{2} \right) \cdot mm \right)}{c_2 \cdot \varepsilon'_c} \right)^{r \cdot k}} \cdot b \cdot \Delta y_2 \cdot \left(\left(i_2 \cdot \Delta y_2 - \frac{\Delta y_2}{2} \right) mm - c_2 + \frac{h}{2} \right) \cdot mm - \frac{f'_c \cdot \left(\frac{\varepsilon_c \cdot \left((c_2 - d_1) \right)}{c_2 \cdot \varepsilon'_c} \right) \cdot r}{r - 1 + \left(\frac{\varepsilon_c \cdot \left((c_2 - d_1) \right)}{c_2 \cdot \varepsilon'_c} \right)^{r \cdot k}} \cdot A_{f1} \cdot \left(\frac{h}{2} - d_1 \right) \right\|$$

$M_{rc2} = 184.077 \ kN \cdot m$

$F_{rs1_{0,0}} = 84.15 \ kN$

$M_{rs1_{0,0}} := F_{rs1_{0,0}} \cdot \left(\frac{h}{2} - d_1 \right)$

$M_{rs1_{0,0}} = 14.095 \ kN \cdot m$

$F_{rs4_{0,0}} = -673.357 \ kN$

$M_{rs4_{0,0}} := F_{rs4_{0,0}} \cdot \left(\frac{h}{2} - d_4 \right)$

$M_{rs4_{0,0}} = 79.119 \ kN \cdot m$

$F_{rs5_{0,0}} = -495.627 \ kN$

$M_{rs5_{0,0}} := F_{rs5_{0,0}} \cdot \left(\frac{h}{2} - d_5 \right)$

$M_{rs5_{0,0}} = 83.018 \ kN \cdot m$

$M_{ri} := M_{rci} + M_{rs1} + M_{rs2} + M_{rs3} + M_{rs4} + M_{rs5}$

$M_{ri} = [360.309 \quad \ldots] \ kN \cdot m$

$M_r := M_{ri}$

$M_r = [360.309 \quad \ldots] \ kN \cdot m$

B2. MATLAB code for Moment-Curvature

```
%%NUMERICAL MODELLING
%% FINDING NEUTRAL AXIS WITH SECANT METHOD
%% Defines initial guess of Neutral Axis
cc0 = 70;
%% Defines second initial guess of Neutral Axis
cc1 = 80;
err_max = 1E-6;
iter_max = 100;

% Get function at first two initial guesses
folder = fun(cc0);
fold = fun(cc1);

% Initize iteration count
colder = cc0;
```

```
cold = cc1;
%% Initialize loop iteration counter
iter = 0;
%% Initial value of err is set "large" to ensure enter loop.
err = 1;

%Iteration loop
while err > err_max & iter < iter_max

%Get cnew using Secant
   cnew = cold - fold * (colder - cold)/(folder - fold);

   %Update iteration
   iter = iter + 1;
   colder = cold;
   folder = fold;
   cold = cnew;

   %Get function values associated with new iterate
   fold = fun(cold);
   err = abs(fold);

end

if iter < iter_max
   'Neutral Axis for FRP Beam will be'
   cold
   'Iterations were'
   iter
else
   'No convergence'
end


function f_at_c = fun(cc)
%% MATERIAL PROPERTIES
%% Concrete Compressive Strength
f_c = 44;
%% FRP Elastic Modulus - Tension
Eft = 45000;
%% FRP Elastic Modulus - Compression
Efc = 48063;
%% FRP Tensile Strength
fft = 808;
%% FRP Compressive Strength
ffc = 569;
```

```
%% Ultimate Concrete strain
epsilon_c = 0.0001;
%% Concrete Elastic Modulus
Ec = 4500*sqrt(f_c);
%% Axial load
Axial = -250000;

%% DIMENSIONS
b = 330;        %% Beam Width
h = 430;        %% Beam Height
L = 2800;       %% Beam Length

%% REINFORCEMENT DATA
cover = 25;     %% Concrete Cover all around
Ls = 25;        %% Layer Spacing
db = 25;        %% Longitudinal Reinforcement Diameter
ds = 10;        %% Stirrups Diameter

%% Beam Effective Depth
ed = h - cover - ds - db - (Ls/2);
n = 6;          %% Number of Bars
n1 = 2;         %% 1st Reinforcement Layer
n2 = 0;         %% 2nd Reinforcement Layer
n3 = 0;         %% 3rd Reinforcement Layer
n4 = 2;         %% 4th Reinforcement Layer
n5 = 2;         %% 5th Reinforcement Layer
ntn = 4;        %% Tension Reinforcement
ncn = 2;        %% Compression Reinforcement

%% AREA OF LONGITUDINAL REINFORCEMENT
A = 506.7;      %% Area of Longitudinal reinforcement
Af1 = n1*A;     %% Area of FRP 1st Layer
Af2 = n2*A;     %% Area of FRP 2nd Layer
Af3 = n3*A;     %% Area of FRP 3rd Layer
Af4 = n4*A;     %% Area of FRP 4th Layer
Af5 = n5*A;     %% Area of FRP 5th Layer
%% STRESS AND STRAIN COMPUTATION
na = 20;        %% Number of Concrete Strips Considered
Row_frp = (ntn*A)/(b*ed);    %% Reinforcement Ratio
epsilon_fu = fft/Eft;        %% Ultimate FRP Strain


%% COMPUTATION OF STRAIN IN EACH CONCRETE FIBRE
   r = 0.8 + (f_c/17);
   kt = 0.67 + (f_c/62);
   epsilon_prime_c = (f_c/Ec)*(r/(r-1));
```

```
    epsilon = epsilon_prime_c/epsilon_c;

%% EFFECTIVE DEPTH FOR EACH REINFORCEMENT LAYER
%% Location of First row of FRP Bars
    d1 = cover + ds + (db/2);
%% Location of Second row of FRP Bars
    d2 = h - ed + Ls;
%% Location of Third row of FRP Bars
    d3 = 0;
%% Location of Fourth row of FRP Bars
    d4 = h - cover - ds - db - Ls - (db/2);
%% Location of Fifth row of FRP Bars
    d5 = h - cover - ds - (db/2);
    d = [d1 d2 d3 d4 d5];

%% STRAIN COMPUTATION FOR EACH REINFORCEMENT LAYER
    epsilon_f = epsilon_c*((cc - d)./cc)'

%% COMPUTATION OF STRESS IN EACH COMPRESSION REINFORCEMENT
    if epsilon_f > epsilon_fu
        fsac = ffc;
    elseif epsilon_f < -epsilon_fu
        fsac = -ffc;
    else
        fsac = Efc*epsilon_f;
    end

%% COMPUTATION OF STRESS IN EACH TENSION REINFORCEMENT
    if epsilon_f > epsilon_fu
        fsat = fft;
    elseif epsilon_f < -epsilon_fu
        fsat = -fft;
    else
        fsat = Eft*epsilon_f;
    end

%% COMPUTATION OF AXIAL LOAD IN GFRP
    Frsa1 = fsac(1,:)*Af1;
    Frsa2 = fsac(2,:)*Af2;
    Frsa3 = fsat(3,:)*Af3;
    Frsa4 = fsat(4,:)*Af4;
    Frsa5 = fsat(5,:)*Af5;

%% COMPUTATION OF MOMENT DUE TO AXIAL LOAD IN GFRP
     Mrsa1 = fsac(1,:)*Af1*((h/2)-d1);
     Mrsa2 = fsac(2,:)*Af2*((h/2)-d2);
```

```
    Mrsa3 = fsat(3,:)*Af3*((h/2)-d3);
    Mrsa4 = fsat(4,:)*Af4*((h/2)-d4);
    Mrsa5 = fsat(5,:)*Af5*((h/2)-d5);


%% Strip Thickness Compression Part
   Deltay = cc/na;
   for is = 1:na+1
      st(1,is) = ((f_c*(((is*Deltay)-(Deltay/2))./(cc*epsilon))*r)./(r-1+((((is*Deltay)-
(Deltay/2))./(cc*epsilon)).^(r*kt))))*b*Deltay;
   end

%% AXIAL DUE TO GFRP
   Cgf_R = (((f_c*((cc-d1)./(cc*epsilon))*r)./(r-1+(((cc-
d1)./(cc*epsilon)).^(r*kt))))*Af1);
   Mgf_R = (((f_c*((cc-d1)./(cc*epsilon))*r)./(r-1+(((cc-
d1)./(cc*epsilon)).^(r*kt))))*Af1*((h/2)-d1));


%% AXIAL DUE TO CONCRETE FIBRE
   ncr = 1;
   delta_x = cc./ncr;
   e = 1;
   g = 1;
   T(e,g) = (st(1,1)/2 + st(1,na+1)/2)*delta_x;
   error = 1;

   while (error > 1E-2)

      e = e+1;
      g = 1;
      deltax(1,e) = cc./(2.^(e-1));
      ncr = cc./deltax(1,e);

      for z = 1:ncr+1
      w(1,z) = ((f_c*(((z*deltax(1,e))-(deltax(1,e)/2))./(cc*epsilon))*r)./(r-
1+((((z*deltax(1,e))-(deltax(1,e)/2))./(cc*epsilon)).^(r*kt))))*b;
      mw(1,z) = ((f_c*(((z*deltax(1,e))-(deltax(1,e)/2))./(cc*epsilon))*r)./(r-
1+((((z*deltax(1,e))-(deltax(1,e)/2))./(cc*epsilon)).^(r*kt))))*b*((z*deltax(1,e)-
(deltax(1,e)/2))- cc +(h/2));
      end

      T(e,g) = ((w(1,1)/2 + sum(w(1,2:ncr)) + w(1,ncr+1)/2)*deltax(1,e));
      MT(e,g) = ((mw(1,1)/2 + sum(mw(1,2:ncr)) + mw(1,ncr+1)/2)*deltax(1,e));

      for g = 2:e
```

```
            T(e,g) = (((4^(g-1))*T(e,g-1)) - T(e-1,g-1))/((4^(g-1))-1);
            MT(e,g) = (((4^(g-1))*MT(e,g-1)) - MT(e-1,g-1))/((4^(g-1))-1);
        end

        error = abs(T(g,g) - T(g,g-1));
        error = abs(MT(g,g) - MT(g,g-1));

    end
    Cgr_R(:,1) = T(g, g);
    Crc_R(:,1) = (Cgr_R(:,1) - Cgf_R);
    f_at_c = Crc_R(:,1) + Frsa1 + Frsa4 + Frsa5 + Axial

    Mgr_R(:,1) = MT(g,g);
    Mrc_R(:,1) = (Mgr_R(:,1) - Mgf_R);

    Mr = Mrc_R(:,1) + Mrsa1 + Mrsa4 + Mrsa5
    Phi = epsilon_c/cc
end
```